

MAGNETOHYDRODYNAMIC STABILITY OF INTERNAL KINK MODES IN TOKAMAKS APPLICATION OF AN EQUILIBRIUM CODE USING BICUBIC FINITE ELEMENTS

THESE N° 1105 (1992)

PRESENTÉE AU DEPARTEMENT DE PHYSIQUE

ECOLE POLYTECHNIQUE FEDERALE DE LAUSANNE

POUR L'OBTENTION DU GRADE DE DOCTEUR ES SCIENCES

PAR

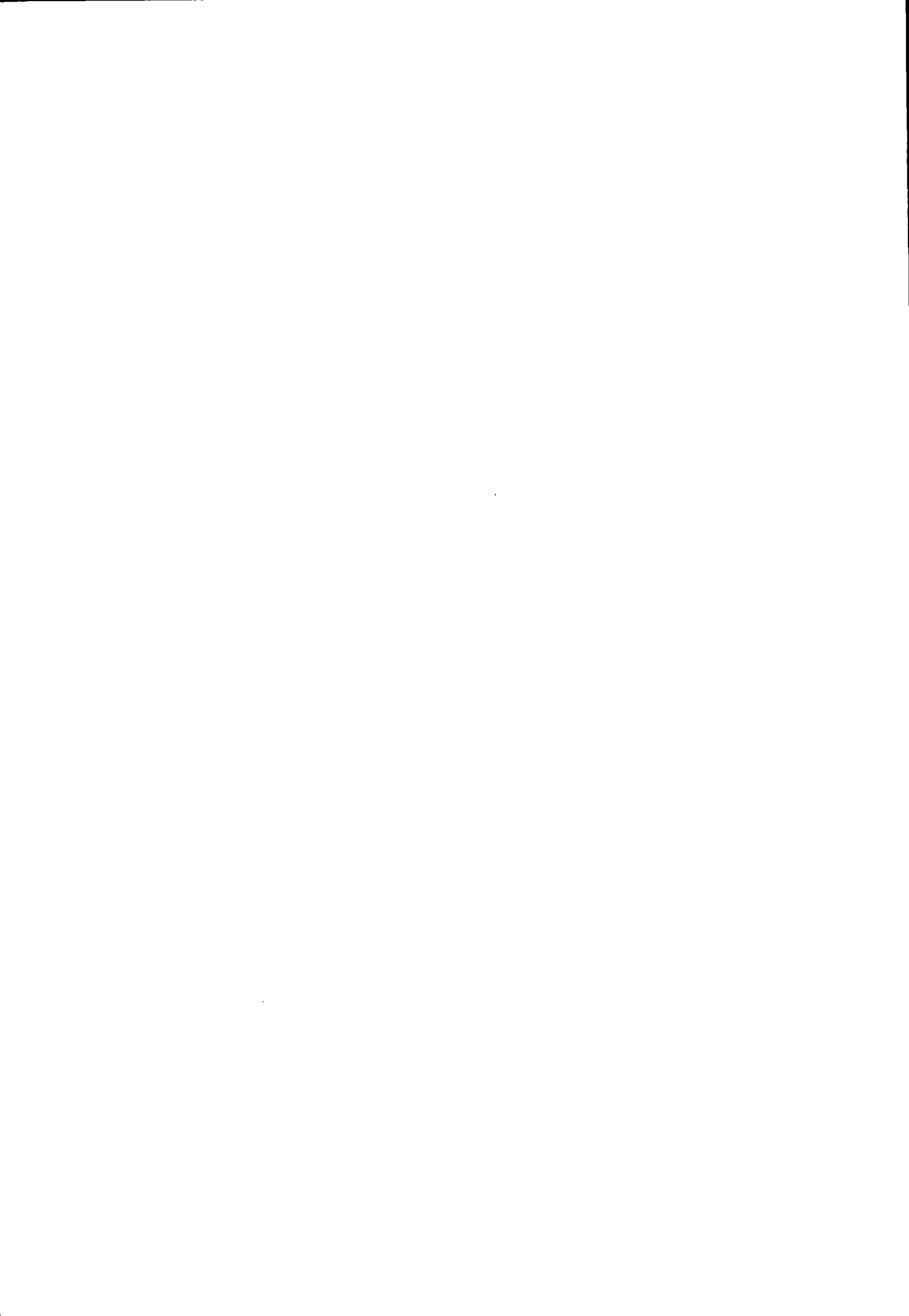
HINRICH LÜTJENS

Physicien diplômé EPFL
de nationalité allemande

acceptée sur proposition du jury:

Dr A. Bondeson, rapporteur
Prof. M.N. Bussac, corapporteur
Dr R. Gruber, corapporteur
Prof. F. Troyon, corapporteur

Lausanne, EPFL
1993



Abstract

Magnetohydrodynamic (MHD) stability limits for the $n = 1$ internal kink mode in a tokamak are investigated. As the internal kink mode is a weak instability, accurate equilibrium solutions are required to determine its stability boundaries. For this purpose, a numerical equilibrium code called CHEASE using Hermite bicubic elements has been developed. The code computes equilibria and provides a mapping to flux coordinates for MHD stability calculations. Several test cases are studied to show the convergence rate of the equilibrium. Convergence tests are also presented for the eigenvalues of the stability calculations when the equilibrium mesh is varied.

Using CHEASE and the toroidal resistive MHD stability code MARS, effects of current profile, plasma cross-section and resistivity on the stability of the internal kink mode are investigated for tokamak equilibria. The results show that the internal kink mode is more unstable than previously thought. The numerical ideal stability results for a circular plasma cross section are compared with the results obtained by an analytic large aspect ratio expansion. It is found that the internal kink is significantly destabilized by the ellipticity of the plasma cross section combined with low shear. A large aspect ratio expansion of the Mercier and the resistive interchange criteria retaining effects of ellipticity and triangularity is given, showing analytically the destabilization by ellipticity.

For resistive internal kink modes, the stabilizing effect of small aspect ratio is confirmed, but as for the ideal case, the stability is very sensitive with respect to shaping of the plasma cross section. For finite pressure and small resistivity, only a very restricted set of equilibria is stable to the internal kink mode.

Résumé

Le sujet de ce travail est l'examen des limites de stabilité magnétohydrodynamique (MHD) des modes kinks internes de nombre d'onde toroïdal $n = 1$ dans un tokamak. Les kinks internes sont des modes à faible taux de croissance, et par conséquent, des solutions d'équilibre très précises sont nécessaires pour déterminer leurs limites de stabilité. Pour cela, un code numérique, appelé CHEASE, qui utilise des éléments finis bicubiques d'Hermite, a été développé. Ce code évalue des équilibres dans les coordonnées de flux et fournit les quantités nécessaires au calcul de stabilité MHD. Plusieurs cas test sont utilisés pour vérifier la convergence de l'équilibre. Des études de convergence sont aussi présentées sur des taux de croissance, afin d'évaluer l'erreur due à l'équilibre sur le calcul de stabilité.

Avec CHEASE et le code toroïdal de stabilité MHD résistive MARS, les effets sur la stabilité du kink interne liés à la forme du profil de courant, à la section du plasma, et à la résistivité sont étudiés pour des équilibres tokamak. Les résultats montrent que le kink interne est moins stable que ce que l'on pensait auparavant. Les résultats numériques de stabilité sont comparés avec ceux obtenus par un développement analytique en grand rapport d'aspect. Il est montré que lorsque le cisaillement des lignes de champ magnétique est faible, le kink interne est déstabilisé de manière importante par l'ellipticité de la section du plasma. Un développement en grand rapport d'aspect est présenté pour les critères de stabilité Mercier et interchange résistif, incluant les effets dus à l'ellipticité et à la triangularité de la section du plasma, afin d'illustrer analytiquement la déstabilisation par l'ellipticité.

Pour les kink internes résistifs, l'effet stabilisant des petits rapports d'aspect est confirmé, mais comme pour les cas idéaux, la stabilité est très sensible aux déformations de la section du plasma. Lorsque la pression est finie et la résistivité faible, le kink interne est stable seulement pour une classe très restreinte d'équilibres.

Remerciements

Je suis particulièrement reconnaissant envers Dr. Anders Bondeson pour sa stimulation et son encouragement tout au long de ce travail. Ses connaissances profondes du domaine de la MHD et son expérience dans le domaine de la numérique m'ont constamment guidé tout au long de ce travail.

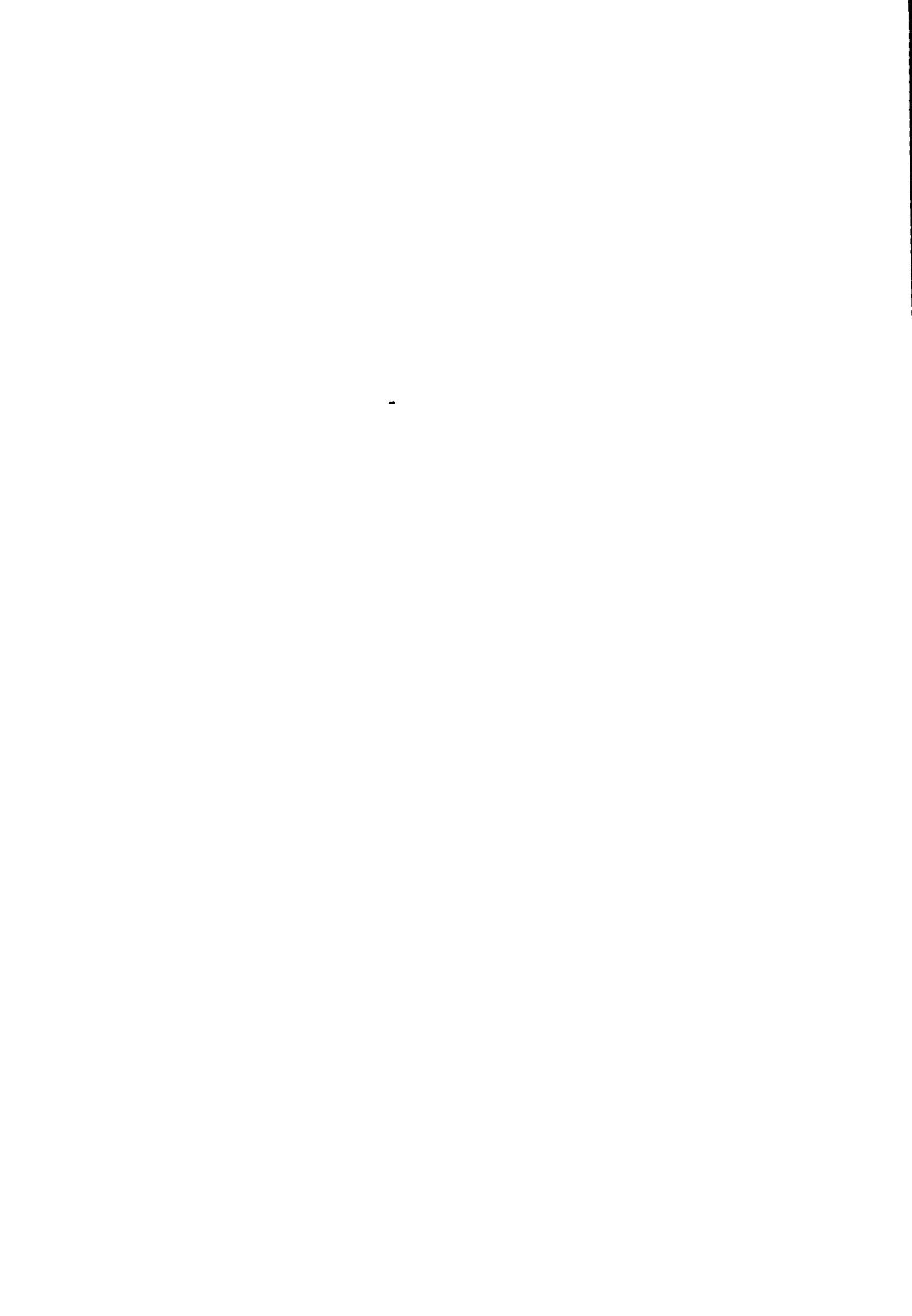
Je remercie Professeur M.N. Bussac, Dr. R. Gruber, Professeur F. Troyon ainsi que Professeur A. Baldereschi d'avoir accepté d'être membre du jury.

Je suis aussi très reconnaissant envers Dr. A. Howling d'avoir relu ce manuscrit en quête de fautes d'anglais éventuelles...

Mes remerciements s'adressent aussi à la direction du CRPP, qui m'a permis d'effectuer ce travail, ainsi qu'à toute l'équipe de l'ancien centre de calcul, qui a su créer une ambiance formidable pendant toutes ces années.

Finalement, mes remerciements vont à tous mes amis, et surtout, à ma femme Anne, pour avoir supporté les moments d'absence et de préoccupation qui ont accompagné l'élaboration de ce travail.

Ce travail a été financé en partie par le fond national suisse de la recherche scientifique.



Contents

1	Introduction	7
1.1	The context	7
1.1.1	Experimental results	7
1.1.2	Theoretical results	8
1.2	The subject	9
1.2.1	Cubic Hermite element equilibrium code	9
1.2.2	Linear MHD stability of internal kink modes	11
2	Axisymmetric toroidal MHD equilibrium resolution with bicubic Hermite finite elements	14
2.1	Equilibrium problem	14
2.2	Method of resolution	16
2.3	Boundary conditions	17
2.4	Specification of the two free functions in the Grad-Shafranov equation .	18
2.5	Transformation of the equilibrium	19
2.6	Convergence of the equilibrium code	20
2.6.1	Solovev Equilibrium	22
2.6.2	Nonlinear equilibria	24
2.7	Comparison test with the equilibrium code CLIO	26
3	Mapping of the equilibrium solution into flux coordinates	28
3.1	Linear stability formulation	28

3.2	Flux coordinates	30
3.3	Computation of flux surface integrals	31
3.4	Convergence Studies of the Mappings	32
3.5	Bicubic spline smoothing of the equilibrium solution. Effects on the stability results.	35
3.6	Comparison of the error on the growth rate of ERATO due to CHEASE and to EQLAUS	36
3.7	Ballooning Stability, Mercier and Resistive Interchange Criteria	38
4	Ideal MHD stability of internal kinks in circular and shaped tokamaks	40
4.1	Circular cross section - Large aspect ratio expansion	41
4.2	Finite aspect ratio calculations - definitions	44
4.3	Circular cross section - Numerical results with finite aspect ratio	45
4.4	Shaping Effects - Numerical results for JET geometry	52
5	Large aspect ratio Mercier and resistive interchange criteria including shape effects	59
6	Resistive toroidal stability of internal kink modes in circular and shaped tokamaks	69
6.1	Dependence on aspect ratio, shaping, and wall separation without pressure	71
6.1.1	Fixed boundary results for zero pressure	72
6.1.2	Free boundary results for zero pressure	73
6.2	Pressure effects	77
6.3	Current profile effects	80
6.3.1	Circular shape	80
6.3.2	JET shape	86
6.3.3	Oblate cross section	89
6.4	Summary of results on resistive stability	89

7	Summary	91
7.1	Cubic Hermite element equilibrium code	91
7.2	MHD stability of internal kink modes in tokamaks	92
A	Bicubic Hermite finite element discretization	94
B	Derivation of expressions involved in the flux coordinate transformation	97
B.1	Expression of χ in terms of θ on a constant poloidal flux surface	97
B.2	Relation between the non-orthogonality and the current density	98
C	Equilibrium quantities for the codes linked to CHEASE	100
C.1	ERATO and LION	100
C.2	MARS	100
C.3	NOVA-W and PEST 3.4	104
D	Bicubic spline interpolation of the cubic Hermite equilibrium solution	106
E	Derivation of the ballooning stability and the Mercier criterion	109
E.1	Ideal ballooning stability criterion	109
E.2	Mercier stability criterion	114
F	Definition of symbols appearing in the text	119
G	Symbolic names of some important variables computed by CHEASE	123



Chapter 1

Introduction

The work reported in the present thesis consists of the construction of an axisymmetric magnetohydrodynamic (MHD) equilibrium code using bicubic Hermite finite elements, and the study of ideal and resistive MHD stability of internal kink modes in tokamaks.

1.1 The context

An almost universal phenomenon in tokamaks is the so-called sawtooth oscillation, a periodic and sudden relaxation of the plasma triggered by an internal instability of toroidal mode number $n = 1$, which releases the energy accumulated in the plasma center. These oscillations are detrimental for fusion, because they limit the central plasma temperature during a discharge. In the next two paragraphs, some important experimental and theoretical results on sawteeth and internal kink modes are reviewed.

1.1.1 Experimental results

In 1974, von Goeler et al. [1] for the first time observed sawteeth experimentally on the ST tokamak. The connection between sawteeth and internal kink modes is due to Kadomtsev [2]. He suggested that the sawteeth are triggered by an internal kink mode of toroidal mode number $n = 1$, and that the nonlinear evolution of these instabilities leads to complete reconnection of the magnetic field lines.

Although the connection between the sawtooth and an $n = 1$ instability has been firmly established, details of the Kadomtsev model have been questioned. An early

example is that of Dubois et al. [3]. They observed sawtooth oscillations in Ohmic discharges on the TFR tokamak which indicated only a partial reconnection of the magnetic field lines after the crash. Similar results were found on the JET (Joint European Torus) tokamak in 1986 by Campbell et al. [4]. Moreover, sawtooth collapse times comparable to the one of smaller tokamaks were observed in JET (between 50 and 100 μs), which again is inconsistent with Kadomtsev's model, where this time depends on the resistive diffusion time of the plasma.

A rather precise knowledge of the safety factor profile is essential for understanding the stability of the central region. The safety factor q characterizes the structure of the magnetic field, and is equal to the number of turns traversed in the toroidal direction (the long way round the torus) of a field line that makes one poloidal turn (the short way round the torus). In TEXTOR (Tokamak Experiment for Technically Oriented Research) [5] and JET [6], investigations on the q profile indicate that the safety factor in the center of tokamaks, q_0 , can be well below unity, even after the sawtooth collapse [7]. Therefore, stable plasma configurations with a $q = 1$ surface exist in tokamaks, which motivates investigations of internal kink stability limits.

1.1.2 Theoretical results

In the first analytical works about internal kink modes in the early seventies, the tokamak plasma was approximated by a cylinder of finite length with periodic boundary conditions [8] (= the "straight tokamak" approximation, see also Wesson [9] or Freidberg, Chapter 9 [10]). But this model neglects effects of the toroidicity, which has a strong influence on the MHD stability limits of the internal kink mode.

Bussac et al. [11] studied in 1975 the MHD stability of the ideal internal kink by means of a large aspect ratio expansion, including toroidal corrections to lowest order in aspect ratio. In contrast with the "straight tokamak" result, they found that the ideal internal kink mode is stable in toroidal geometry when the pressure confined inside the $q = 1$ surface is below a finite threshold value, that depends on the current profile.

In resistive MHD, Glasser, Greene and Johnson [12] derived the dispersion relation for tearing modes and the resistive interchange stability criterion in a torus. This interchange stability criterion is the resistive counterpart of the Mercier stability criterion [13], and its violation is a sufficient condition for resistive instability. Coppi et al. [14] derived a dispersion relation for the resistive kink mode for pressure-less equilibria with circular plasma boundary and infinite aspect ratio, valid for cases near marginal ideal stability. Bussac et al. [15] demonstrated that for ideally stable cases, this resistive kink mode is slowed down to a weaker tearing instability at finite aspect ratio.

Undoubtedly, more sophisticated theories than MHD are required for a complete comprehension of the physics behind the sawtooth oscillations. But already in the simplest theoretical frame, ideal MHD, the understanding of the stability limits of the internal kink is poor. In 1976, Berger et al. [16] demonstrated numerically that the ellipticity is destabilizing significantly the ideal internal kink mode for analytical Solovév equilibria [17]. Conversely, the analytical large aspect ratio expansion including shaping of the plasma cross section by Connor and Hastie [18] suggests that the effect of ellipticity is weak.

As the internal kink is a weak instability, it is sensitive to various effects. In this thesis, the effects of current profile shape, plasma geometry, resistivity and wall separation are investigated. It is shown that ellipticity and resistivity are strongly destabilizing the internal kink, and that even for equilibria with circular cross sections, the ideal stability limits are significantly lower than previously assumed. Moreover, the numerical results presented in the following show that it is very difficult to find entirely (ideally and resistively) stable equilibria with a geometry typical of tokamaks.

1.2 The subject

1.2.1 Cubic Hermite element equilibrium code

In comparison with external kink modes, the internal kinks have small growth rates (typically below $\gamma = 10^{-2}\omega_A$, where $\omega_A = v_A/R_0$ is the toroidal Alfvén frequency).

Moreover, the behavior of resistive instabilities is often sensitive to details in the vicinity of resonant magnetic surfaces (toroidal surfaces on which the magnetic field lines are closed, or where q is a rational quantity). Therefore, an extremely accurate equilibrium solution is required for a precise calculation of such instabilities.

Several numerical codes have been developed in the past, which use various numerical techniques such as conforming [19,20] or non-conforming [21,22] linear finite elements, finite differences [23,24,25,26], spectral decomposition [27], or a variational moment method [28,29,30,31,32]. The methods of resolution applied in several of these codes are documented in a recent review about the computation of MHD equilibria in tokamaks [33]. With these codes, the precision in the equilibrium necessary for an accurate internal kink stability calculation can be obtained by increasing the number of intervals or poloidal modes used for the discretization. However, this proves to be rather expensive in computer time for codes using linear elements. The spectral methods solve this problem only partially, because as soon as the plasma cross section becomes very non-circular (for instance a sharp dee), a large number of poloidal modes are required to obtain a precise solution, and this again is computer time consuming.

Therefore, a new numerical code, called CHEASE [34] (Cubic Hermite Element Axisymmetric Static Equilibrium) has been developed, solving the MHD equilibrium problem in axisymmetric geometry, using bicubic Hermite finite elements. With bicubic Hermite elements, the error of the solution converges locally as

$$\|\Psi - \Psi_{\text{Hermite}}\| < Ch^4 \quad (1.1)$$

where C is a constant and h is the discretization mesh “cell size” [35]. The Hermite bicubic elements ensure that the gradient of the solution is continuous over the whole equilibrium mesh, and guarantee that the second derivative of the solution converges within every cell of the mesh.

With CHEASE and the toroidal resistive stability code MARS [36], ideal MHD growth rates down to $5 \cdot 10^{-4} \omega_A$ can readily be computed. These codes are therefore

appropriate for MHD stability studies of internal kink modes in tokamaks.

The first part of this thesis is organized as follows:

- Chapter 2 gives an outline of the bicubic finite element method applied for the resolution of the axisymmetric equilibrium in toroidal geometry. Convergence studies for different equilibria of the poloidal magnetic energy and the magnetic axis are presented, and compared with the results obtained by the linear “hybrid element” CLIO [21,22].
- Chapter 3 describes the mapping of the equilibrium to flux coordinates and the computation of the equilibrium quantities required by the stability codes MARS and ERATO [37] and the Alfvén and ion cyclotron range of frequencies code LION [38]. The accuracy of the mapping is checked by convergence tests on eigenvalues obtained with the stability codes ERATO and MARS when the equilibrium mesh is refined. The errors on MHD growth rates computed with ERATO due to CHEASE and the finite difference equilibrium code EQLAUS [26] are compared.

1.2.2 Linear MHD stability of internal kink modes

The dynamics of a plasma involve several distinct spatial and temporal scales, and a variety of models can be applied for its description. In general, global plasma instabilities that occur on the Alfvén time scale are well described by approximating the plasma as a conducting fluid. This model is called MagnetoHydroDynamics (MHD).

The MHD equations including the effects of finite resistivity are

$$\begin{aligned}
 \frac{\partial \rho}{\partial t} + \nabla \cdot \rho \mathbf{v} &= 0 && \text{(Continuity)} \\
 \rho \frac{D\mathbf{v}}{Dt} &= \mathbf{J} \times \mathbf{B} - \nabla p && \text{(Newton)} \\
 \frac{Dp}{Dt} + \Gamma p \nabla \cdot \mathbf{v} &= 0 && \text{(Equation of state)} \\
 \mathbf{E} + \mathbf{v} \times \mathbf{B} &= \eta \mathbf{J} && \text{(Ohm's law)} \\
 \nabla \times \mathbf{E} &= -\frac{\partial \mathbf{B}}{\partial t} && \text{(Faraday)} \\
 \nabla \times \mathbf{B} &= \mathbf{J} && \text{(Ampere's law)} \\
 \nabla \cdot \mathbf{B} &= 0 && \text{(Initial conditions)}
 \end{aligned} \tag{1.2}$$

where ρ is the mass density of the fluid, \mathbf{v} the velocity and p the pressure, which is assumed to be isotropic. \mathbf{B} is the magnetic field, \mathbf{E} the electric field, \mathbf{J} the current density, η the resistivity of the plasma and Γ the ratio of specific heats. D/Dt denotes the convective derivative : $D/Dt = \partial/\partial t + \mathbf{v} \cdot \nabla$.

Using the MHD model, Bussac et al. [11] calculated analytically the pressure limit for ideal internal kink stability in circular equilibria by a large aspect ratio expansion. For parabolic current profile and a small $q = 1$ radius, they found that the $n = 1$ internal kink mode is stable when the poloidal beta on the $q = 1$ surface satisfies $\beta_p < (13/144)^{1/2} \approx 0.3$. The poloidal beta, denoted by β_p , characterizes the pressure confinement inside the $q = 1$ surface. In the present thesis, numerical stability results obtained for circular cross sections with CHEASE and MARS at finite aspect ratio show that the critical β_p is generally significantly lower than 0.3. This discrepancy is resolved as a result of the choice of the boundary conditions. In the examples presented by Bussac et al. in [11], fixed boundary conditions were assumed. Here, Bussac's analytical large aspect ratio stability criterion will be applied to equilibria with a more realistic boundary prescription, giving β_p -limits that are in good agreement with the numerical results at finite aspect ratio.

With respect to shaping, analytical studies [18,39] suggest that the effect of ellipticity is weak when the central safety factor q_0 is close to unity, whereas numerical computations show a clear destabilization by elliptic shaping [16,40]. Our numerical calculations, without recourse to geometrical orderings, confirm that ellipticity is strongly destabilizing, in particular, at low shear. The main part of this destabilization results from ellipticity in combination with finite pressure and finite aspect ratio. As an analytical example of this destabilization, a large aspect ratio expression for the Mercier and the resistive interchange criteria is presented, which includes the effects of ellipticity and triangularity.

The last part of this thesis gives numerical results on resistive stability of the internal kink. For very low pressure and circular cross section, the study confirms previous

results obtained by Holmes et al. [41]: Resistive stability is favored by small aspect ratio, low shear at the $q = 1$ surface, and low q_0 . However, it is found that even slight pressure severely restricts the region of complete resistive MHD stability when $q_0 < 1$. This result is discussed analytically by considering the resistive and ideal interchange criteria, which play important roles for the linear stability of the internal kink. At finite pressure, resistive instability is hard to avoid because the resistive interchange criterion tends to be violated at $q = 1$, as a result of non-circularity. A typical result, when pressure and shape effects are taken into account, is that the internal kink mode is slowed down by toroidal effects, and turns into a weak resistive tearing/interchange mode at small resistivity. Elliptic shaping renders pressure gradients considerably more destabilizing than for circular flux surfaces by violation of the resistive interchange criterion.

The second part of this thesis is organized as follows:

- In Chapter 4, numerical results on the stability of the ideal internal kink are presented. Effects of shaping of the plasma cross section and shape of the current profile are investigated. For circular cross sections, a comparison with the analytical large aspect ratio results is given.
- An expansion of the Mercier and the resistive interchange criteria is given in Chapter 5. These show analytically the strong destabilizing effect of ellipticity of the plasma cross section.
- Chapter 6 reports results about the resistive stability of the internal kink. Effects of aspect ratio, shaping of the cross section, shape of the current profile, pressure and wall separation are investigated numerically.



Chapter 2

Axisymmetric toroidal MHD equilibrium resolution with bicubic Hermite finite elements

The first part of this thesis describes the construction of a new equilibrium code, named CHEASE (for Cubic Hermite Element Axisymmetric Static Equilibrium), using bicubic Hermite finite elements for the discretization [34]. This code is documented in Chapters 2 and 3. Convergence studies of equilibrium quantities and comparative tests with existing equilibrium codes are presented. Quite generally, these tests show the improvement in numerical precision and the savings in computation time for typical tokamak applications in comparison with codes using linear finite elements.

2.1 Equilibrium problem

The problem of axisymmetric static MHD equilibrium is well known [42]. An axisymmetric magnetic field can be represented as

$$\mathbf{B} = G\nabla\Phi + \nabla\Phi \times \nabla\Psi \quad (2.1)$$

where Φ is the ignorable toroidal angle (see Figure 2.1) and Ψ is the poloidal magnetic flux function. For static MHD equilibria, $\partial/\partial t = 0$ and $\mathbf{v} = 0$, and eq.(1.2) reduces to

$$\begin{aligned} \mathbf{J} \times \mathbf{B} &= \nabla p \\ \nabla \times \mathbf{B} &= \mathbf{J} \\ \nabla \cdot \mathbf{B} &= 0 \end{aligned} \quad (2.2)$$

In that case, the poloidal current flux function G and the plasma pressure p are functions of Ψ only. Substituting eq.(2.1) into eq.(2.2) leads to the Grad-Shafranov equation [43,44,45]

$$\nabla \cdot \frac{1}{R^2} \nabla \Psi = -p'(\Psi) - \frac{1}{R^2} G G'(\Psi) = \frac{j_\phi}{R} \quad (2.3)$$

where j_ϕ denotes the toroidal plasma current density, R the major radius and prime the derivative with respect to Ψ . Eq.(2.3) is an elliptic second order nonlinear partial

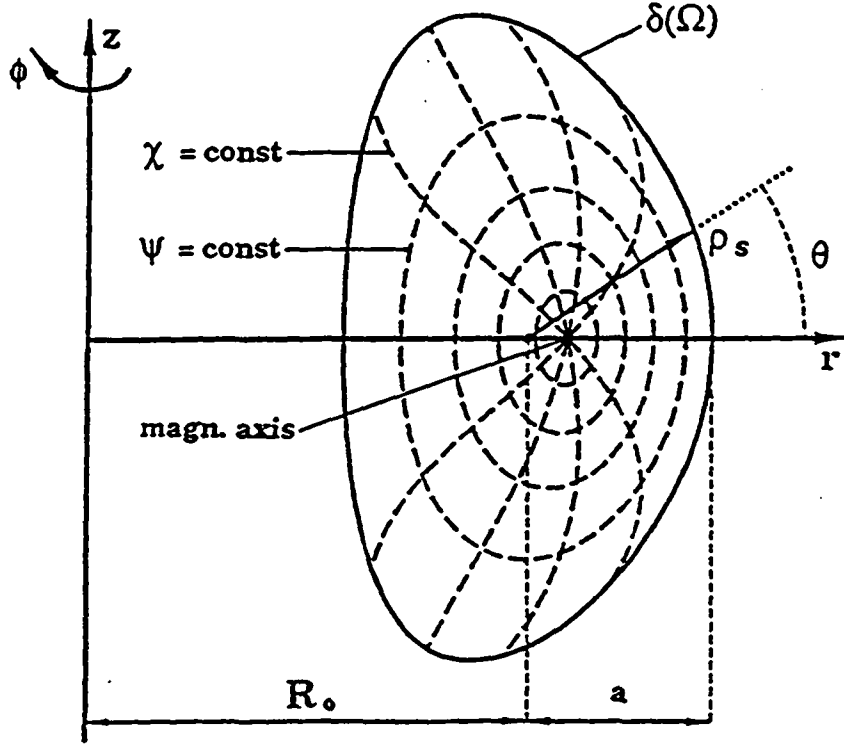


Figure 2.1: The cylindrical coordinates $(R; Z; \Phi)$ in toroidal geometry.

differential equation. The nature of the equilibria (i.e. tokamak, reversed field pinch, etc.) is determined by the two free functions $p'(\Psi)$ and $GG'(\Psi)$. These issues will be discussed in Section 2.4.

In the following, the plasma cross section Ω is assumed to be known. Thus, we restrict consideration of eq.(2.3) to the fixed boundary case with $\Psi \equiv 0$ on the plasma edge $\delta\Omega$. Furthermore, only cases with one single magnetic axis are considered : Ψ is negative everywhere inside the plasma and the total plasma current

$$I = \int_{\Omega} j_\phi dS \quad (2.4)$$

is positive.

For the solution of equilibrium eq.(2.3), CHEASE transforms the plasma cross section Ω into a rectangular region $0 \leq \sigma \leq 1$, $0 \leq \theta \leq 2\pi$ by the use of a modified and non-orthogonal coordinate system (σ, θ) related to the cylindrical coordinates (R, Z) by (see Figure 2.1)

$$\begin{aligned} R &= \sigma \rho_s(\theta) \cos \theta + R_c \\ Z &= \sigma \rho_s(\theta) \sin \theta + Z_c. \end{aligned} \quad (2.5)$$

2.2 Method of resolution

CHEASE uses a variational method for the resolution of the Grad-Shafranov equation (2.3) [46]. The variational form of the Grad-Shafranov equation is

$$\int_{\Omega} \frac{1}{R} \nabla_{\zeta} \cdot \nabla \Psi \, dS + \int_{\Omega} \zeta j_{\Phi} \, dS = 0. \quad (2.6)$$

where ζ is an arbitrary weighting function from the same function space as Ψ . Eq.(2.6) is solved numerically in the standard manner of the finite element method by expanding Ψ in Hermite bicubics on the rectangular grid (σ, θ) [35,46], as described in detail in Appendix A. The unknowns of the discretized equilibrium problem are the values of the function Ψ , its first derivatives $\partial\Psi/\partial\sigma$ and $\partial\Psi/\partial\theta$ and the mixed second derivative $\partial^2\Psi/\partial\sigma\partial\theta$, all on the nodes of the mesh. The integrals in eq.(2.6) are carried out numerically using a Gaussian quadrature formula.

The nonlinear eq.(2.6) is solved iteratively by a Picard method, i.e. the solution after $k + 1$ iteration steps Ψ_{k+1} is computed with help of the solution after k iteration steps Ψ_k :

$$\int_{\Omega} \frac{1}{R} \nabla_{\zeta} \cdot \nabla \Psi_{k+1} \, dS = - \int_{\Omega} \zeta j_{\Phi}(\Psi_k) \, dS \quad (2.7)$$

The Picard iteration is interrupted when

$$\|\Psi_{k+1} - \Psi_k\| < \epsilon \quad (2.8)$$

where ϵ is a predefined number. The norm used in eq.(2.8) is

$$\|u\| = \left[\int_{\Omega} u^2 \, dS \right]^{1/2}. \quad (2.9)$$

The iterations are normally done first on a coarse grid ($N_\sigma \times N_\theta = 16 \times 16$) and later on a more refined grid. For the coarse grid, the center of the polar coordinates is chosen as the geometrical midpoint ($R_0, 0$) of the plasma. For the equilibrium calculation, all distances are scaled so that $R_0 = 1$. For the refined grid, the magnetic axis of the approximate solution is chosen as the center of the polar coordinates. This is done to facilitate the subsequent mapping to flux coordinates required for the stability calculation.

2.3 Boundary conditions

As mentioned in Section 2.1, we consider the fixed boundary case $\Psi \equiv 0$ on $\delta\Omega$. This implies $\Psi = 0$ and $\partial\Psi/\partial\theta = 0$ for all the boundary points $\sigma = 1$ and $\theta = \theta_j, j = 1, \dots, N_\theta$, where N_θ is the number of intervals in the θ -direction.

The origin of the polar coordinate system requires some extra care as the coordinate transformation (2.5) becomes singular there and one single geometrical point is represented by N_θ mesh points. Conditions have to be imposed to guarantee that Ψ is a regular function of R and Z at the origin. A first order Taylor expansion of Ψ around (R_0, Z_0) , when expressed in terms of (σ, θ) leads to

$$\Psi = \Psi_c + \sigma \rho_s(\theta) [\Psi_R \cos(\theta) + \Psi_Z \sin(\theta)] + \mathcal{O}(\sigma^2) \quad (2.10)$$

Thus, the regularity condition forces the $4N_\theta$ unknowns $\Psi, \partial\Psi/\partial\sigma, \partial\Psi/\partial\theta$ and $\partial^2\Psi/\partial\sigma\partial\theta$ for $\sigma = 0$ and $\theta = \theta_j, j = 1, \dots, N_\theta$ to be replaced by the three unknowns Ψ_c, Ψ_R and Ψ_Z . The following conditions are imposed by collocation on the N_θ grid points for $\sigma = 0$:

$$\begin{aligned} \Psi &= \Psi_c \\ \frac{\partial\Psi}{\partial\theta} &= 0 \\ \frac{\partial\Psi}{\partial\sigma} &= \rho_s(\theta) [\Psi_R \cos \theta + \Psi_Z \sin \theta] \\ \frac{\partial^2\Psi}{\partial\sigma\partial\theta} &= \rho_s(\theta) [-\Psi_R \sin \theta + \Psi_Z \cos \theta] + \\ &\quad \frac{d\rho_s}{d\theta} [\Psi_R \cos \theta + \Psi_Z \sin \theta] \end{aligned} \quad (2.11)$$

The conditions (2.11) guarantee that Ψ and $|\nabla\Psi|$ are constant at the mesh center.

2.4 Specification of the two free functions in the Grad-Shafranov equation

There are many different ways of defining the two free functions $p'(\Psi)$ and $GG'(\Psi)$ in the Grad-Shafranov equation (2.3). For example, early β optimizations were made by specifying $p'(\Psi)$ and $GG'(\Psi)$ independently [47]. However, it soon appeared that it is difficult to control equilibrium quantities such as the current density profile and the safety factor

$$q(\Psi) = \frac{G(\Psi)}{2\pi} \oint_{\Psi=\text{const}} \frac{dl}{R|\nabla\Psi|} \quad (2.12)$$

with this method, especially near the plasma edge. The specification of a suitable averaged current density profile instead of the $GG'(\Psi)$ profile solves this problem.

In CHEASE, three different kind of profile specifications have been implemented in which $p'(\Psi/\Psi_{min})$ is specified together with one of:

- $GG'(\Psi/\Psi_{min})$
- The surface averaged current density within a given flux surface

$$I^*(\Psi/\Psi_{min}) = \frac{\oint_{\Psi=\text{const}} j_{\Phi} J/Rd\chi}{\oint_{\Psi=\text{const}} J/Rd\chi} = -\frac{C_1}{C_0} p' - \frac{C_2}{C_0} GG' \quad (2.13)$$

- The averaged parallel current density

$$j_p(\Psi/\Psi_{min}) = \frac{\langle \mathbf{J} \cdot \mathbf{B} \rangle}{\langle \mathbf{B} \cdot \nabla\Phi \rangle} = -\frac{p'}{C_2} - GG' \left(1 + \frac{1}{G^2} \frac{C_3}{C_2} \right) \quad (2.14)$$

where $\langle \dots \rangle$ denotes the volume average along a flux surface.

The averaged current density profiles I^* and j_p in eq.(2.13,2.14) are formulated in terms of the four surface integrals

$$\left\{ C_0(\Psi), C_1(\Psi), C_2(\Psi), C_3(\Psi) \right\} = \oint_{\Psi=\text{const}} \left\{ \frac{1}{R}, 1, \frac{1}{R^2}, \frac{|\nabla\Psi|^2}{R^2} \right\} Jd\chi \quad (2.15)$$

Replacing eq.(2.13;2.14) into the current density in eq.(2.3) gives

$$j_{\Phi}(\Psi/\Psi_{min}) = \frac{1}{R} \frac{C_0}{C_2} I_N^* + \left(\frac{1}{R} \frac{C_1}{C_2} - R \right) p' \quad (2.16)$$

if I^* is specified and

$$j_{\Phi}(\Psi/\Psi_{min}) = \frac{1}{yR} j_p + \frac{1}{y} \left(\frac{1}{R} \frac{1}{C_2} - Ry \right) p' \quad (2.17)$$

where

$$y = 1 + \frac{1}{G^2} \frac{C_3}{C_2} \quad (2.18)$$

if j_p is prescribed. For the computation of an equilibrium with the I^* or the j_p profile, the integrals (2.15) must be evaluated on a chosen set of Ψ values. This requires a mapping of the equilibrium solution into flux coordinates (Ψ, χ, Φ) , where χ is a generalized poloidal angle. The method applied for this will be described in Section 3.3. At present, it is only important to notice that because of this mapping, an additional iteration over the source term of the Grad-Shafranov equation must be introduced : let $C_{i,l}(\Psi)$, $i = 1, 2, 3, 4$ be the integrals in eq.(2.15) at iteration step l over the mapping. The values of these integrals are held fixed during the Picard iterations in eq.(2.7), until the solution converges. At this stage, the $C_{i,l+1}(\Psi)$'s at iteration step $l + 1$ over the mapping are reevaluated from the converged equilibrium solution, and a new Picard iteration can be started, keeping this time the $C_{i,l+1}(\Psi)$'s fixed. This process is stopped when

$$\left[\sum_{\Psi \text{ values}} \{C_{i,l+1}(\Psi) - C_{i,l}(\Psi)\}^2 \right]^{1/2} < \epsilon \quad (2.19)$$

for $i = 1, \dots, 4$. For the integration of the variational form (2.6), the values of the integrals (2.15) required on the Gaussian quadrature points are obtained by interpolating with cubic splines between the $C_{i,l}(\Psi)$ values known on a finite set of Ψ values.

2.5 Transformation of the equilibrium

It is well known [37] that a single solution of the Grad-Shafranov equation (2.3) can be used to generate a whole sequence of equilibria with fixed poloidal beta, but different

plasma current and rotational transform. Two transformations which leave eq.(2.3) unchanged are used to effect this. The first is a scaling

$$\Psi_{new} = \lambda \Psi_{old}; G_{new} = \lambda G_{old}; p_{new} = \lambda^2 p_{old}. \quad (2.20)$$

The second is a shift of G^2

$$G_{new}^2 = G_{old}^2 + c, \quad (2.21)$$

with Ψ and p unchanged. By these transformations, equilibria can be generated with prescribed values of either the total current (2.4), or of the safety factor $q(\Psi_q)$ on some arbitrary flux surface Ψ_q . The existence of two transformations also allows specification of G on a given flux surface Ψ_G .

When the total current is specified, first the scaling (2.20) is applied with $\lambda = I_{specified}/I_{old}$ and then G^2 is shifted using (2.21) with $c = G_{specified}^2(\Psi_G) - G^2(\Psi_G)$, where G denotes the value after rescaling. When the safety factor is prescribed, first G^2 is shifted by $c = \{q_{specified}^2/q_{old}^2(\Psi_q) - 1\}G^2(\Psi_q)$, where $q_{old}(\Psi_q)$ is obtained from eq.(2.12), and then the solution is rescaled by $\lambda = G_{specified}/G(\Psi_G)$, where G denotes the value after the shift.

After the transformation of the equilibrium, all relevant physical quantities characterizing the equilibrium can be computed. A list of these quantities is shown in Table 2.1.

2.6 Convergence of the equilibrium code

In this Section, examples are presented to show the convergence of the equilibrium solution with respect to the cell size. For these tests, an equal number of intervals in the σ and θ directions is used, $N_\sigma = N_\theta = N$, and the "cell size" is defined as $h = 1/N$. Standard error estimates [35,46] predict that Ψ itself converges with an $\mathcal{O}(h^4)$ error, while the error in $\nabla\Psi$ is $\mathcal{O}(h^3)$.

Two different quantities are used to record the convergence, namely, the poloidal

Global quantities	
Total plasma volume / 2π	$V_{tot} = \int_{\Omega} J d\Psi d\chi$
Volume average	$\bar{f} = \left(\int_{\Omega} f J d\Psi d\chi \right) / V_{tot}$
Total toroidal current	$I = \int_{\Omega} j_{\phi}(J/R) d\Psi d\chi$
Normalized total toroidal current	$I_N = \frac{I}{aT_{surf}}$
Plasma inductance	$\ell_i = \frac{4\pi}{I_{\phi}^2 R_0} \int_{\Omega} \frac{ \nabla\Psi ^2}{R^2} J d\Psi d\chi$
Pressure peaking factor	$ppf. = \frac{p_0}{\bar{p}}$
Total beta	$\beta = \frac{2\bar{p}}{B^2}$
Fusion beta	$\beta^* = \frac{2(\bar{p}^2)^{1/2}}{B^2}$
Total experimental beta	$\beta_z = \frac{2R_0^2 \bar{p}}{T_{surf}^2}$
Total poloidal beta	$\beta_{p,tot} = \frac{8\pi}{I_{\phi}^2 R_0} \bar{p} V_{tot}$
Flux surface quantities	
Volume of $\Psi = \text{const}$ / 2π	$V(\Psi) = \int_{\Psi'=\Psi_{min}}^{\Psi} \oint J d\chi d\Psi'$
Generalized radius of $\Psi = \text{const}$	$\rho(\Psi) = (V(\Psi)/V_{tot})^{1/2}$
Toroidal current within $\Psi = \text{const}$	$I_{\phi}(\Psi) = \int_{\Psi'=\Psi_{min}}^{\Psi} \oint j_{\phi}(J/R) d\chi d\Psi'$
Poloidal beta on $\Psi = \text{const}$	$\beta_p(\Psi) = -\frac{8\pi}{I_{\phi}^2(\Psi) R_0} \int_{\Psi'=\Psi_{min}}^{\Psi} p'(\Psi') V(\Psi') d\Psi'$
Global shear on $\Psi = \text{const}$	$\hat{s}(\Psi) = \frac{\rho}{q(\Psi)} \frac{dq}{d\rho}(\Psi)$
Local quantities	
Local shear	$\hat{s}_{local} = -\frac{(\mathbf{B} \times \nabla\Psi) \cdot \nabla \times (\mathbf{B} \times \nabla\Psi)}{ \nabla\Psi ^2}$
Magnetic field line curvature	$\kappa = \frac{1}{B^2} \nabla\Psi \cdot (\mathbf{B} \cdot \nabla) \mathbf{B}$

Table 2.1: Physical quantities computed by equilibrium code

magnetic field energy

$$\mathcal{W}_B = \frac{1}{2} \int_{\sigma=0}^1 \int_{\theta=0}^{2\pi} \sigma \rho_s^2(\theta) \frac{|\nabla \Psi|^2}{R} d\sigma d\theta. \quad (2.22)$$

and the position of the magnetic axis R_m . In the special case where the equilibrium equation (2.3) is linear, i.e. j_ϕ is independent of Ψ , the poloidal magnetic field energy is expected to converge as $\mathcal{O}(h^6)$ [35,46]. For an up-down symmetric equilibrium, the magnetic axis where $\nabla \Psi = 0$ will occur at $(R, Z) = (R_m, 0)$. Evidently, R_m should have the same convergence properties as $\partial \Psi / \partial R$, i.e. the error should be $\mathcal{O}(h^3)$.

In the convergence tests to follow, the θ -mesh has been generated in such a way that the area of all cells in the θ -direction (for fixed σ) is the same. Two different classes of equilibria will be considered: analytic Solovév equilibria [17] and nonlinear equilibria where p' , GG' and I^* are functions in Ψ / Ψ_{min} .

2.6.1 Solovév Equilibrium

A standard test case for any equilibrium code is the family of analytic equilibria found by Solovév [17] for which eq.(2.3) is a linear equation for Ψ . Here, we consider the special case where

$$\begin{aligned} P(\Psi) &= -\frac{1 + \kappa^2}{\kappa R_0^3 q_0} \Psi \\ G(\Psi) &= G_0 = 1 \end{aligned} \quad (2.23)$$

and the poloidal beta on axis is unity. In eq.(2.23), κ denotes the elongation, R_0 and a the major and the minor plasma radius, respectively. q_0 is the safety factor on the magnetic axis. The corresponding analytic formula for Ψ is

$$\Psi = \frac{\kappa}{2R_0^3 q_0} \left(\frac{R^2 Z^2}{\kappa^2} + \frac{1}{4} (R^2 - R_0^2)^2 - a^2 R_0^2 \right) \quad (2.24)$$

For the convergence study, a Solovév equilibrium with $q_0 = 3/4$, $\kappa = 1$, $a = 1/3$ and $R_0 = 1$ is used. This equilibrium will be called "test case I" in the following.

In Figure 2.2, the poloidal magnetic field energy of the numerical solution converges towards its analytical value with an $\mathcal{O}(h^6)$ error. Figure 2.3 shows that the error in the magnetic axis R_m is $\mathcal{O}(h^3)$. Thus, the poloidal magnetic field energy and the magnetic axis converge according to theoretical expectation.

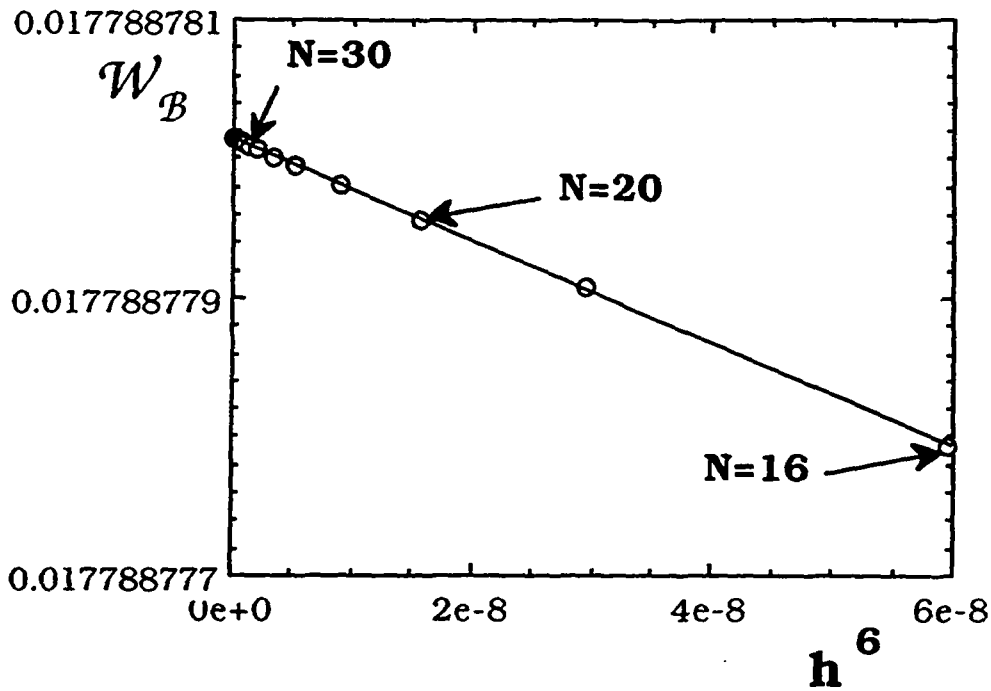


Figure 2.2: Convergence of the poloidal magnetic energy of the test case I (Solovev). The regression curve is $W_B = 1.778878015 \cdot 10^{-2} - 3.7001 \cdot 10^{-2} h^6$.

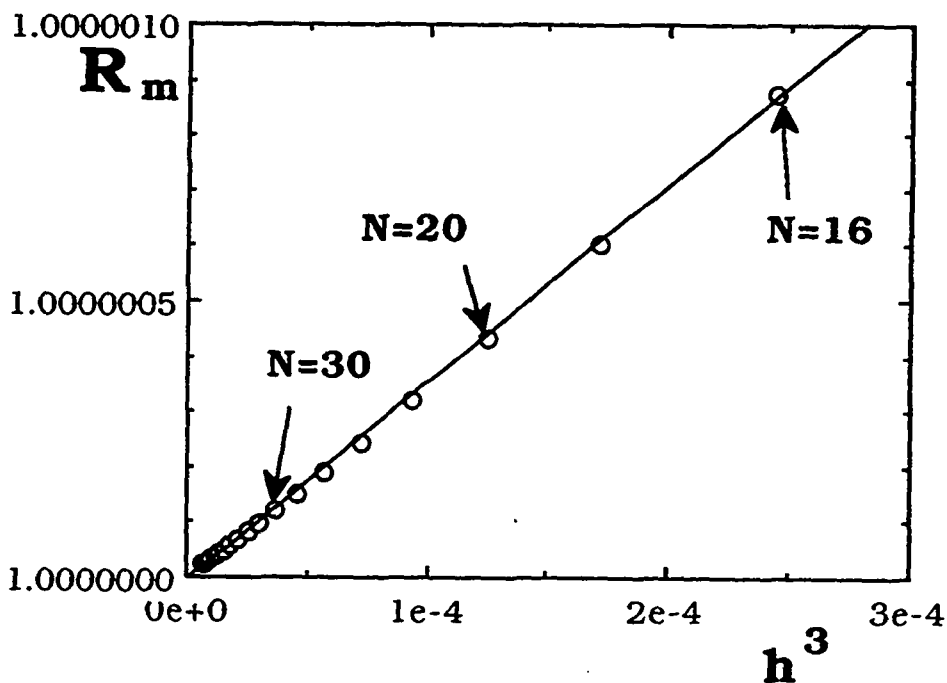


Figure 2.3: Convergence of the magnetic axis of the test case I (Solovev). The regression curve is $R_m = 1 + 3.5711 \cdot 10^{-3} h^3$.

2.6.2 Nonlinear equilibria

The Solovév equilibrium bypasses one difficulty in eq.(2.3): the problem loses its non-linearity, as the source term j_ϕ is independent of Ψ . To remove this restriction, we now consider some “nonlinear” test cases, where j_ϕ depends on Ψ . The plasma surface is defined by

$$\begin{aligned} R &= R_0 + a \cos(\theta + \delta \sin \theta - \zeta \sin 2\theta) \\ Z &= \kappa a \sin \theta \end{aligned} \tag{2.25}$$

where a , κ and R_0 have the same meaning as in eq.(2.23), δ is the triangularity, and ζ is a parameter which, if it is positive, broadens the “tips” of the plasma cross section.

Two nonlinear test cases are considered, one with polynomial definition of p' and GG' , and one where p' and I^* are specified:

- Test case II: $a/R_0 = 0.37$, $\kappa = 1.7$, $\delta = 0.3$, $\zeta = 0$ and

$$\begin{aligned} p'(\Psi/\Psi_{min}) &= -0.14(\Psi/\Psi_{min}) \\ GG'(\Psi/\Psi_{min}) &= -0.2(\Psi/\Psi_{min}) + 0.249(\Psi/\Psi_{min})^2. \end{aligned} \tag{2.26}$$

Test case II has been rescaled using the transformation described in Section 2.5 so that the safety factor on axis is $q_0 = 1.2$.

- Test case III : $a/R_0 = 0.37$, $\kappa = 1.7$, $\delta = 0.3$, $\zeta = 0$ and

$$\begin{aligned} p'(\Psi/\Psi_{min}) &= \begin{cases} 0.22 & \text{if } 0 < t < 0.4 \\ -0.611t^2 + 0.489t + 0.122 & \text{if } 0.4 < t < 1 \end{cases} \\ I^*(\Psi/\Psi_{min}) &= \begin{cases} -1.1t + 1 & \text{if } 0 < t < 0.16 \\ 1.22t^3 - 1.47t^2 - 0.723t + 0.972 & \text{if } 0.16 < t < 1 \end{cases} \end{aligned} \tag{2.27}$$

where $t = 1 - \Psi/\Psi_{min}$. Test case III has been rescaled so that the $q = 1$ surface has a radius of $\rho = 0.4$ (ρ is the generalized radius defined in Table 2.1). This case is a typical example of an equilibrium used for the internal kink stability study in Chapter 4.

Figure 2.4 shows that the magnetic axis converges according to theoretical prediction with an $\mathcal{O}(h^3)$ error for the two nonlinear test cases. The $\mathcal{O}(h^3)$ convergence of the magnetic axis for test case III shows that the convergence of the cubic Hermite elements

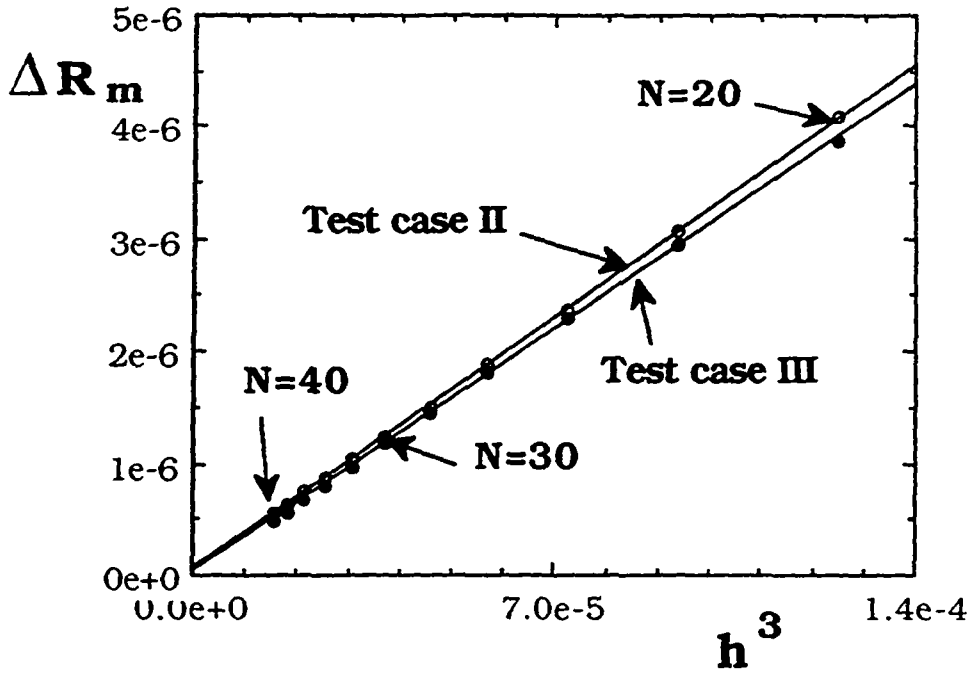


Figure 2.4: Convergence of the magnetic axis of the nonlinear test cases. The regression curve is $|R_m/R_0 - 1.058353| = 3.2183 \cdot 10^{-2} h^3$ for test case II and $|R_m/R_0 - 1.0428771| = 3.1111 \cdot 10^{-2} h^3$ for test case III.

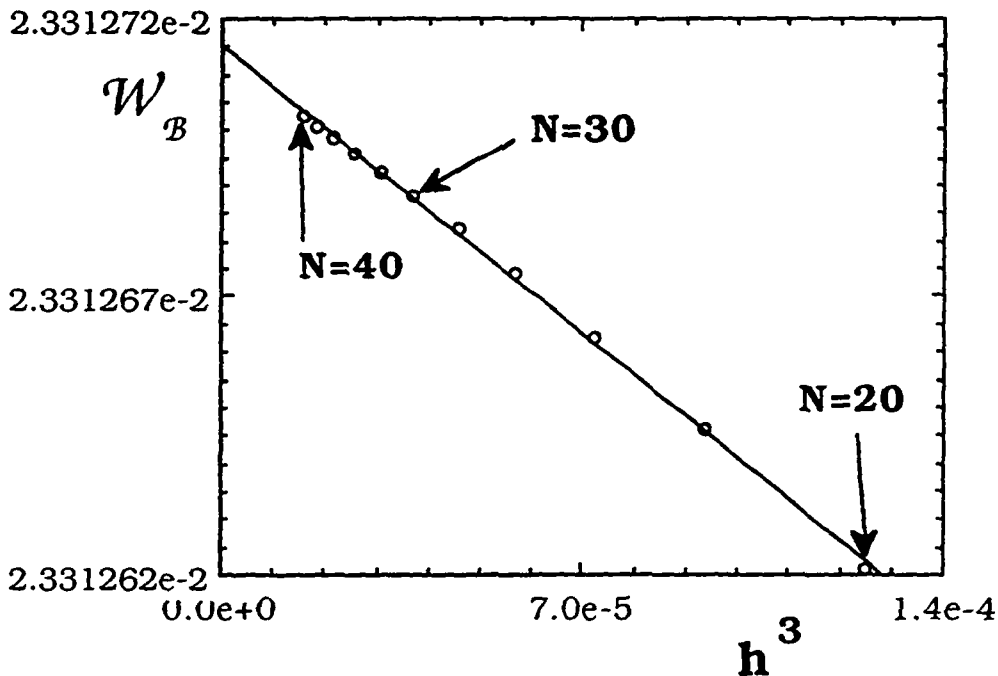


Figure 2.5: Convergence of the poloidal magnetic energy of the test case II.

is not changed by the mappings to flux coordinates required for the computation of the integrals (2.15) in the current density (2.16).

In the case where eq.(2.3) is a nonlinear equation in Ψ , the poloidal magnetic field energy (2.22) is no longer expected to converge in $\mathcal{O}(h^6)$ as for linear equilibria. Indeed, the error in the poloidal magnetic field energy of test case II converges as $\mathcal{O}(h^3)$ in Figure 2.5, which is the convergence rate expected for $\nabla\Psi$.

2.7 Comparison test with the equilibrium code CLIO

The position of the magnetic axis is commonly used for validating equilibrium codes. In Ref.[22], a Solovév equilibrium with $\mathcal{K} = 2$, $R_0 = 1$, $a = 0.4$ and $q_0 = 1$ was used as convergence test of the finite linear “hybrid element” code CLIO. According to the curve presented in [22], the error in the magnetic axis $|R_m - 1| = 0.130h^2$ with CLIO. The same equilibrium has been computed with CHEASE. A linear regression gives $|R_m - 1| = 9.9660 \cdot 10^{-3}h^3$ for the same equilibrium. To compare the efficiency of the linear and cubic elements, we note in Figure 2.6 that CLIO yields an error of $\Delta R_m \simeq 1.5 \cdot 10^{-6}$ for the magnetic axis position with a 300×300 mesh, whereas CHEASE needs less than a 16×16 mesh to reach the same accuracy. The cpu-time required for the calculation of these equilibria on CRAY-2 is about 350 seconds for CLIO and less than 2 seconds for CHEASE.

The same comparison can be made with the JET test case shown in the same publication. There, the error in the magnetic axis (see Figure 2.6) behaves like $R_m/R_0 - 1.1014865 = 1.8193 \cdot 10^{-2}h^3$ for CHEASE, and $R_m/R_0 - 1.1014865 = 0.1378h^2$ for CLIO. Therefore, CLIO gives an error of $\Delta R_m \simeq 1.5 \cdot 10^{-6}$ in the magnetic axis position with a 300×300 mesh, while CHEASE reaches a comparable precision on a 22×22 mesh. The resolution time on CRAY-2 for this equilibrium is 6.5 cpu seconds with CHEASE and about 400 seconds with CLIO.

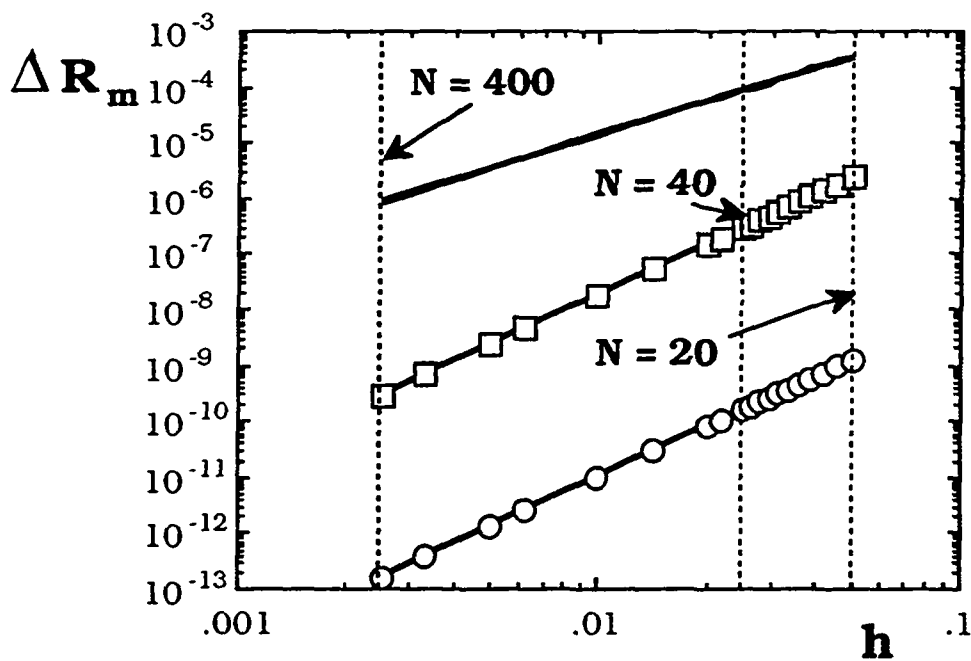


Figure 2.6: Comparison of the error in the magnetic axis between CLIO and CHEASE for a Solovev and a nonlinear JET equilibrium. The full line represents the error with CLIO for both cases. The open circles (squares) show the error with CHEASE for the Solovev (JET) equilibrium.

Chapter 3

Mapping of the equilibrium solution into flux coordinates

In this Chapter, the mapping of the equilibrium to (Ψ, χ, Φ) coordinates is presented. It will be shown that the mapping in CHEASE preserves the convergence rate of the bicubic Hermite elements used for the equilibrium discretization. This is illustrated by convergence tests of eigenvalues computed by MHD stability codes when the equilibrium mesh is refined and the stability mesh is held fixed.

3.1 Linear stability formulation

CHEASE provides the equilibrium quantities for the stability codes ERATO (ideal MHD) [37], MARS (resistive MHD) [36] and for LION (Alfvén and ion cyclotron range of frequencies) [38]. These codes consider the time evolution of small perturbations of the equilibrium. In the case of resistive MHD, the linearized system derived from eq.(1.2) is

$$\begin{aligned} \rho_0 \frac{\partial \mathbf{v}}{\partial t} &= (\nabla \times \mathbf{B}_1) \times \mathbf{B}_0 + \mathbf{J}_0 \times \mathbf{B}_1 - \nabla p_1 \\ \frac{\partial p_1}{\partial t} &= -\mathbf{v} \cdot \nabla p_0 - \Gamma p_0 \nabla \cdot \mathbf{v} \\ \frac{\partial \mathbf{B}_1}{\partial t} &= \nabla \times (\mathbf{v} \times \mathbf{B}_0) - \nabla \times \eta (\nabla \times \mathbf{B}_1) \\ \nabla \cdot \mathbf{B}_1 &= 0 \end{aligned} \tag{3.1}$$

In the special case where the resistivity $\eta = 0$, substituting the two last equations of (3.1) into the equation of motion gives the equation of evolution for the Lagrangian

displacement $\xi(\mathbf{r}_o, t)$ defined by $\mathbf{r}(t) = \mathbf{r}_o + \xi(\mathbf{r}_o, t)$:

$$\rho_0 \frac{\partial^2 \xi}{\partial t^2} = \nabla(\Gamma p_0 \nabla \cdot \xi + \xi \cdot \nabla p_0) + \mathbf{J}_o \times [\nabla \times (\xi \times \mathbf{B}_o)] + \{\nabla \times [\nabla \times (\xi \times \mathbf{B}_o)]\} \times \mathbf{B}_o. \quad (3.2)$$

Equations (3.1) and (3.2) should be supplied with boundary and initial conditions. The initial conditions are given by specifying $p_1(\mathbf{r})$, $\mathbf{v}(\mathbf{r})$, $\xi(\mathbf{r})$, $\mathbf{B}_1(\mathbf{r})$ at $t = 0$.

Consider a plasma isolated from a perfectly conducting wall S_v by a vacuum region. In the vacuum, the perturbed magnetic field $\mathbf{B}_{v1}(\mathbf{r}, t)$ fulfills

$$\begin{aligned} \nabla \times \mathbf{B}_{v1} &= 0 \\ \nabla \cdot \mathbf{B}_{v1} &= 0. \end{aligned} \quad (3.3)$$

The boundary condition on the conducting wall S_v is

$$\mathbf{n} \cdot \mathbf{B}_{v1} = 0. \quad (3.4)$$

Moreover, on the plasma-vacuum interface S_p , the pressure balance must be satisfied, i.e.

$$p(\mathbf{r}, t) + \frac{\mathbf{B}^2(\mathbf{r}, t)}{2} = \frac{\mathbf{B}_v^2(\mathbf{r}, t)}{2} \quad (3.5)$$

and the tangential component of the electric field in the moving system must be continuous:

$$\mathbf{n} \cdot \frac{\partial \mathbf{B}_{v1}}{\partial t} = (\mathbf{B}_o \cdot \nabla)(\mathbf{n} \cdot \mathbf{v}) \quad (3.6)$$

or in terms of $\xi(\mathbf{r}_o, t)$:

$$\mathbf{n} \cdot \mathbf{B}_{v1} = (\mathbf{B}_o \cdot \nabla)(\mathbf{n} \cdot \xi) \quad (3.7)$$

If a perfectly conducting wall S_p surrounds the plasma, the boundary conditions are simply

$$\begin{aligned} \mathbf{n} \cdot \mathbf{B}_1 &= 0 \\ \mathbf{n} \cdot \mathbf{v} &= 0 \\ \mathbf{n} \cdot \xi &= 0. \end{aligned} \quad (3.8)$$

The stability codes ERATO and MARS compute eigenmodes with temporal variation $e^{\gamma t}$. MARS solves the system (3.1;3.3-3.8) using a Fourier decomposition in the poloidal direction, and linear finite elements with a tunable integration scheme in the radial

direction [48]. ERATO uses a variational technique for the resolution of eq.(3.2-3.8). The discretization is done with the so-called "hybrid finite elements" in both the radial and poloidal directions. LION solves the linear field equation

$$\nabla \times (\nabla \times \mathbf{E}) = \underline{\underline{\epsilon}} \mathbf{E} \quad (3.9)$$

where $\underline{\underline{\epsilon}}$ is the cold plasma dielectric tensor for several ion species. This code requires the same equilibrium quantities as ERATO.

In all the following stability calculations, the mass density ρ is constant in space.

3.2 Flux coordinates

The flux coordinate system used by ERATO, MARS and LION differs completely from the one used for the equilibrium calculation. The radial stability coordinate of these codes is

$$s = \sqrt{\frac{|\Psi_{min} - \Psi|}{|\Psi_{min}|}} \quad (3.10)$$

The angular variable χ is specified by the choice of the Jacobian $J = [(\nabla\Psi \times \nabla\chi) \cdot \nabla\Phi]^{-1}$ of the mapping from (Ψ, χ, Φ) space to Cartesian coordinates. The contravariant metric tensor of these coordinates is given by

$$\begin{aligned} (g^{ij}) &= \begin{pmatrix} |\nabla\Psi|^2 & \nabla\Psi \cdot \nabla\chi & 0 \\ \nabla\Psi \cdot \nabla\chi & |\nabla\chi|^2 & 0 \\ 0 & 0 & |\nabla\Phi|^2 \end{pmatrix} \\ &= \begin{pmatrix} |\nabla\Psi|^2 & |\nabla\Psi|^2 \beta_{\Psi\chi} & 0 \\ |\nabla\Psi|^2 \beta_{\Psi\chi} & \beta_{\Psi\chi}^2 |\nabla\Psi|^2 + \frac{R^2}{J^2 |\nabla\Psi|^2} & 0 \\ 0 & 0 & \frac{1}{R^2} \end{pmatrix} \end{aligned} \quad (3.11)$$

where

$$\beta_{\Psi\chi} = \frac{\nabla\Psi \cdot \nabla\chi}{|\nabla\Psi|^2}. \quad (3.12)$$

The covariant metric tensor $(g_{ij}) = J^2(g^{ij})^{-1}$ is obtained by inverting eq.(3.11). In CHEASE, J is restricted to

$$J = C(\Psi)R^\alpha|\nabla\Psi|^\mu \quad (3.13)$$

where α and μ are integers. $C(\Psi)$ is obtained by demanding that χ increases by 2π per poloidal turn. The angular stability coordinate χ and the non-orthogonality $\beta_{\Psi\chi}$ can be expressed in the equilibrium coordinates (σ, θ) :

$$\begin{aligned} \chi(\theta) &= \int_0^\theta \frac{R\sigma\rho_s^2(\theta')}{J\frac{\partial\Psi}{\partial\sigma}} d\theta' \\ \beta_{\Psi\chi}(\theta) &= \int_0^\theta \left\{ \frac{Rj_\Phi}{|\nabla\Psi|^2} + (2-\alpha) \left[\frac{\partial(\ln R)}{\partial\Psi} \right]_n - \right. \\ &\quad \left. (\mu+2) \left[\frac{\partial(\ln|\nabla\Psi|)}{\partial\Psi} \right]_n - \frac{C'(\Psi)}{C(\Psi)} \right\} \frac{R\sigma\rho_s^2(\theta')}{J\frac{\partial\Psi}{\partial\sigma}} d\theta' \end{aligned} \quad (3.14)$$

A derivation of eqs.(3.14) is given in Appendix B. The subscript n in eq.(3.14) stands for the normal derivative with respect to Ψ , j_Φ is defined by eq.(2.3) and $C'(\Psi)$ is derived from the periodicity condition $\beta_{\Psi\chi}(0) = \beta_{\Psi\chi}(2\pi)$.

3.3 Computation of flux surface integrals

For the equilibrium and the stability calculation, integrated quantities of the form

$$\mathcal{F}(\Psi = \text{const}, \chi) = \int_0^\chi f\left(\Psi, \frac{\partial\Psi}{\partial\sigma}, \frac{\partial\Psi}{\partial\theta}, \frac{\partial^2\Psi}{\partial\sigma\partial\theta}, \frac{\partial^2\Psi}{\partial\sigma^2}, \frac{\partial^2\Psi}{\partial\theta^2}\right) J d\chi' \quad (3.15)$$

are required, as for instance the poloidal stability angle χ or the non-orthogonality $\beta_{\Psi\chi}$ in eq.(3.14), the safety factor q (2.12) or the four integrals (2.15). To compute such integrals without losing the convergence rate of the cubic Hermite elements, a high order integration scheme, such as Gaussian quadratures, must be applied.

The error of a k point Gaussian quadrature is proportional to the $2k^{\text{th}}$ derivative of the integrand of eq.(3.15), and therefore discontinuities in these derivatives will destroy the convergence of the integration scheme. The finite element solution of eq.(2.3) has always the same continuity properties as the basis functions used for the discretization.

With bicubic Hermite elements, already the second derivatives $\partial^2\Psi/\partial\sigma^2$ and $\partial^2\Psi/\partial\theta^2$ are discontinuous at the (σ, θ) mesh cell edges. As a consequence, the only reliable numerical method for the integration of eq.(3.15) is to split the integration interval into a set of subintervals delimited by the intersections of the constant Ψ surfaces with the (σ, θ) cell edges. In this way, the discontinuities which may appear in the integrand of (3.15) are avoided, and a high order integration scheme can be employed.

3.4 Convergence Studies of the Mappings

To illustrate the convergence properties of the mapping itself, we first consider the Solovév equilibrium described in Section 2.6.1. This case avoids resolving the Grad-Shafranov equation (2.3), because analytic values for Ψ , $\partial\Psi/\partial\sigma$, $\partial\Psi/\partial\theta$ and $\partial^2\Psi/\partial\sigma\partial\theta$ can be substituted on the nodes of the equilibrium mesh. Consequently, the mappings can be decoupled from the equilibrium solver in this case, and the convergence properties of the equilibrium quantities as well as the accuracy of the integration scheme presented in Section 3.3 can be verified independently. The convergence properties of the mappings are checked by observing the growth rate (normalized to the Alfvén frequency $\omega_A = v_A/R_0$) of the most unstable linear eigenmode computed by ERATO or MARS. For this test, the stability meshes are kept fixed and the equilibrium mesh density is varied. We are not aware of a theoretical prediction for the convergence of the stability eigenvalues with the equilibrium mesh. For the three test cases, the χ coordinate defined by the constant volume Jacobian ($J = C(\Psi)$ or $\alpha = 0$ and $\mu = 0$ in eq.(3.13)) has been used. This gives good results for the stability calculations (better than with straight field lines, $J = C(\Psi)R^2$). The s mesh has been packed on all resonant q surfaces. For the Solovév test case (test case I), the growth rate for toroidal mode number $n = 3$ is computed, with a perfectly conducting wall on the plasma edge. The stability mesh is fixed to $N_s = 130$ radial and $N_\chi = 130$ intervals with ERATO, and $N_s = 130$ radial points and $N_m = 12$ Fourier components in the χ -direction with MARS. The errors in the growth rate obtained with the analytic solution on the equi-

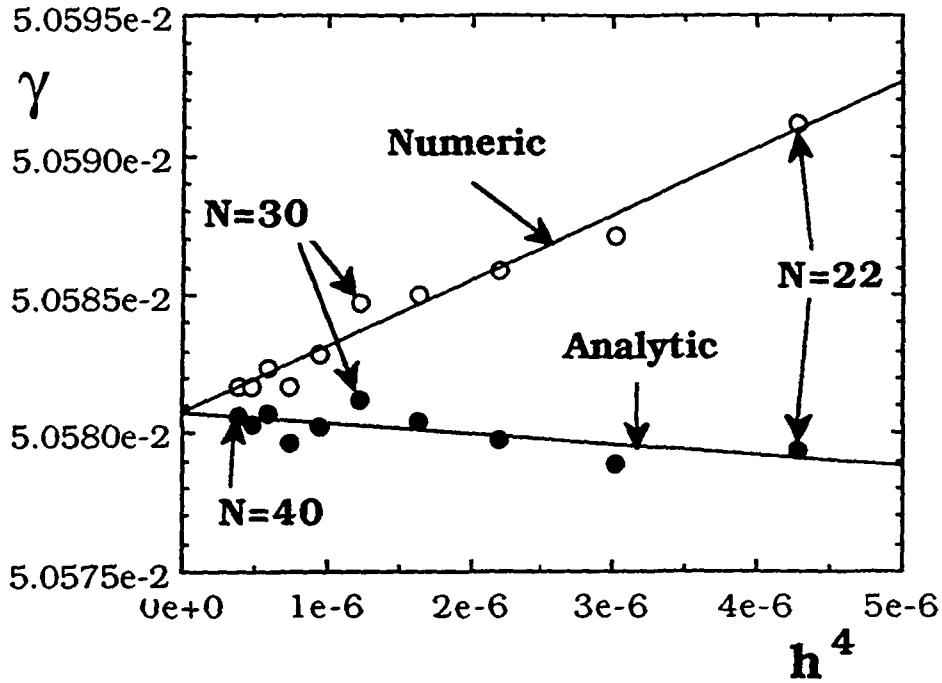


Figure 3.1: Convergence of the growth rate of the Solovev test case (test case I) with ERATO.

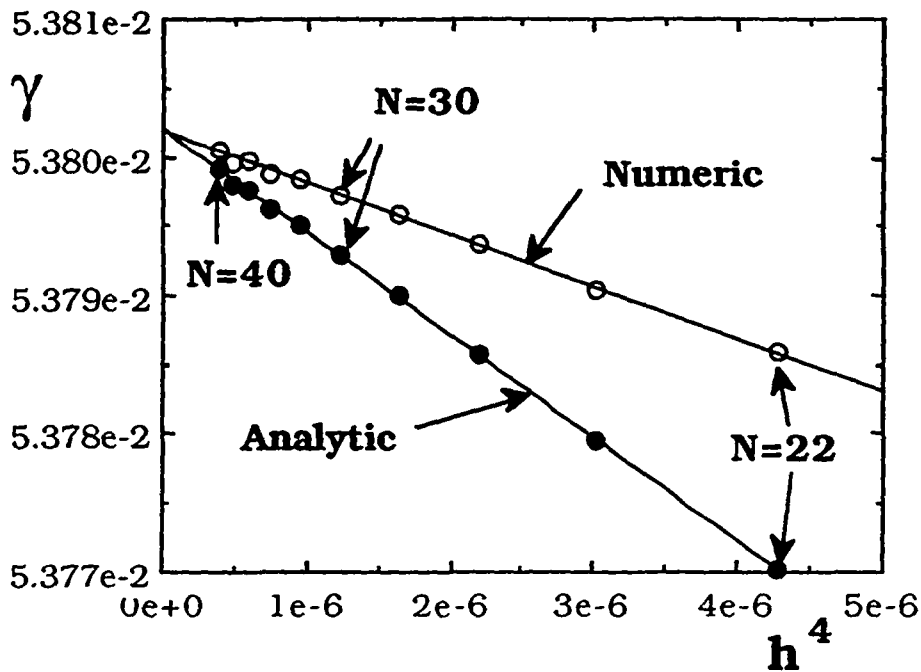


Figure 3.2: Convergence of the growth rate of the Solovev test case (test case I) with MARS.

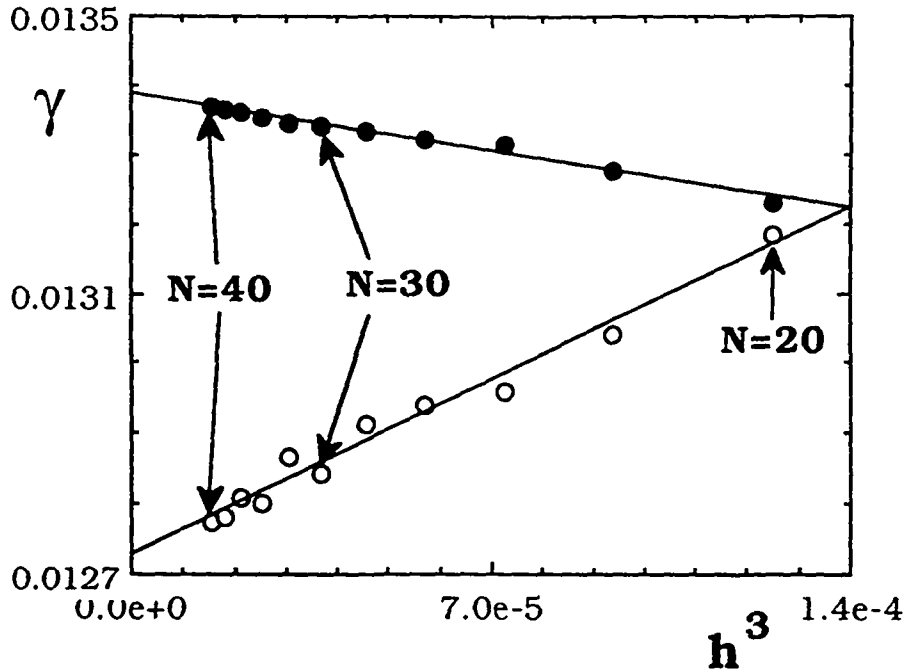


Figure 3.3: Convergences of growth rates of the test case II with ERATO (open circles) and MARS (full circles).

librium gridpoints (full circles in Figures 3.1 and 3.2) and with the numerical solution (open circles in Figures 3.1 and 3.2) converge to the same value as $\mathcal{O}(h^4)$ with some oscillations superimposed for ERATO. Figures 3.1 and 3.2 show that the error of the growth rate due to the equilibrium discretization on a $N_r = N_\theta = 22$ grid is of the order of 1.10^{-5} for both ERATO and MARS, which is negligible compared to the error due to the stability discretization.

The test case II described in Section 2.6.2 shows an $n = 1$ external kink instability with a perfectly conducting wall placed at one minor radius from the plasma surface. Figure 3.3 shows that the growth rates converge as $\mathcal{O}(h^3)$ with ERATO (open circles) and with MARS (full circles). Similar convergence properties are obtained for the test case III.

The values of the growth rates after convergence of the equilibrium are slightly different with ERATO and MARS because the discretization methods used in the two stability codes lead to different truncation errors. After convergence of the stability

calculations with fixed equilibrium mesh ($N_\sigma = N_\theta = 40$), both codes give the same growth rates: $\gamma = 5.395 \cdot 10^{-2}$ for the Solovév and $\gamma = 1.231 \cdot 10^{-2}$ for the test case II. It should be noted that 10^{-2} is a typical growth rate for production runs in the context of beta-limit studies.

3.5 Bicubic spline smoothing of the equilibrium solution. Effects on the stability results.

For certain instabilities, changing the density of the equilibrium mesh with the stability mesh kept constant gives large oscillations in the growth rate computed by ERATO. The origin of this problem is the cubic Hermite discretization used for the equilibrium resolution, which guarantees only continuous first order derivatives over the discretization mesh. Discontinuities in the second derivative of Ψ may deteriorate the convergence of the growth rate of ERATO when the equilibrium mesh is refined, since ERATO requires local equilibrium quantities which depend on these derivatives (see Table C.1).

A simple way to get rid of these oscillations is to interpolate the equilibrium solution with bicubic splines, which guarantee continuous first and second order derivatives over the discretization mesh. To effect this, the values of Ψ on the nodes obtained by the bicubic Hermite solution are interpolated by bicubic splines, and $\partial\Psi/\partial\sigma$, $\partial\Psi/\partial\theta$ and $\partial^2\Psi/\partial\sigma\partial\theta$ are reevaluated from the bicubic spline interpolations, as described in Appendix D. This smoothing does not alter the $\mathcal{O}(h^4)$ convergence of the bicubic Hermite elements. However, the slopes of the convergence curves are influenced.

As an example, the bicubic spline smoothing is applied to the following equilibrium:

- Test case IV: The plasma boundary (2.25) is chosen as $a/R_0 = 0.423$, $\kappa = 1.68$, $\delta = 0.3$, $\zeta = 0$ and the current density is specified by

$$\begin{aligned} p'(\Psi/\Psi_{min}) &= -0.06(\Psi/\Psi_{min}) \\ GG'(\Psi/\Psi_{min}) &= -0.45(\Psi/\Psi_{min}) + 0.174(\Psi/\Psi_{min})^2. \end{aligned} \tag{3.16}$$

This equilibrium has been rescaled so that the safety factor on axis is $q_0 = 0.85$.

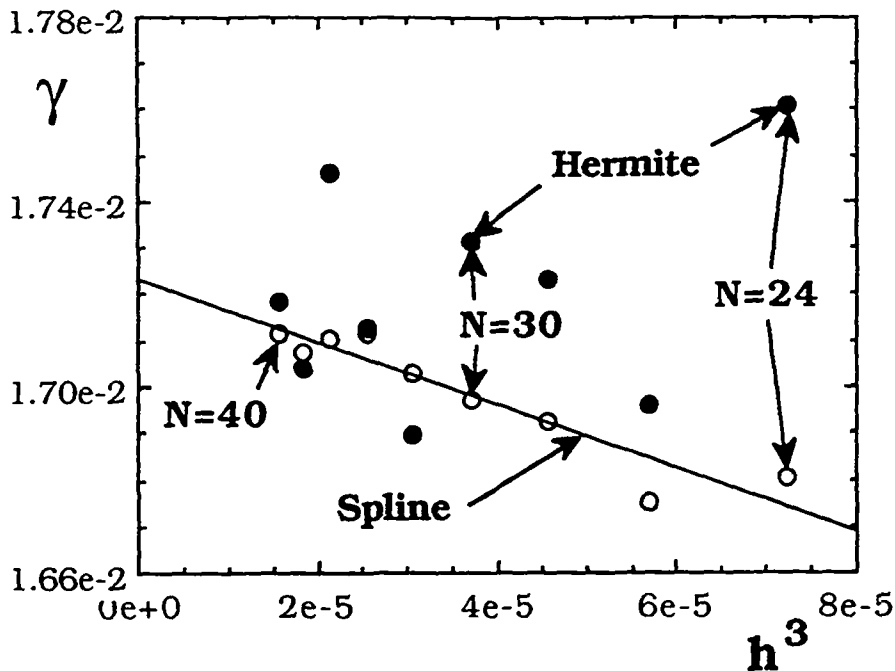


Figure 3.4: Convergence of ERATO growth rates for test case IV with a Hermite (full circles) and a 2-D spline smoothed (open circles) equilibrium solution.

Figure 3.4 shows that for this equilibrium, the growth rate of ERATO is not converging with the Hermite equilibrium solution, whereas for the smoothed solution, the convergence rate is $\mathcal{O}(h^3)$.

Similar tests with MARS have shown that smoothing Ψ with bicubic splines deteriorates slightly the $\mathcal{O}(h^3)$ convergence slope of the growth rate when the equilibrium mesh is refined.

3.6 Comparison of the error on the growth rate of ERATO due to CHEASE and to EQLAUS

It is interesting to compare the results of Section 3.4 with those obtained by other codes. The equilibrium code EQLAUS [26] combined with ERATO is used for such a comparison with CHEASE. EQLAUS uses a finite difference scheme in Cartesian coordinates for the discretization. The nonlinear JET case (test case II) shown in Section 2.6 has been reproduced with this numerical package. The ERATO mesh has

been fixed ($N_s = N_x = 130$), and the same radial stability mesh packing was used as for CHEASE.

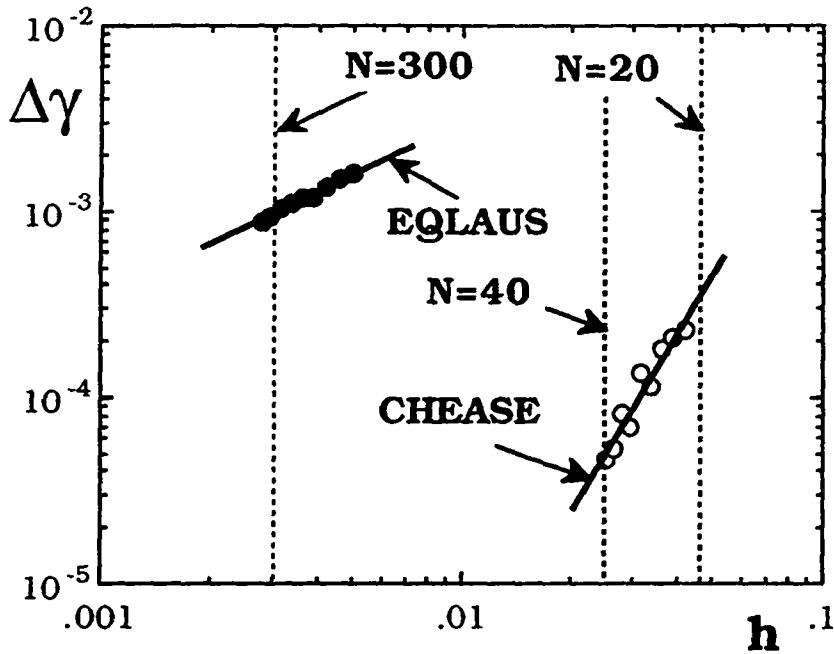


Figure 3.5: Absolute value of the error in the growth rate due to the equilibrium discretization with CHEASE (open circles) and EQLAUS (full circles) for test case II.

For the test case II, the absolute value of the error in the growth rate behaves as $|\gamma - 1.273 \cdot 10^{-2}| = 0.322h$ with EQLAUS & ERATO and $|\gamma - 1.273 \cdot 10^{-2}| = 3.469h^3$ with CHEASE & ERATO (see Figure 3.5). Thus, the error in the growth rate due to EQLAUS is of about $\Delta\gamma = 1 \cdot 10^{-3}$ on a 300×300 mesh. This precision is already reached on a 20×20 mesh with CHEASE and ERATO. On CRAY-2, the computation of a 300×300 case with EQLAUS takes about 300 cpu seconds, while a 20×20 case with CHEASE requires only about 20 seconds, including in both cases the computation of the stability input quantities, ballooning and local stability criteria.

3.7 Ballooning Stability, Mercier and Resistive Interchange Criteria

Ballooning modes are toroidal modes with infinite toroidal mode number n [49,50]. The potential energy for these modes is given by (see Appendix E)

$$\delta W_p(n \rightarrow \infty) = \frac{1}{2} \int_{-\infty}^{+\infty} \left\{ c_1 \left| \frac{\partial \xi}{\partial \chi} \right|^2 + c_2 |\xi|^2 \right\} J d\chi \quad (3.17)$$

where ξ is the radial component of the displacement vector, and χ is a generalized poloidal angle extending from $-\infty$ to $+\infty$. For ballooning stability, δW_p must be positive definite on every flux surface. The quantities appearing in (3.17) are [49]

$$\begin{aligned} \nu &= \frac{JG}{R^2} \\ B^2 &= \frac{1}{R^2} [G^2 + |\nabla\Psi|^2] \\ c_1 &= \frac{1}{J^2 |\nabla\Psi|^2} \left(1 + \frac{|\nabla\Psi|^4}{B^2} g^2 \right) \\ c_2 &= -\frac{2p'}{B^2} \left[\left(\frac{\partial \tilde{P}}{\partial \Psi} \right) - \frac{gG}{B^2} \frac{1}{J} \left(\frac{\partial \tilde{P}}{\partial \chi} \right)_{\Psi} \right] \\ g &= \nu \beta_{\Psi\chi} + \int_{\chi_0}^{\chi} \left(\frac{\partial \nu}{\partial \Psi} \right)_{\chi} d\chi' \\ \tilde{P} &= p + \frac{B^2}{2} \end{aligned} \quad (3.18)$$

The integral (3.17) is solved on the $(\Psi; \chi)$ mesh of ERATO by a hybrid linear finite element method. The infinite χ integration interval of (3.17) is replaced by a finite one specified as input (normally $20 \times 2\pi$) outside which ξ is set to zero. For the arbitrary angle χ_0 , 25 different values are tested on every constant Ψ surface. The diagonalization of the matrix corresponding to the first variation of (3.17) is not unique, but according to Sylvester's theorem [51], the number of negative terms in the diagonal matrix is invariant and equal to the number of unstable ballooning modes on the particular poloidal flux surface.

The Mercier stability [13] and the resistive interchange criterion [12] are checked on every constant poloidal flux surface. These criteria can be expressed in terms of the

integrals

$$\left\{ J_1, J_2, J_3, J_4, J_5, J_6 \right\} = \frac{1}{2\pi} \oint_{\Psi=\text{const}} \left\{ \frac{1}{R^2 |\nabla \Psi|^2}, \frac{1}{|\nabla \Psi|^2}, \frac{R^2}{|\nabla \Psi|^2}, \frac{1}{R^2}, 1, \frac{|\nabla \Psi|^2}{R^2} \right\} J d\chi. \quad (3.19)$$

A given flux surface is stable to ideal interchanges if the Mercier criterion $-D_I > 0$, where

$$-D_I = \left(\frac{p' G J_2}{q'} - \frac{1}{2} \right)^2 + \frac{p'}{q'^2} (J_5' - p' J_3) (G^2 J_1 + J_4) \quad (3.20)$$

A derivation of the Mercier criterion is given in Appendix E. Resistive interchanges are stable if $-D_R > 0$, with

$$-D_R = -D_I - (H - 1/2)^2 \quad (3.21)$$

and

$$H = \frac{G p'}{q'} \left(J_2 - \frac{J_5 (J_4 + G^2 J_1)}{J_6 + G^2 J_4} \right) \quad (3.22)$$

The prime in eqs.(3.20,3.22) denotes the derivative with respect to Ψ .

Chapter 4

Ideal MHD stability of internal kinks in circular and shaped tokamaks

The second part of this thesis concerns beta-limits of internal kink instabilities. In Chapter 4, numerical results show that in many cases, the internal kink is more unstable than previously assumed. This holds, in particular, for elliptically shaped cross sections. A partial analytic explanation is given in Chapter 5, where the Mercier criterion (3.20) is derived in the large aspect ratio limit, showing the significant destabilization by ellipticity. Finally, in Chapter 6, effects due to resistivity on the internal kink mode are reported.

At present, essentially all the analytical work on ideal internal kink modes in a tokamak has been carried out in the large aspect ratio limit. In a pioneering work, Bussac et al. [11] found the pressure limit for internal kink stability in circular equilibria. The calculations of central stability performed by Laval et al. [52] indicate an significant destabilizing effect of ellipticity and a stabilizing effect of triangularity. Conversely, a more recent calculation of Connor and Hastie predicts only a very weak destabilizing effect of elliptic shaping [18].

To some extent, the uncertainties concerning the internal kink stability can be explained by the difficulty of computing these modes numerically, because their growth rate is typically below $\gamma/\omega_A = 10^{-2}$, where $\omega_A = v_A/R_0$ is the toroidal Alfvén fre-

quency. Nevertheless, Berger et al. [16] found a strong destabilizing effect by ellipticity by numerical calculations in the special case of Solovév equilibria [17]. However, no systematic study has been undertaken for equilibrium solutions with more realistic profiles and shaped plasma cross sections, and therefore, strong numerical arguments for the confirmation or the invalidation of the analytical results were hitherto nonexistent.

The purpose of this Chapter is to present calculations of ideal MHD stability limits for the internal kink mode for tokamaks with different current profiles and plasma cross sections. The bicubic Hermite element code CHEASE [34] and the toroidal resistive stability code MARS [36] are powerful tools for such a study, and allow routine computation of ideal MHD growth rates down to $5 \cdot 10^{-4} \omega_A$.

In the following, β_p denotes the poloidal beta on the $q = 1$ surface, defined, in the general case, as in Table 2.1.

4.1 Circular cross section - Large aspect ratio expansion

Stability limits for the internal kink mode have been calculated by means of the large aspect ratio expansion [11] taking into account the toroidal coupling of the dominant $m = 1$ displacement ($m =$ poloidal mode number) to the $m = 0$ and $m = 2$ side-bands. For a parabolic current profile, Bussac et al. [11] found that the marginal stable value of β_p , the poloidal beta on the $q = 1$ surface, is $\beta_p = (13/144)^{1/2} \approx 0.3$ when $r_{q=1} \ll a$, falls to a minimum of about 0.23 for $r_{q=1}/a \approx 0.4$, and then increases again for larger $q = 1$ radii. For profiles that are more peaked than parabolic, the pressure limit decreases more sharply with $r_{q=1}$. Very steep current profiles, such as the Shafranov (step-function) profile are less stable [39].

The stability diagram ($\beta_{p,crit}$ versus $r_{q=1}/a$) of Bussac et al. [11] was computed assuming a fixed boundary. With this assumption, the $m = 2$ side-band is wall stabilized whenever $q(r = a) \equiv q_a < 2$. For the parabolic current profile, $q_a/q_0 = 2$, and therefore $q_a < 2$ holds if $q_0 < 1$, i.e., in all cases of interest for the internal kink. Evidently,

the results in [11] for the parabolic profile refer to the non-standard case of very low q operation, $q_a < 2$, with a close-fitting wall. Although tokamaks can be operated this way, the standard operating regime is $q_a > 2$.

For comparison with the finite aspect ratio computations, we show the β_p -limit obtained from large aspect ratio theory and boundary conditions appropriate for $q_a > 2$. The potential energy for the large aspect ratio $n = 1$ ideal internal kink mode was calculated by Bussac et al. [11]. It is a quadratic polynomial in β_p :

$$\delta W_p = \frac{\pi^2}{2} R_0 |\xi|^2 B_0^2 \varepsilon^4 P_T(\beta_p) \quad (4.1)$$

where $\varepsilon = r_{q=1}/R_0$, R_0 is the major radius, ξ the amplitude of the $m = 1$ radial displacement ($m =$ poloidal mode number), and

$$P_T(\beta_p) = -3\beta_p - \hat{S} - \frac{[3(\beta_p + \hat{S} - 1/4) + (\beta_p + \hat{S} + 3/4)A_i] [3(\beta_p + \hat{S} - 1/4) + (\beta_p + \hat{S} + 3/4)A_e]}{A_i - A_e} \quad (4.2)$$

where

$$\beta_p = -\frac{2}{B_p^2(r_{q=1})} \int_0^{r_{q=1}} \frac{r^2}{r_{q=1}^2} \frac{dp}{dr} dr \quad (4.3)$$

is the poloidal beta on the $q = 1$ surface and

$$\hat{S} \equiv \int_0^{r_{q=1}} \frac{r^3}{r_{q=1}^4} \left[\frac{1}{q^2} - 1 \right] dr. \quad (4.4)$$

The quantity \hat{S} measures the shear inside the $q = 1$ in a global sense. A_e and A_i are the logarithmic derivatives $r d(\ln \xi)/dr$ of the ($m = 2, n = 1$) component of the radial displacement just outside and inside the $q = 1$ surface, respectively. They are obtained from the solutions of the cylindrical Euler equation

$$\frac{d}{dr} \left(r^3 F^2 \frac{d\xi}{dr} \right) - r(m^2 - 1)F^2 \xi = 0 \quad (4.5)$$

where

$$F = \mathbf{k} \cdot \mathbf{B} = \frac{B_0}{R_0} \left(\frac{m}{q} - n \right) \quad (4.6)$$

for ($m = 2, n = 1$) in the two separate regions $q > 1$ and $q < 1$ with appropriate boundary conditions.

For the Shafranov equilibrium, the logarithmic derivatives A_i and A_e can be obtained analytically [39]. However, for more general current densities, the solution of the Euler equation (4.5) must be carried out numerically. Figure 4.1 shows the β_p -limit obtained from the large aspect ratio theory plotted (a) versus $r_{q=1}/a$, and (b) versus q_0 , using boundary conditions appropriate for $q_a > 2$, with the $q = 2$ surface inside the conducting plasma. (If $q_a < 2$, a region of currentless but perfectly conducting plasma that extends to the $q = 2$ surface at $r/a = (2/q_a)^{1/2}$ is added). Three different current profiles are considered: two polynomial profiles,

$$j_\Phi(r) = \begin{cases} j_0(1 - r^2/a^2)^l & \text{if } r < a \\ 0 & \text{if } r > a \end{cases} \quad (4.7)$$

with $l = 1, 2$ (parabolic and parabolic-squared for which $q_a = (l + 1)q_0$), and the

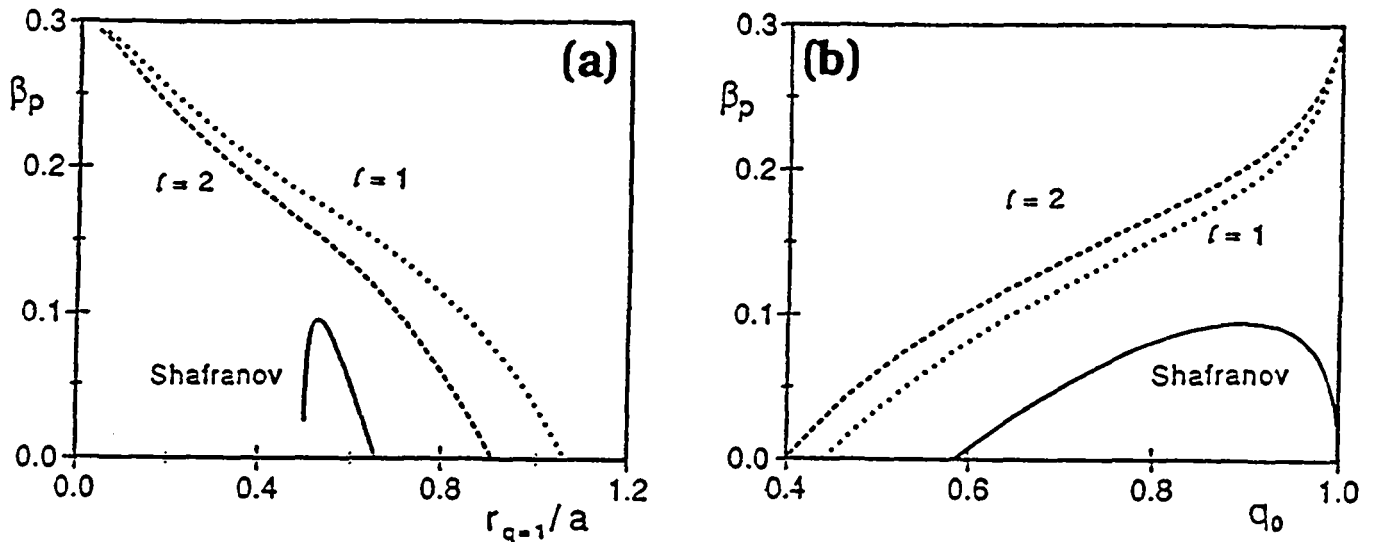


Figure 4.1: Marginal β_p for circular equilibria from large aspect ratio theory. Results are given for three current profiles: Shafranov (with a step at $r_0 = a/2$), parabolic ($l = 1$) and parabolic-squared ($l = 2$), in (a) versus $r_{q=1}/a$ and in (b) versus q_0 .

Shafranov profile, with the step in the current density at $r = 0.5a$. For the two smooth profiles (4.7), the β_p -limit falls monotonically when the $q = 1$ radius increases, as shown

in Figure 4.1(a). This is in clear contrast to the fixed boundary result of Bussac et al. [11], where the stabilization by the wall at $r = a$ becomes stronger with increasing $q = 1$ radius, and the pressure limit even becomes infinite for $r_{q=1}/a > 0.79$. With the modified treatment of the wall, “typical” limits in the range of 0.1 to 0.2 are found rather than the usually-quoted value 0.3 which is valid as $r_{q=1} \rightarrow 0$.

Figure 4.1(b) shows that the β_p -limit goes to zero for q_0 below some profile-dependent threshold, ranging from 0.40 for the parabolic-squared profile to 0.58 for the Shafranov profile. For q_0 close to unity, the pressure limit is highly sensitive to the current profile: the Shafranov profile gives much lower values than the rounded-off current profiles (4.7).

4.2 Finite aspect ratio calculations - definitions

Here, we show the full-MHD stability limits for the internal kink at finite aspect ratio calculated using the stability code MARS [36] and the equilibrium code CHEASE [34]. The plasma-vacuum interface in equilibrium is prescribed by eq.(2.25). Results will be presented for two geometries corresponding to the TEXTOR tokamak: $R_0/a = 4$, $\kappa = 1$, $\delta = 0$, $\zeta = 0$ (medium aspect ratio circle), and JET [53]: $R_0/a = 2.7$, $\kappa = 1.7$, $\delta = 0.3$, $\zeta = 0$ (small aspect ratio dee).

In all cases, the same shape is used for the pressure profile p/p_0 . The pressure is prescribed as a function of the poloidal flux Ψ , so that $dp/d\Psi$ is constant in the central region and falls smoothly to zero at the edge. Figure 4.2 shows the pressure versus the normalized minor radius ρ .

The current profiles are specified by the surface averaged toroidal current density I^* (2.13). $I^*(\Psi/\Psi_{\text{axis}})$ is prescribed except for a multiplicative factor that is adjusted to specify the $q = 1$ radius, using the equilibrium transformations described in Section 2.5.

The stability diagrams presented in the following give β_p as a function of the $q = 1$ radius $\rho_{q=1}$ at constant growth rates, $\gamma/\omega_A = 0, 1.10^{-3}, 3.10^{-3}, 5.10^{-3}$, where

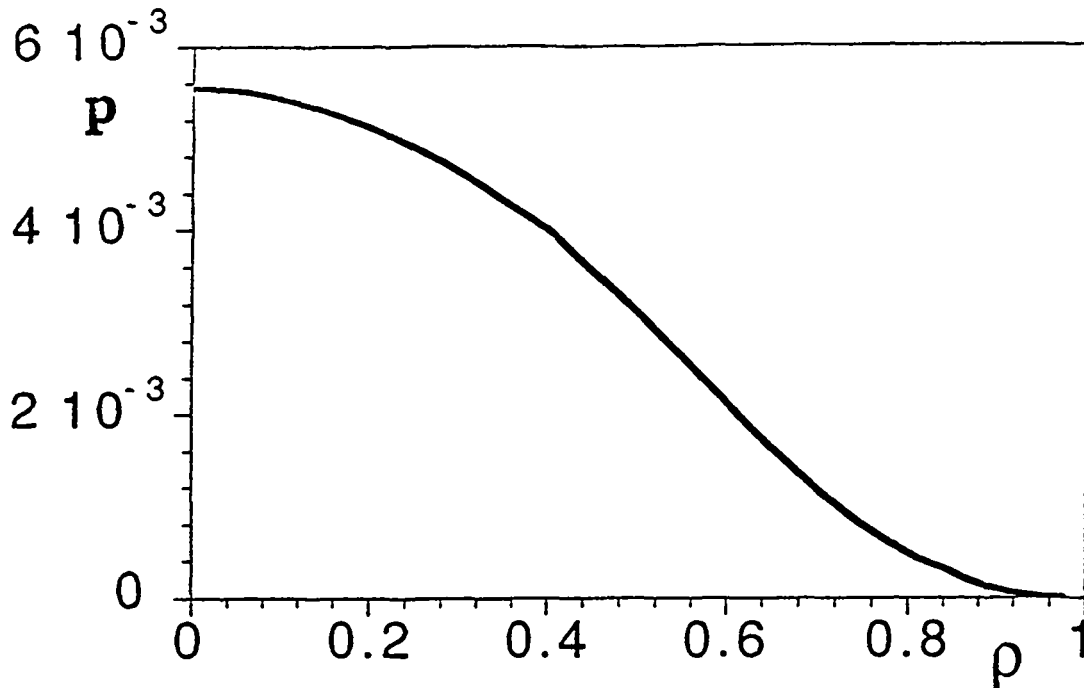


Figure 4.2: Pressure versus normalized minor radius ρ for the numerical equilibria.

$\omega_A = v_A/R_0$ is the toroidal Alfvén frequency. These curves have been obtained after interpolation of the computed values of $\gamma(\beta_p, \rho_{q=1})$ for equilibria with different β_p but identical I^* profiles.

Convergence studies have been carried out and the results are shown after extrapolation to zero mesh size. However, it must be admitted that ideal-MHD growth rates of the order $10^{-3}\omega_A$ are non-trivial to compute. Our results for $\gamma = 10^{-3}\omega_A$ should be reliable, but in certain cases, extrapolation to marginal stability is somewhat uncertain. This may be acceptable from a physics point of view, since instabilities with very small growth rates must be expected to be strongly modified by non-MHD effects.

4.3 Circular cross section - Numerical results with finite aspect ratio

For a circular plasma, results will be shown for four different current profiles: one *rounded* profile, two profiles with I^* *flattened* at a certain radius, and a profile where

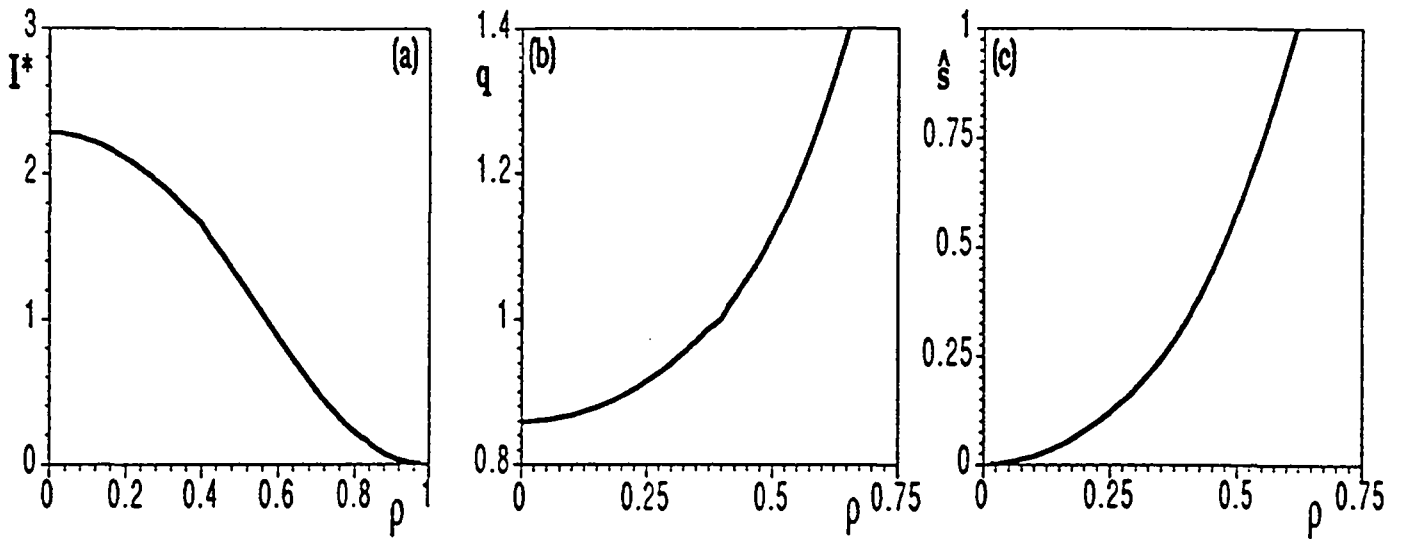


Figure 4.3: Profiles of (a) averaged toroidal current density I^* , (b) safety factor q and (c) shear \hat{s} versus ρ for the *rounded* current profile.

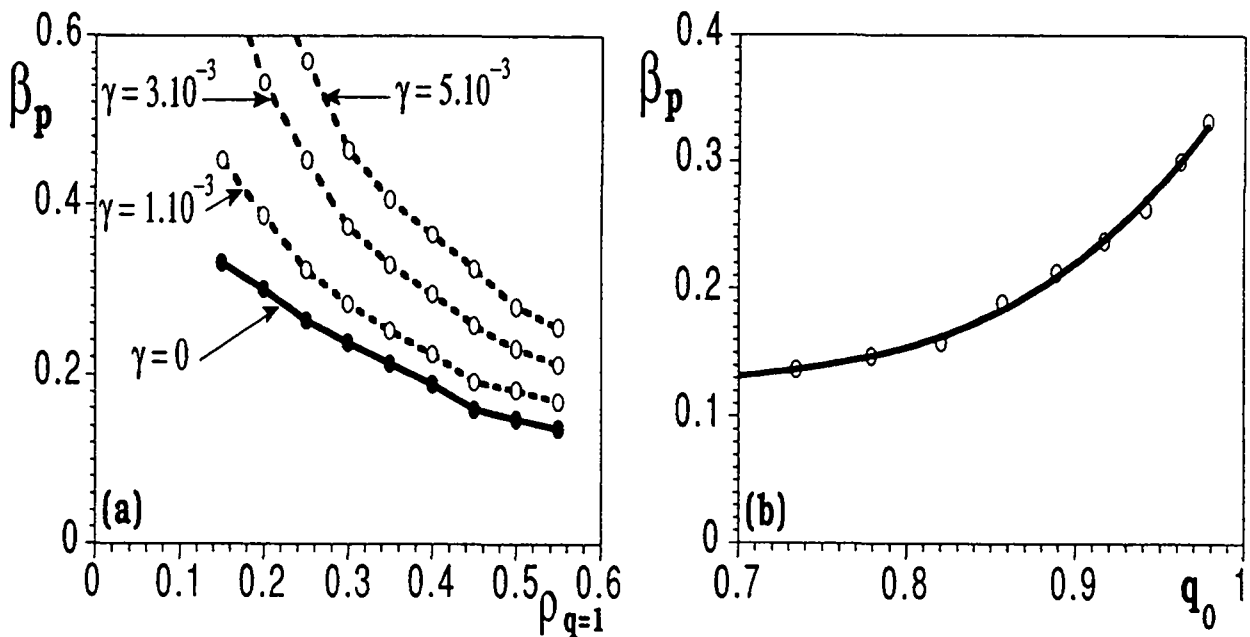


Figure 4.4: Stability limits in β_p for circular equilibrium with aspect ratio 4 and the *rounded* current profile shown in Figure 4.3: (a) β_p versus $\rho_{q=1}$ and (b) β_p versus q_0 .

I^* has *shoulders*, termed TEXTOR [5]. The aspect ratio of these equilibria is 4.

Figure 4.3 shows $I^*(\rho)$, $q(\rho)$ and $\hat{s}(\rho)$ for the *rounded* profile, and the corresponding stability results are shown in Figure 4.4. Both the current profile and the marginal stability curve are close to those for the parabolic-squared profile of Section 4.1. Figure 4.4(b) shows the marginal β_p versus q_0 , to be compared with Figure 4.1(b). Evidently, for an aspect ratio of 4 and circular boundary, the large aspect ratio theory is in good agreement with the full-MHD result.

Figure 4.5 shows an effect that is a higher order correction to the large aspect ratio result: the influence of the wall position for circular equilibria with $2 < q_a < 3$. The

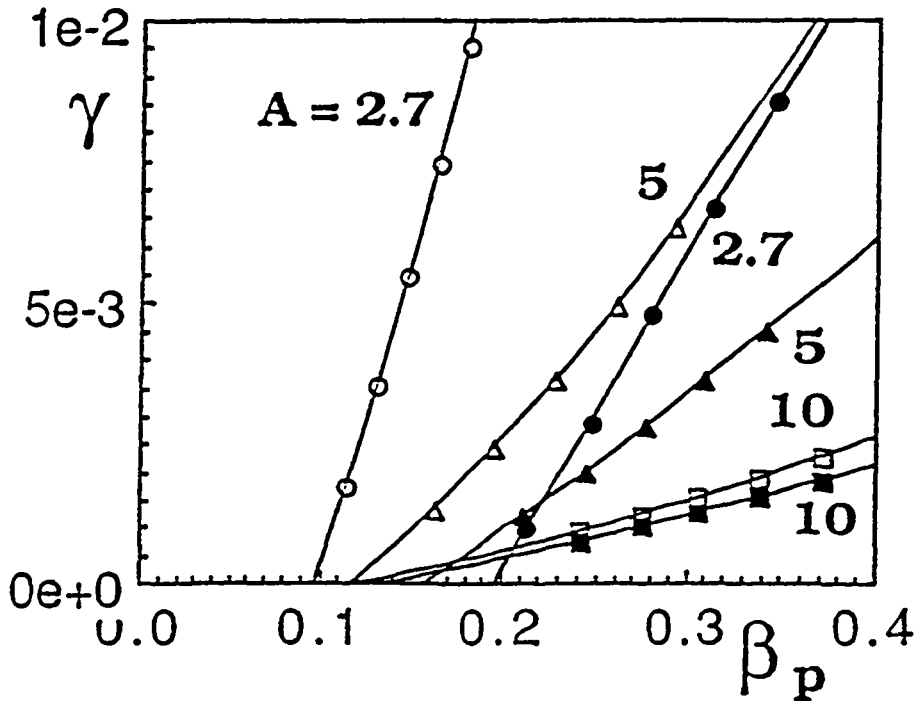


Figure 4.5: Internal kink growth rates versus β_p for a circular equilibrium with fixed boundary (filled symbols) and free boundary (open symbols). Three different aspect ratios are shown: $A = R_0/a = 10, 5$ and 2.7 and $\rho_{q=1} = 0.6$.

diagram shows the growth rates of the $n = 1$ internal kink for different aspect ratios and a circular boundary, with the boundary either fixed or free (and the conducting wall at infinity). For circular equilibria with $q_a > 2$, the large aspect ratio expansion to lowest order shows no effect of the wall position. According to Figure 4.5, this is a

good approximation at large aspect ratio, $A = 10$. A detailed analysis of the numerical results shows that the difference in marginal β_p between the free and the fixed boundary cases is proportional to $(a/R_0)^2$ at large aspect ratio. At tight aspect ratio, $A = 2.7$, the difference between fixed and free boundary results is appreciable: $\beta_p \approx 0.1$ for free boundary and $\beta_p \approx 0.2$ for fixed boundary. The numerical results show a very weak influence of the wall position for circular equilibria with $q_a > 3$.

Therefore, the wall position influences the internal kink stability for aspect ratios of interest only at low q_a . In the following, only configurations where the wall is placed at 20% of the minor radius away from the plasma are considered.

The *flattened* current profiles (Figure 4.6) have a plateau at a certain radius: $dI^*/d\rho = 0$ for $\rho = \rho_p \approx 0.42$. Inside this radius, the shear is rather uniform, and outside, it

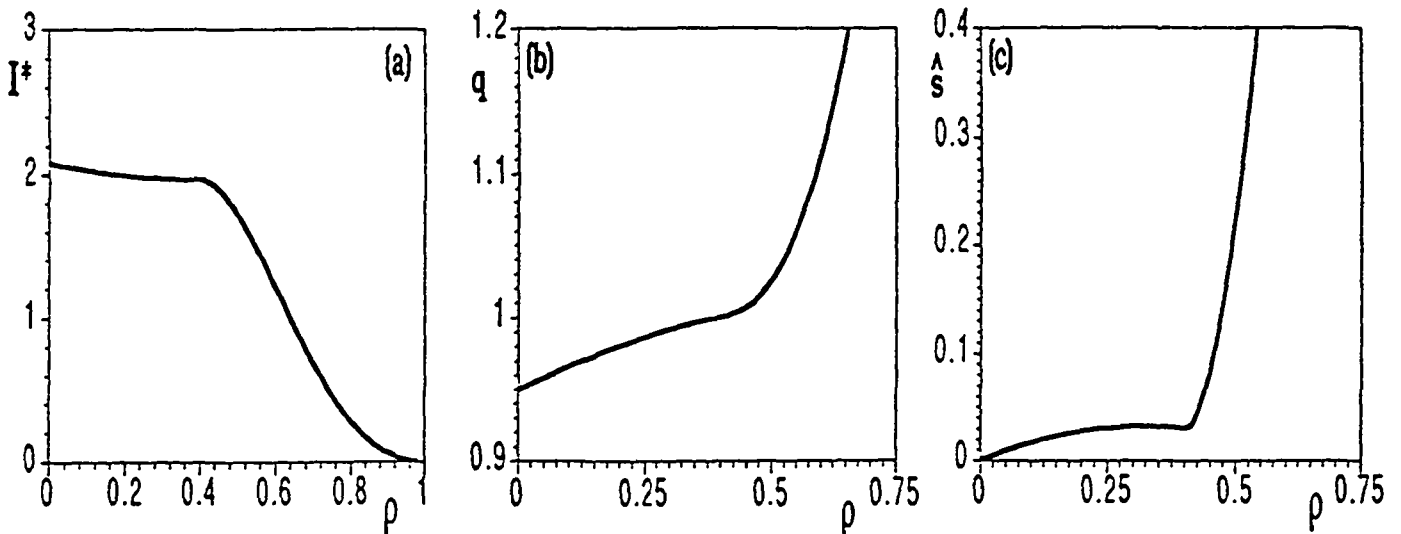


Figure 4.6: Profiles of (a) averaged toroidal current density I^* , (b) safety factor q and (c) shear \hat{s} versus ρ for the *flattened* current profile with *low central shear*

increases sharply. Two current profiles with different central shear are considered: one with *small central shear*, $q_0/q(\rho_p) \approx 0.95$, and one with *medium central shear*, $q_0/q(\rho_p) \approx 0.80$.

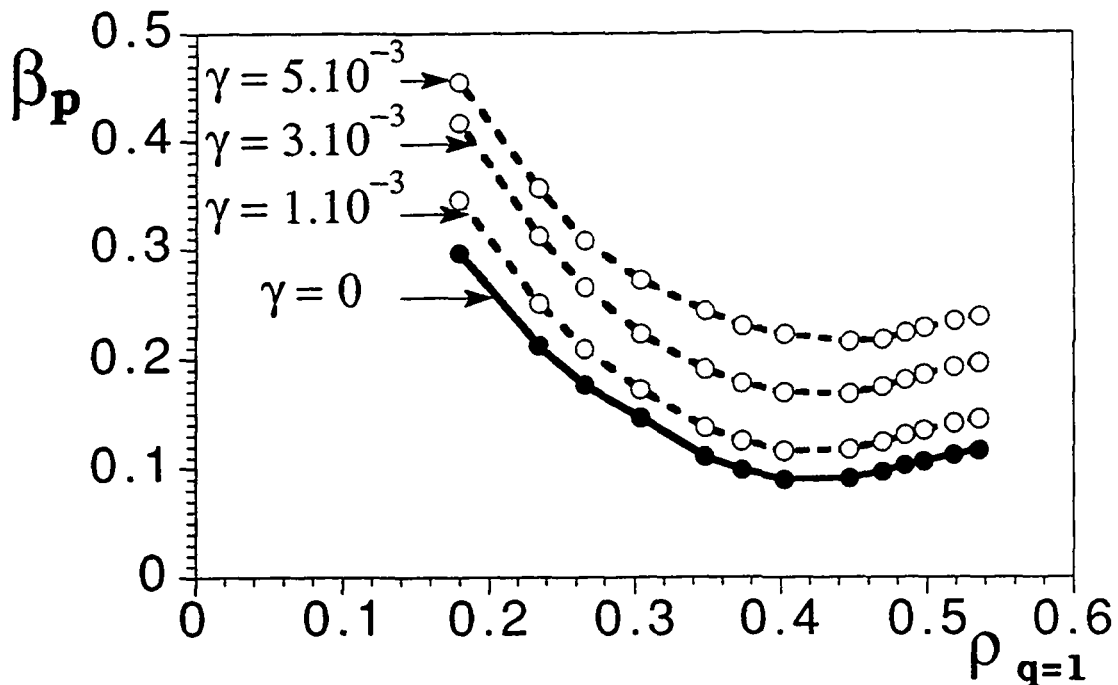


Figure 4.7: Stability limits in β_p for the *flattened* current profile with *low central shear*. The cross section is circular with aspect ratio 4.

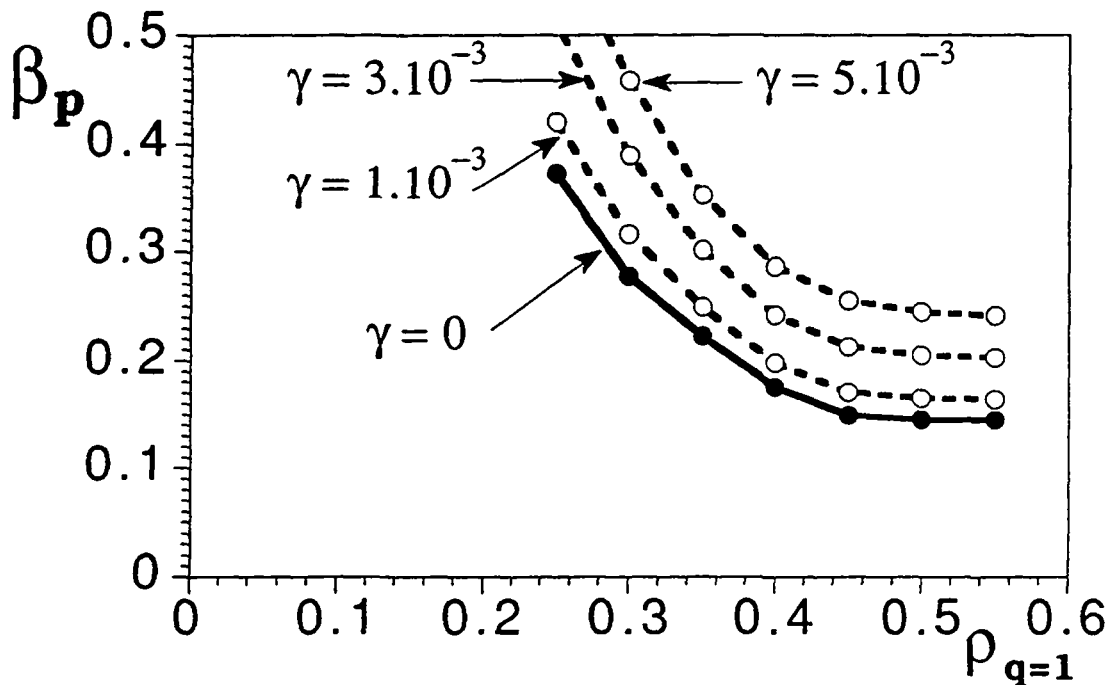


Figure 4.8: Stability limits in β_p for the *flattened* current profile with *medium central shear* (four times larger than in Figure 4.6). The cross section is circular with aspect ratio 4.

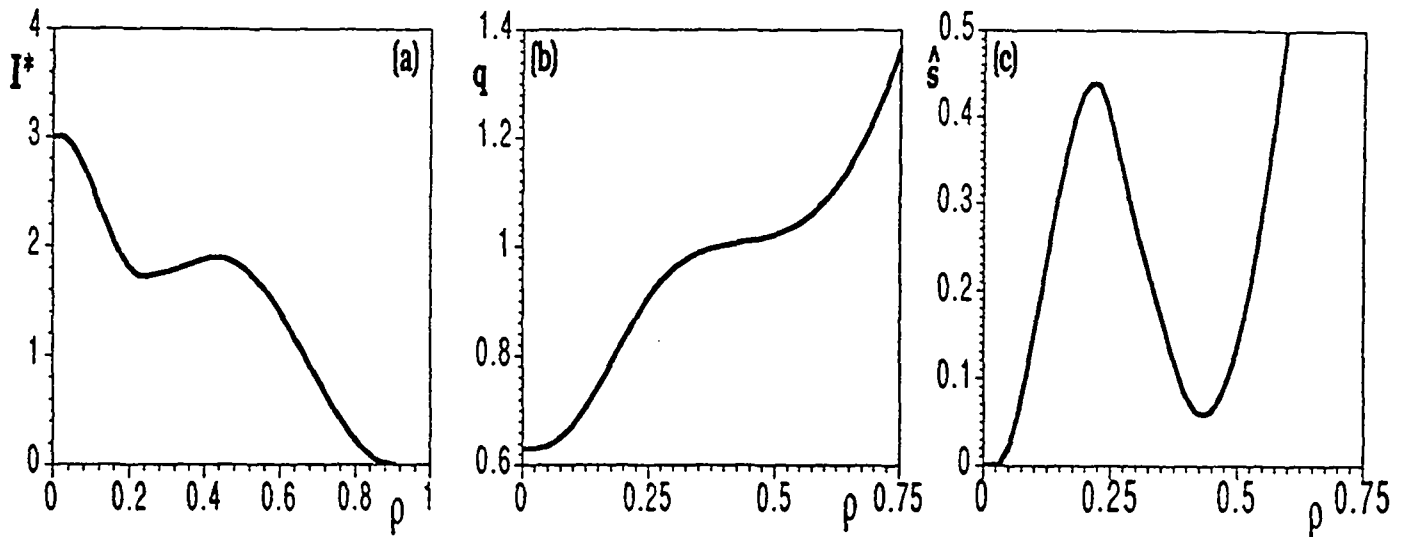


Figure 4.9: Profiles of (a) averaged toroidal current density I^* , (b) safety factor q and (c) shear \hat{s} versus ρ for the *TEXTOR* current profile.

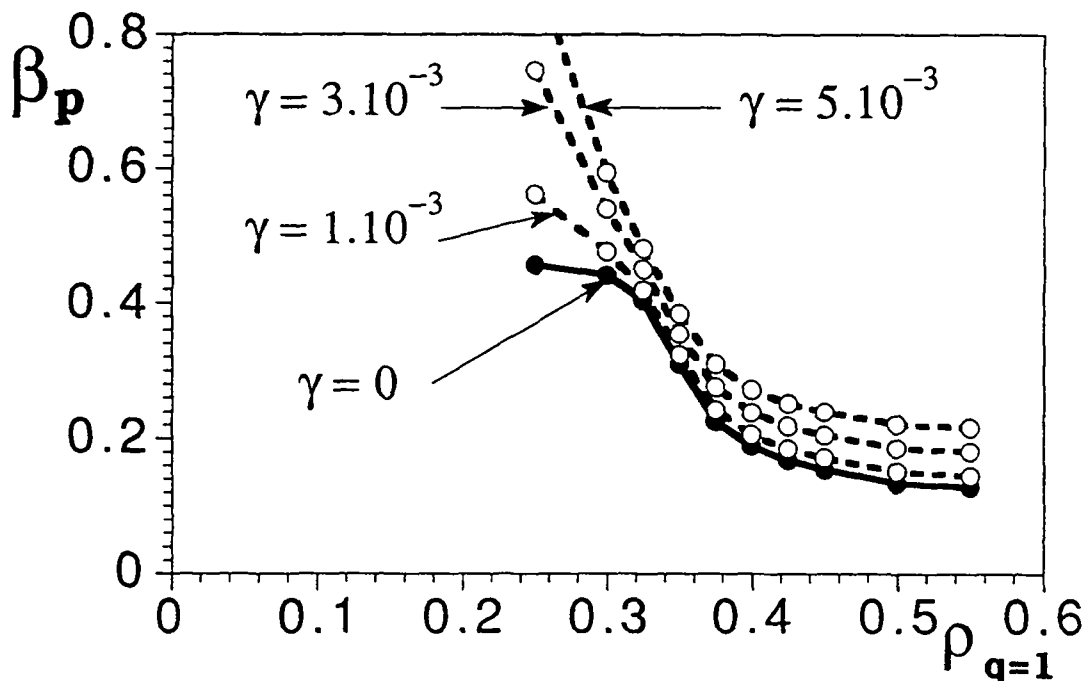


Figure 4.10: Stability limits in β_p for the *TEXTOR* current profile. The cross section is circular with aspect ratio 4.

Figure 4.6 shows $I^*(\rho)$, $q(\rho)$ and $\hat{s}(\rho)$ for the flattened profile with *low central shear* at aspect ratio 4 and the stability results are shown in Figure 4.7. The marginal β_p is similar to that for the rounded profile (Figure 4.4(a)) when the $q = 1$ surface is far away from the current plateau at $\rho_p \approx 0.42$, but when the $q = 1$ surface is near the plateau, $\beta_{p,crit}$ has a local minimum of about 0.08.

Figure 4.8 shows the stability for the *flattened* current profile with *medium central shear*. The equilibrium is similar to that in Figure 4.6 except that the central shear is four times larger. The limits in β_p are higher than for the low-shear equilibrium. They are quite similar to those for the rounded profile (Figures 4.3 and 4.4), except for slightly higher values when the $q = 1$ radius is small, due to the higher shear near the magnetic axis.

Finally, Figures 4.9 and 4.10 give profiles and stability results for a current profile of the *TEXTOR type with shoulder* at $\rho \approx 0.4$. The marginal β_p has a rather high maximum (≈ 0.46) when the $q = 1$ surface is located slightly inside the shoulder, but $\beta_{p,crit}$ falls abruptly to between 0.1 and 0.2 when the $q = 1$ radius increases and reaches the low-shear region. The TEXTOR profile is particularly stable to the internal kink mode and can even be resistively stable at fairly high β_p [5,41,55].

The large aspect ratio results (Section 4.1) show that the $n = 1$ mode is unstable even at zero pressure when q_0 is below a threshold value ranging from 0.58 for the Shafranov profile to 0.40 for the parabolic-squared profile (see Figure 4.1(b)). This current driven mode is investigated for two finite aspect ratio equilibria with zero pressure: (a) the rounded profile and (b) the Shafranov profile, both surrounded by a region of currentless but conducting plasma. The aspect ratios (R_0/a for the rounded profile and R_0/r_0 , with $r_0 =$ the minor radius of the step for the Shafranov profile) are 4 in both cases. Figure 4.11 shows the resulting growth rates as functions of q_0 . Instability occurs below certain thresholds in q_0 , which are in remarkably good agreement with the large aspect ratio result in Figure 4.1(b). The instability at low q_0 has been observed previously by Turnbull and Troyon [56]. It is sensitive to the current profile, and the

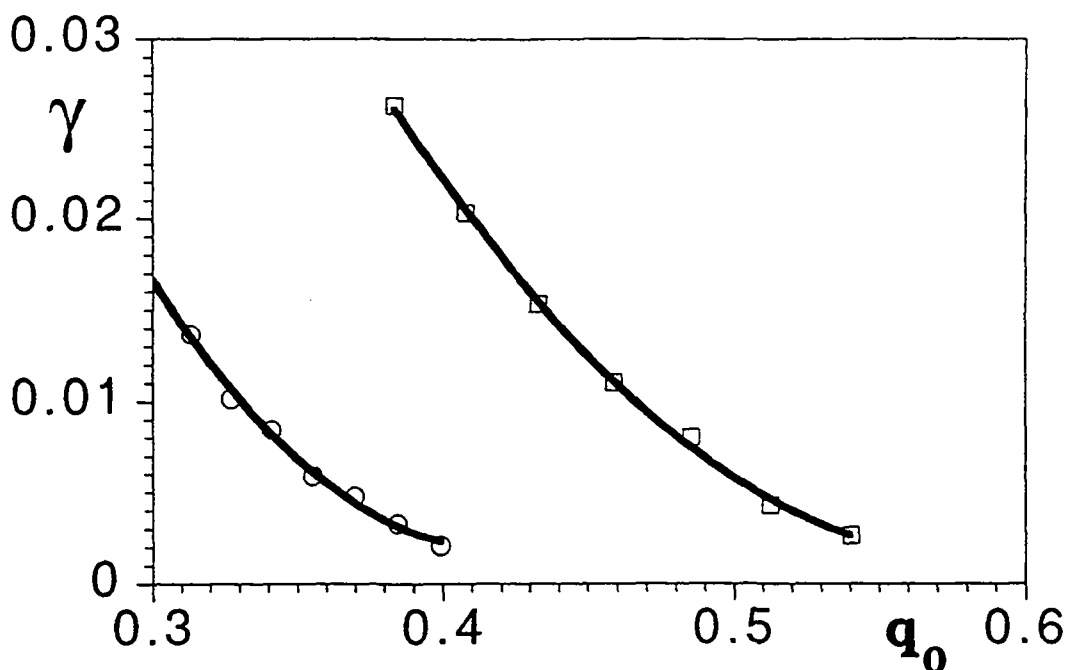


Figure 4.11: Internal kink instability at zero pressure for low q_0 , circular equilibrium ($A = 4$) with the rounded profile (circles) and the Shafranov profile (squares).

Shafranov profile is more unstable than the rounded profile.

The results for circular equilibria can be simply summarized. Except at very low aspect ratio, the stability of the internal kink is in good agreement with the large aspect ratio theory when the appropriate boundary conditions are applied. For smooth and monotonic current profiles, the marginal β_p decreases monotonically with increasing $q = 1$ radius and typical β_p -limits are between 0.1 and 0.2. The position of the wall is important only for tight aspect ratio and $q_a < 3$.

4.4 Shaping Effects - Numerical results for JET geometry

Certain previous investigations [57,16] have shown a destabilizing effect of ellipticity on the internal kink mode. This is clearly confirmed by the present study. To illustrate this, numerical results are given for the full ideal MHD stability problem in JET geometry: aspect ratio $A = 2.7$, elongation $\kappa = 1.7$, triangularity $\delta = 0.3$ and $\zeta = 0$ in

eq.(2.25) for the same current profiles as for the circular cross section. The $q(\rho)$ and $\hat{s}(\rho)$ profiles are slightly different from their circular equivalents, but the differences are insignificant in the central region, say $\rho < 0.6$.

The β_p -limits for JET geometry are significantly lower than for the circle. The results for the *rounded* current profile are shown in Figure 4.12. The maximum stable β_p is about 0.09 and the limit decreases as the $q = 1$ surface approaches the magnetic axis.

The effects of ellipticity were estimated analytically in Refs. [18,39] by computing the shaping contribution to δW_p at infinite aspect ratio and zero pressure. This shaping term was found to have a vanishing effect on the marginal β_p as $q_0 \rightarrow 1$. By contrast, the full MHD result in Figure 4.12 shows that the β_p -limit is strongly reduced for JET shape and small $q = 1$ radius. In fact, with JET shape, $\beta_{p,crit}$ vanishes, or is very small, as $q_0 \rightarrow 1$.

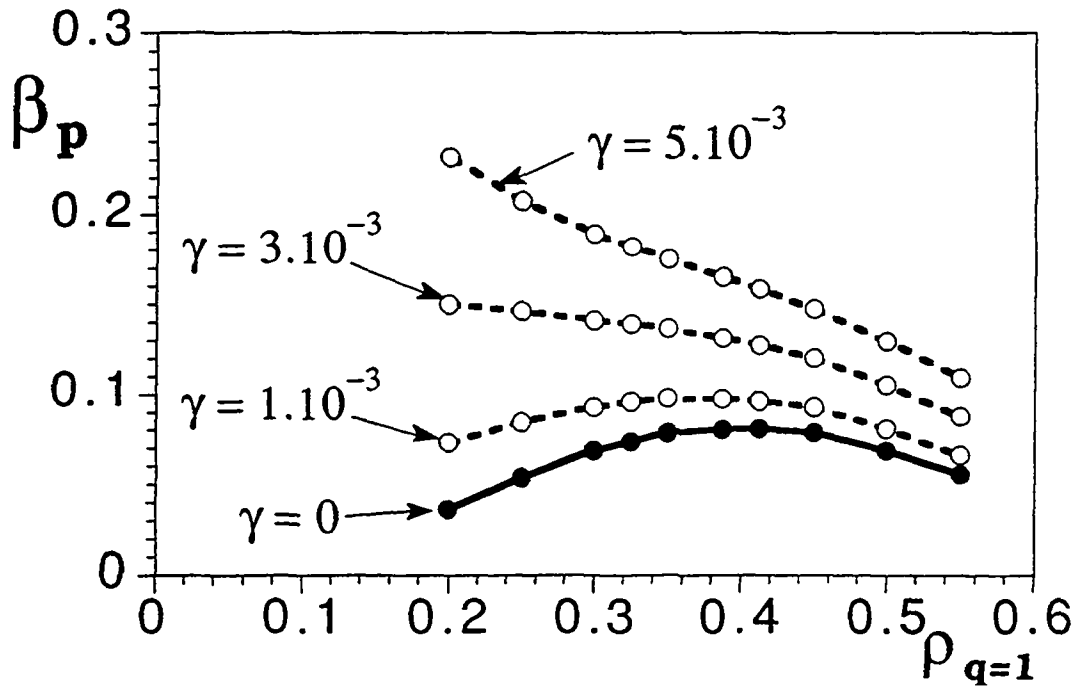


Figure 4.12: Stability limits in β_p for JET geometry and the *rounded* current profile (Figure 4.3).

Similarly, for the two *flattened* current profiles, the beta-limits are lower with the

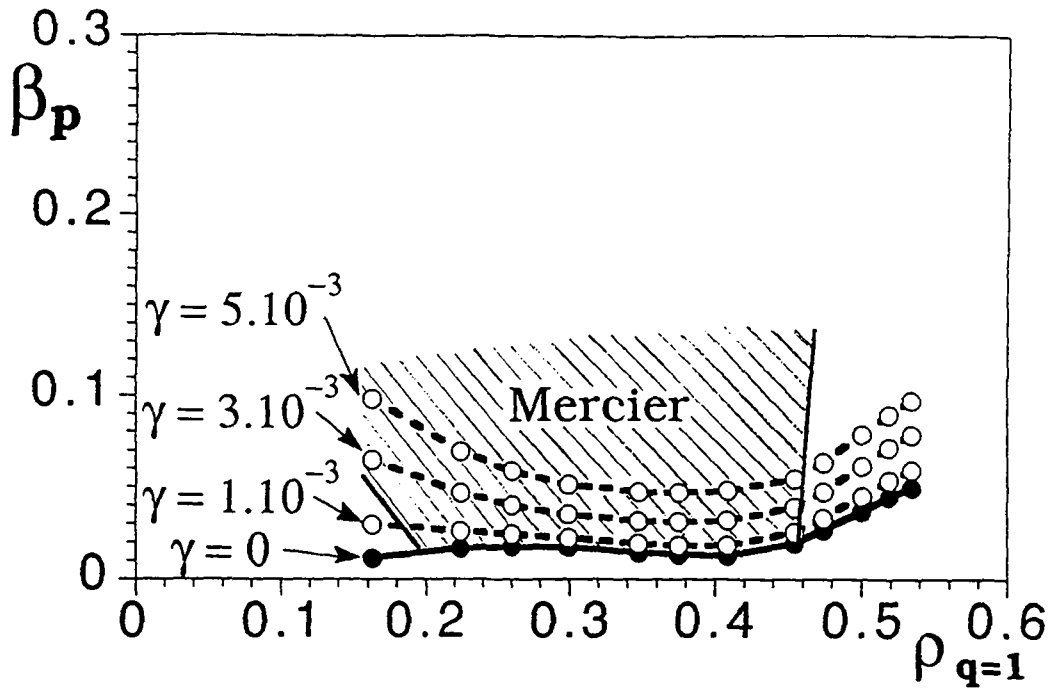


Figure 4.13: Stability limits in β_p for JET geometry and the *flattened* current profile with *low central shear* (Figure 4.6).

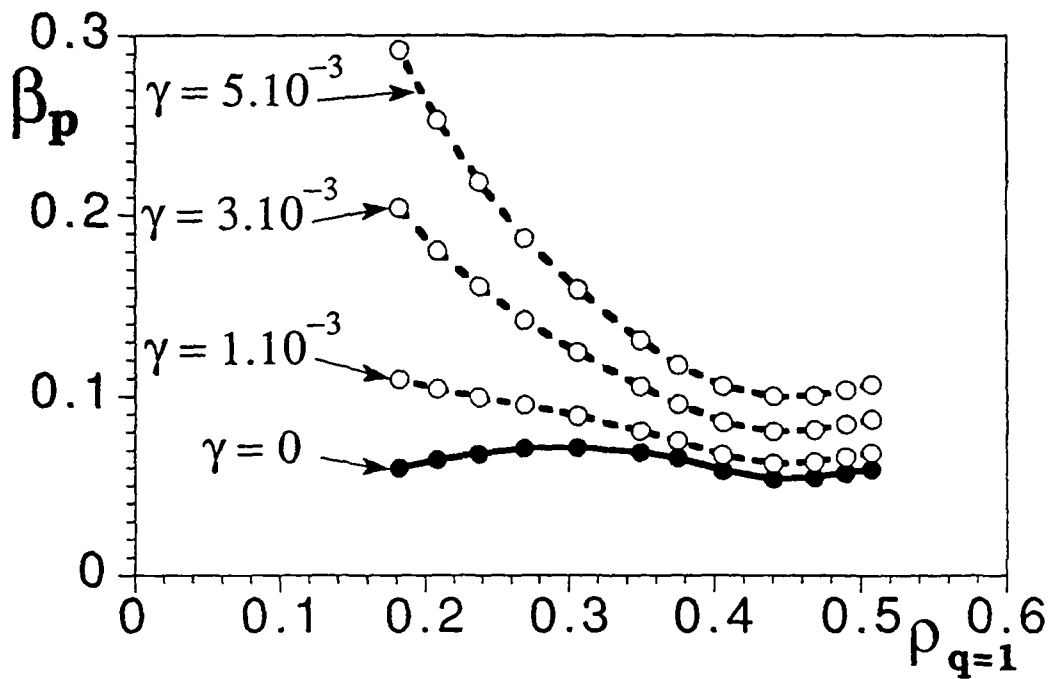


Figure 4.14: Stability limits in β_p for JET geometry and the *flattened* current profile with *medium central shear* (four times the central shear in Figure 4.6).

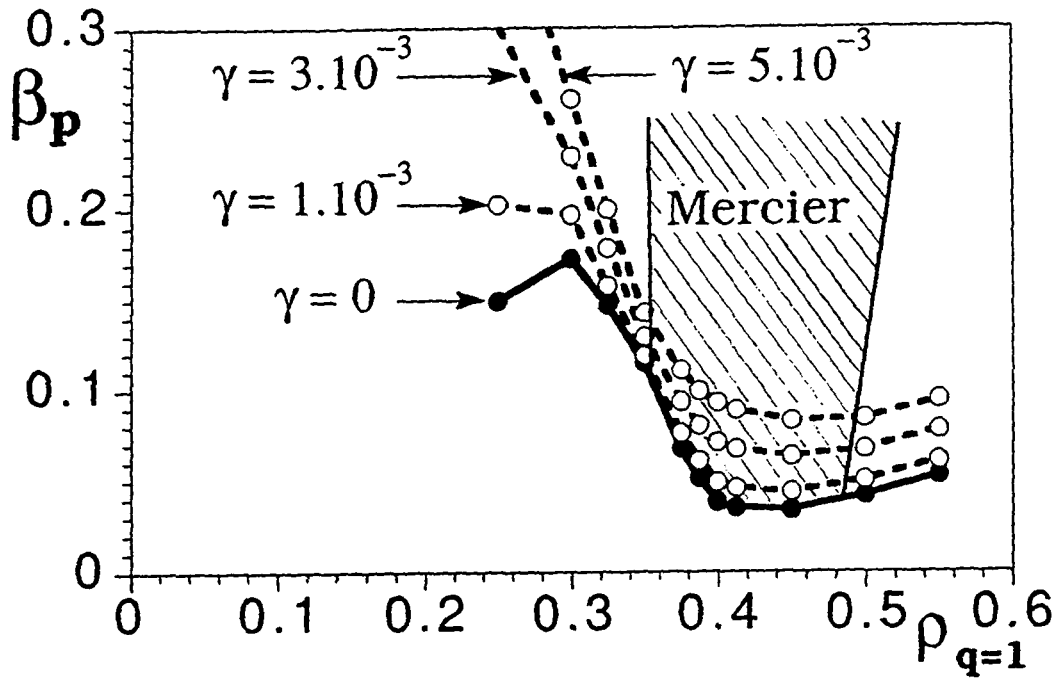


Figure 4.15: Stability limits in β_p for JET geometry and the *TEXTOR* current profile (Figure 4.9). The dashed region indicates violation of the Mercier criterion at $q = 1$.

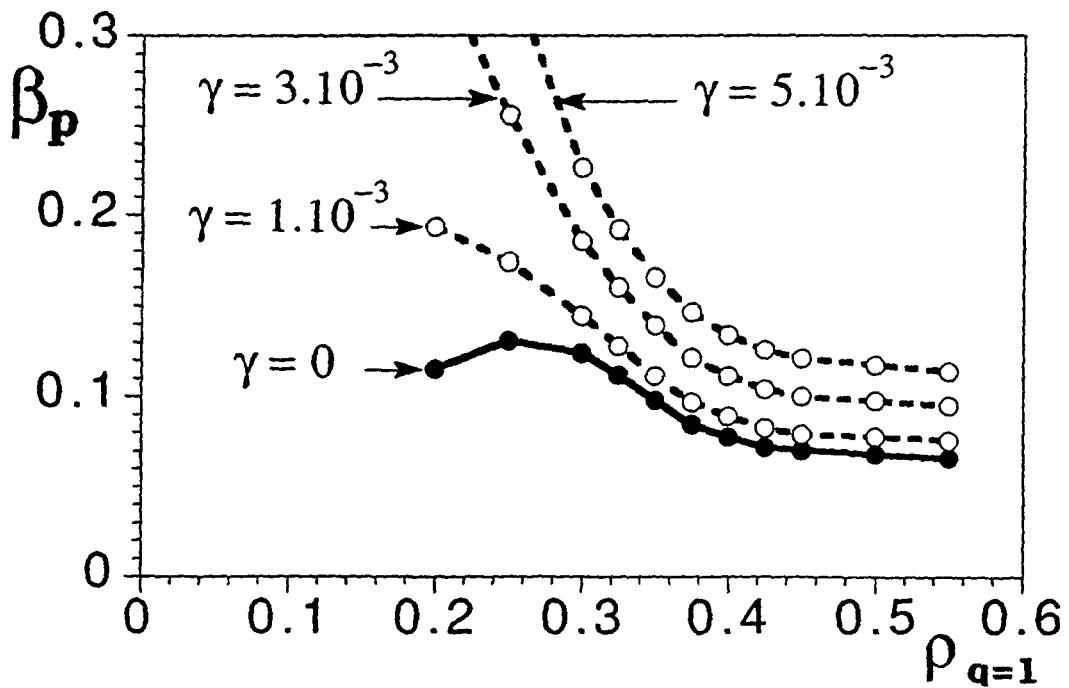


Figure 4.16: Stability limits in β_p for JET geometry and the *TEXTOR* current profile with reduced shoulders.

JET cross section than for a circle, see Figures 4.13 and 4.14. The decrease is rather dramatic for the profile with weak central shear, for which the β_p limit in JET geometry is typically around 0.03, while the medium shear profile gives about 0.08. Thus, contrary to the predictions of earlier analytical expansions [18,39], the destabilization is stronger in the case of weak central shear. This destabilization by shaping can be correlated with interchange instability. The shaded region of Figure 4.13 shows where the Mercier criterion (3.20) is violated on the $q = 1$ surface. The minimum in $\beta_{p,crit}$ is set by interchange instability for this equilibrium. It is well known [12,58] that, when the Mercier criterion is violated on a rational surface $q = m/n$, there exist (infinitely many) unstable modes with toroidal mode number n . Our numerical calculations show that violation of the Mercier criterion on the $q = 1$ surface leads to an $n = 1$ internal mode, typically with a large growth rate.

Further evidence of the importance of interchange stability can be found in the stability diagram for the *TEXTOR* current profile, Figure 4.15. This Figure shows a clear dependence on the shear locally at the $q = 1$ surface. The β_p -limit drops from about 0.17 (the highest value we have found with JET geometry), when the $q = 1$ surface is in the high-shear region inside the shoulder, to about 0.03 when it enters the region of minimum shear. The minimum in $\beta_{p,crit}$ again coincides with the threshold for interchange at the $q = 1$ surface, and increases if the minimum shear is increased. Figure 4.16 shows the stability diagram for a *TEXTOR* profile with reduced shoulder and larger minimum shear [$\hat{s}_{min} = \hat{s}(\rho \approx 0.38) \approx 0.16$]. Note the absence of a local minimum in the marginal β_p at the radius of minimum shear for this equilibrium.

It is of interest to consider the shape of the unstable eigenfunction when the Mercier criterion is violated at the $q = 1$ surfaces. This reveals that, when the Mercier criterion is violated only in a small region around the $q = 1$ surface, the mode structure is quite different from the usual step function. As an example, Figure 4.17(a) shows the unstable displacement for the JET cross section and the *TEXTOR* current profile, with the $q = 1$ surface at the point of minimum shear, at two different pressures. In the

lowest-beta case, the Mercier criterion is violated only in a small region around $q = 1$, and the unstable mode has a clear interchange character. However, for a relatively moderate β_p , the mode resembles the standard step-function of the internal kink. In cases where the Mercier criterion is violated more globally in the $q < 1$ region, the unstable mode stays close to the step function also near the marginal point, as shown in Figure 4.17(b) for the low-shear profile.

The numerical results of this Section show that the ideal MHD pressure limit for the internal kink is significantly lower in JET geometry than for a circle. For most of the JET cases examined here, the critical β_p is below 0.1. With elliptic shaping and weak shear, the Mercier criterion can be violated at low β_p , and this generally gives rise to global instabilities with large growth rates.

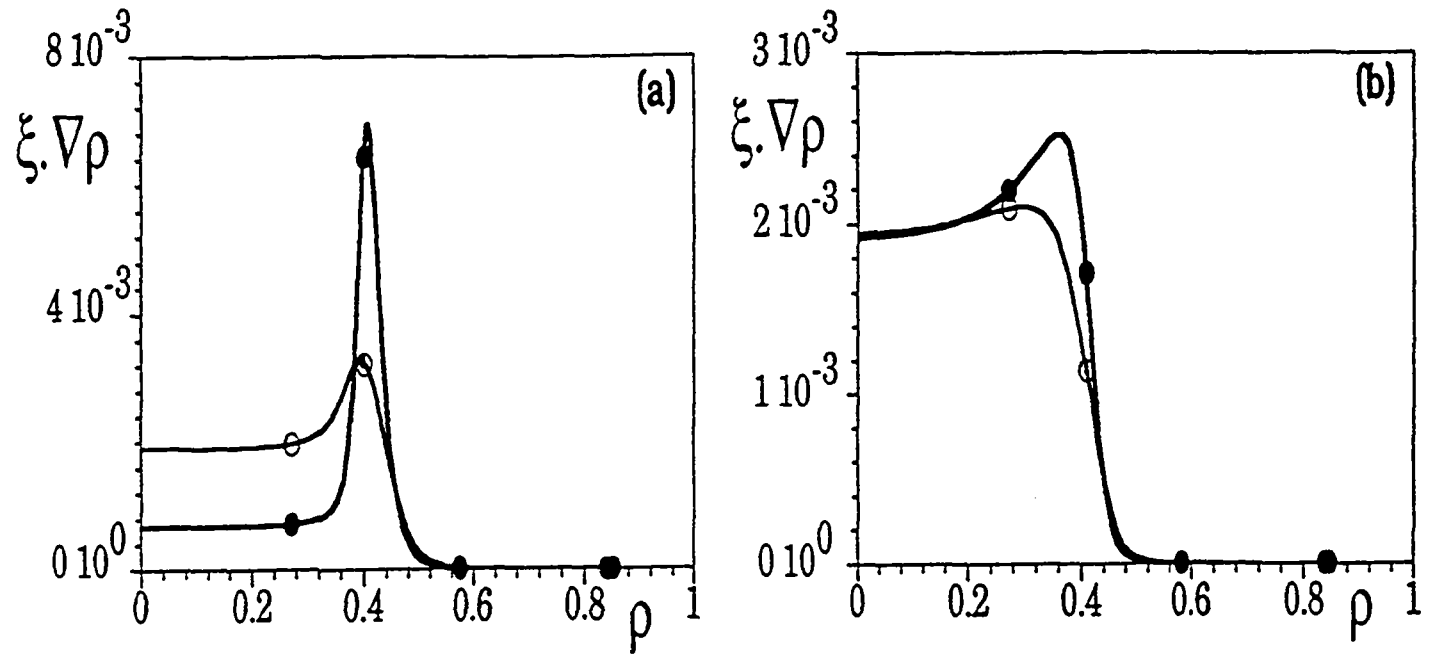


Figure 4.17: Eigenfunctions ($m = 1$ components of $\xi \cdot \nabla \rho$ in straight field line coordinates) for different cases with JET cross section when the Mercier criterion is violated at the $q = 1$ surface.

(a) The TEXTOR current profile (Figures 4.9 and 4.15) with $\rho_{q=1} = 0.4$ and the Mercier criterion is violated only locally around $q = 1$. The two cases have $\beta_p = 0.043$, $\gamma = 9.9 \cdot 10^{-4}$ (filled symbols) and $\beta_p = 0.096$, $\gamma = 4.2 \cdot 10^{-3}$ (open symbols) respectively.

(b) The low-shear current profile (Figures 4.6 and 4.13) with $\rho_{q=1} \approx 0.41$. The Mercier criterion is violated globally for $q < 1$. The two cases have $\beta_p = 0.025$, $\gamma = 2.0 \cdot 10^{-3}$ (filled symbols) and $\beta_p = 0.042$, $\gamma = 4.1 \cdot 10^{-3}$ (open symbols) respectively.



Chapter 5

Large aspect ratio Mercier and resistive interchange criteria including shape effects

In this Chapter, a large aspect ratio expansion is applied to derive a form of the Mercier [13] and the resistive interchange [12] criteria retaining the effects of ellipticity and triangularity.

Comparison of the numerical results in the preceding Chapter for circular and JET shaped cross sections shows that ellipticity is destabilizing. The destabilization is particularly noticeable at low shear, contrary to the large aspect ratio predictions of [18,39]. However, the shape corrections in [18,39] were evaluated at infinite aspect ratio and zero pressure, while the destabilization of the internal kink in our numerical examples with low shear is connected with violation of the Mercier criterion on $q = 1$. This instability is well known: for vertically elongated flux surfaces, the Mercier criterion on the magnetic axis (see [10], Chapter 10 or [59,60]) is violated when $q = 1$ (unless the triangularity is sufficiently large). It is evident that terms which are normally “small” in the large aspect ratio expansion can become non-negligible for equilibria with weak shear.

It would be desirable to express the ellipticity corrections to the potential energy of the internal kink by extending the large aspect ratio of Bussac et al. [11]. This entails retaining the toroidicity and ellipticity induced couplings of the $m = 1$ component to its

four side-bands, $m = -1, 0, 2, 3$, and calculating all $\mathcal{O}(\varepsilon^2 e)$ terms (where $\varepsilon = \rho_{q=1} a / R_0$ and e is the ellipticity) in $\delta W_p / \varepsilon^2$. This is a rather formidable calculation, and, to illustrate the point, we shall content ourselves by giving the corrections to the Mercier and the resistive interchange criteria due to ellipticity and triangularity at large aspect ratio.

The standard large aspect expansion is modified by introducing two small parameters: toroidicity, $\varepsilon [= r/R_0]$, and ellipticity, $e [= (\kappa - 1)/2]$. The asymptotic large aspect ratio ordering in ε assumed here is $q \approx r B_0 / (R B_p) \sim \mathcal{O}(1)$ and $2p/B_0^2 \sim \mathcal{O}(\varepsilon^2)$, where B_p is the poloidal magnetic field. In that limit, the magnetic field (2.1) can be approximated so that

$$\begin{aligned} G &= R_0 B_0 \hat{g}(r) \\ \nabla \Psi &= R_0 B_0 \varepsilon f(r) \nabla r \end{aligned} \tag{5.1}$$

and therefore, using the Grad-Shafranov equation (2.3) and Ampere's law in eq.(1.2), $\hat{g}(r) = 1 + \mathcal{O}(\varepsilon^2)$. The expansion of the Mercier and the resistive interchange criteria is taken to second order in ε and to first order in e , keeping the contributions of order $\varepsilon^2 e$. This is justified because the normally leading $\mathcal{O}(\varepsilon^2)$ pressure contribution to the Mercier parameter vanishes for $q = 1$, so that the $\mathcal{O}(\varepsilon^2 e)$ shaping terms give the leading contribution. We stress the importance of ordering ellipticity independently from aspect ratio. Connor and Hastie [18] set $e = \mathcal{O}(\varepsilon)$ which makes the ellipticity-induced terms higher order in ε (and, in the limit of infinite aspect ratio, the equilibrium is circular). The modified ordering allows us to calculate the contribution due to elliptic and triangular shaping without going beyond second order in ε . Except for the difference in ordering, our calculation follows that of Connor and Hastie [18]. The flux

surfaces are assumed to have the shape

$$\begin{aligned}
R &= R_0 - \varepsilon(r - eE(r)) \cos \omega - \varepsilon^2 \Delta(r) + \varepsilon^2 T(r) \cos 2\omega + \\
&\quad \varepsilon^3 \sum_n P_n(r) \cos n\omega + \dots \\
Z &= \varepsilon(r + eE(r)) \sin \omega + \varepsilon^2 T(r) \sin 2\omega - \\
&\quad \varepsilon^3 \sum_n Q_n(r) \sin n\omega + \dots
\end{aligned} \tag{5.2}$$

where r and ω are two non-orthogonal coordinates corresponding to minor radius and poloidal angle, and ε and e are the independent expansion parameters. The elliptic deformation $E(r)$ is related to the elongation by $\kappa = 1 + 2E/r + \mathcal{O}((E/r)^2)$ and to the ellipticity by $E = re$, $\Delta(r)$ is the Shafranov shift, and $T(r)$ is the triangular deformation related to the triangularity by $\delta = 4T(r)/r$. Eq.(5.2) contains all shaping terms of order ε^3 , contrary to the expansion used in [54,55], and here, it will be shown explicitly that no term of this order contributes to the Mercier parameter (3.20)

$$-D_I = \left(\frac{p' G J_2}{q'} - \frac{1}{2} \right)^2 + \frac{p'}{q'^2} (J_5' - p' J_3) (G^2 J_1 + J_4) \tag{5.3}$$

and to the resistive interchange parameter (3.21)

$$-D_R = -D_I - (H - 1/2)^2 \tag{5.4}$$

where

$$H = \frac{G p'}{q'} \left(J_2 - \frac{J_5 (J_4 + G^2 J_1)}{J_6 + G^2 J_4} \right) \tag{5.5}$$

and

$$\begin{aligned}
\{J_1, J_2, J_3, J_4, J_5, J_6\} &= \\
\frac{1}{2\pi} \oint_{\Psi=\text{const}} \left\{ \frac{1}{R^2 |\nabla \Psi|^2}, \frac{1}{|\nabla \Psi|^2}, \frac{R^2}{|\nabla \Psi|^2}, \frac{1}{R^2}, 1, \frac{|\nabla \Psi|^2}{R^2} \right\} J d\chi.
\end{aligned} \tag{5.6}$$

In the following, we use the straight field-line coordinates (\hat{r}, χ, Φ) defined by

$$\begin{aligned}
\hat{r}^2 &= \frac{R_0}{\pi} \int_0^r dr' \oint_{r'=\text{const}} \frac{\tilde{J}}{R^2} d\omega \\
\chi &= 2\pi \frac{\int_{0, r=\text{const}}^{\omega} \frac{\tilde{J}}{R^2} d\omega'}{\oint_{r=\text{const}} \frac{\tilde{J}}{R^2} d\omega'}
\end{aligned} \tag{5.7}$$

rather than (r, ω, Φ) , where

$$\tilde{J} = R \left(\frac{\partial R}{\partial \omega} \frac{\partial Z}{\partial r} - \frac{\partial R}{\partial r} \frac{\partial Z}{\partial \omega} \right). \quad (5.8)$$

Introducing eq.(5.2) and eq.(5.8) into (5.7) permits to identify \hat{r} with r at order $\mathcal{O}(\varepsilon^3) + \mathcal{O}(e^2)$ by choosing the geometric coefficients P_1 and Q_1 so that

$$P_1 \left(1 + \frac{eE}{r} \right) + Q_1 \left(1 - \frac{eE}{r} \right) = \frac{r^3}{4R_0^2} + \frac{r\Delta}{R_0} - \frac{er^2E}{2R_0^2} - \frac{eET}{R_0}. \quad (5.9)$$

The Jacobian from $(\hat{r}, \chi, \Phi) = (r, \chi, \Phi)$ space to Cartesian coordinates reads

$$J = \tilde{J} \frac{d\omega}{d\chi} = \frac{qR^2}{G} \quad (5.10)$$

and the safety factor is given by

$$q(r) = \frac{G(r)}{R_0 B_0 f(r)} \frac{r}{R_0} + \mathcal{O}(\varepsilon^3) + \mathcal{O}(e^2). \quad (5.11)$$

Therefore, the integrals (5.6) read

$$\{J_1, J_2, J_3, J_4, J_5, J_6\} = \frac{1}{2\pi} \oint_{\Psi=\text{const}} \left\{ \frac{1}{(R_0 B_0 \varepsilon f |\nabla r|)^2}, \frac{R^2}{(R_0 B_0 \varepsilon f |\nabla r|)^2}, \frac{R^4}{(R_0 B_0 \varepsilon f |\nabla r|)^2}, 1, R^2, (R_0 B_0 \varepsilon f |\nabla r|)^2 \right\} \frac{q}{G} d\chi \quad (5.12)$$

in (r, χ, Φ) coordinates. The integrals (5.12) involve the quantities R and $(g^{rr})^{-1} = |\nabla r|^{-2}$, which must be expressed in (r, χ, Φ) coordinates. For an expansion of R , given by eq.(5.2), as a function of r and χ with an error of order $\mathcal{O}(\varepsilon^3) + \mathcal{O}(e^2)$, ω is needed with an error of order $\mathcal{O}(\varepsilon^2) + \mathcal{O}(e^2)$. At lowest order in ε ,

$$(g^{rr})^{-1} = \frac{\tilde{J}^2}{R^2 g_{\omega\omega}} = \{1 - 2eE' \cos 2\omega\} \varepsilon^2 + \mathcal{O}(\varepsilon^3) + \mathcal{O}(e^2) \quad (5.13)$$

where

$$g_{\omega\omega} = \left(\frac{\partial R}{\partial \omega} \right)^2 + \left(\frac{\partial Z}{\partial \omega} \right)^2. \quad (5.14)$$

Therefore, for an expansion of $(g^{rr})^{-1}$ as a function of r and χ with an error of order $\mathcal{O}(\varepsilon^5) + \mathcal{O}(e^2)$, ω is required with an error of order $\mathcal{O}(\varepsilon^3)$ in the $\varepsilon\varepsilon^2$ term of eq.(5.13),

and with an error of order $\mathcal{O}(\varepsilon^2) + \mathcal{O}(e^2)$ in the higher order terms in ε . With eq.(5.7), χ can be expressed in terms of r and ω :

$$\begin{aligned} \chi \equiv & \omega + e\chi_e(r, \omega) + \varepsilon\chi_\varepsilon(r, \omega) + \varepsilon e\chi_{ee}(r, \omega) + \varepsilon\chi_{eT}(r, \omega) + \\ & \varepsilon e\chi_{eeT}(r, \omega) + \varepsilon^2\chi_{e^2}(r, \omega) + \varepsilon^2\chi_{e^2T}(r, \omega) + \dots \end{aligned} \quad (5.15)$$

where

$$\begin{aligned} \chi_e(r, \omega) &= \frac{1}{2} \left(\frac{E}{r} - E' \right) \sin 2\omega \\ \chi_\varepsilon(r, \omega) &= \left(\frac{r}{R_0} + \Delta' \right) \sin \omega \\ \chi_{ee}(r, \omega) &= \left(\frac{E\Delta'}{r} - \frac{(rE)'}{2R_0} \right) \sin \omega + \frac{E - rE'}{6R_0} \sin 3\omega \\ \chi_{eT}(r, \omega) &= \frac{1}{3} \left(\frac{2T}{r} - T' \right) \sin 3\omega \\ \chi_{eeT}(r, \omega) &= - \left(\frac{ET' + 2E'T}{r} \right) \sin \omega \\ \chi_{e^2}(r, \omega) &= \omega \left(\frac{r^2}{2R_0^2} + \frac{\Delta}{R_0} + \frac{r\Delta'}{2R_0} \right) + \left(\frac{r^2}{4R_0^2} + \frac{r\Delta'}{4R_0} \right) \sin 2\omega - \sum_n \\ & \quad \left\{ \left(\frac{n(P_n + Q_n)}{r} + P'_n + Q'_n \right) \frac{\sin(n-1)\omega}{2(n-1)} - \right. \\ & \quad \left. \left(\frac{n(P_n - Q_n)}{r} - P'_n + Q'_n \right) \frac{\sin(n+1)\omega}{2(n+1)} \right\} \\ \chi_{e^2T}(r, \omega) &= \left(\frac{T\Delta'}{r} - \frac{rT'}{4R_0} \right) \sin 2\omega + \left(T - \frac{rT'}{2} \right) \frac{\sin 4\omega}{4R_0} \end{aligned} \quad (5.16)$$

The prime denotes the derivative with respect to r . The two expansions of ω as a function of r and χ needed for the evaluation of R and $(g^{rr})^{-1}$ in (r, χ, Φ) coordinates are obtained by successive approximations from eqs.(5.15,5.16):

- order $e\varepsilon$:

$$\begin{aligned} \omega &= \chi - e\chi_e \left\{ r, \chi - \varepsilon\chi_\varepsilon(r, \chi) - \varepsilon\chi_{eT}(r, \chi) \right\} - \\ & \quad \varepsilon\chi_\varepsilon \left\{ r, \chi - e\chi_e(r, \chi) \right\} - \varepsilon e\chi_{ee} \{ r, \chi \} - \\ & \quad \varepsilon\chi_{eT} \left\{ r, \chi - e\chi_e(r, \chi) \right\} - \varepsilon e\chi_{eeT} \{ r, \chi \} + \mathcal{O}(\varepsilon^2) + \mathcal{O}(e^2) \end{aligned} \quad (5.17)$$

• order ε^2 :

$$\begin{aligned}
\omega &= \chi - \varepsilon \chi_\varepsilon \left\{ r, \chi - \varepsilon \chi_\varepsilon(r, \chi) - \varepsilon \chi_{\varepsilon T}(r, \chi) \right\} - \\
&\quad \varepsilon \chi_{\varepsilon T} \left\{ r, \chi - \varepsilon \chi_\varepsilon(r, \chi) \right\} - \varepsilon^2 \chi_{\varepsilon^2} \{ r, \chi \} - \\
&\quad \varepsilon^2 \chi_{\varepsilon^2 T} \{ r, \chi \} + \mathcal{O}(\varepsilon^3) + \mathcal{O}(e).
\end{aligned} \tag{5.18}$$

Now, the integrals (5.12) can be evaluated. To the required order,

$$\begin{aligned}
J_1 &= \frac{R_0^2 q^3}{r^2 G^3} \left[1 + \hat{c}_0 - 3\hat{c}_2 - \varepsilon^2 \left(\frac{r^2}{R_0^2} + \frac{2\Delta}{R_0} \right) + e\varepsilon^2 E \frac{3r}{2R_0^2} \right] \\
J_2 &= \frac{R_0^4 q^3}{r^2 G^3} \left[1 + \hat{c}_0 + 3\hat{c}_1 + 3\hat{c}_2 - \varepsilon^2 \left(\frac{3r^2}{2R_0^2} + \frac{4\Delta + 3r\Delta'}{R_0} \right) + e\varepsilon^2 \frac{9rE + 3r^2 E'}{4R_0^2} \right] \\
J_3 &= \frac{R_0^6 q^3}{r^2 G^3} \left[1 + \hat{c}_0 + 6\hat{c}_1 + 9\hat{c}_2 - \varepsilon^2 \frac{6(r\Delta)'}{R_0} - e\varepsilon^2 \frac{3r^2 E'}{2R_0^2} \right] \\
J_4 &= \frac{q}{G} \\
J_5 &= \frac{R_0^2 q}{G} \left[1 + \hat{c}_1 - \varepsilon^2 \left(\frac{r^2}{2R_0^2} + \frac{2\Delta}{R_0} + \frac{r\Delta'}{R_0} \right) + e\varepsilon^2 \frac{3rE + r^2 E'}{4R_0^2} \right] \\
J_6 &= \frac{r^2 G}{R_0^2 q} \left[1 - \hat{c}_0 - \hat{c}_2 + \varepsilon^2 \left(\frac{r^2}{R_0^2} + \frac{2\Delta}{R_0} \right) - e\varepsilon^2 E \frac{3r}{2R_0^2} - \right. \\
&\quad \left. \frac{2\Delta'}{r} e\varepsilon^2 \left(\frac{2ET}{r} + 6E'T + ET' \right) + (\Delta')^2 \varepsilon^2 \left(2 + \frac{3eE}{r} \right) + \right. \\
&\quad \left. 2eE'\varepsilon^2 (P'_1 - Q'_1 + P'_3 + Q'_3) \right]
\end{aligned} \tag{5.19}$$

where

$$\begin{aligned}
\hat{c}_0 &= \varepsilon^2 \left\{ \frac{r^2}{R_0^2} + \frac{2\Delta}{R_0} + \frac{r\Delta'}{R_0} - e \frac{(r^3 E)'}{2rR_0^2} - e \frac{(rET)'}{rR_0} - \right. \\
&\quad \left. 3e\Delta' \left(\frac{T}{r} \left[\frac{E}{r} + 3E' \right] + \frac{T'}{2} \left[\frac{E}{r} - E' \right] \right) + \right. \\
&\quad \left. \frac{3}{2} (\Delta')^2 \left(1 + \frac{3eE}{2r} - \frac{1}{2} eE' \right) - \frac{e}{r} (P_1 - Q_1) \left(\frac{E}{2r} + E' \right) - \right. \\
&\quad \left. P_1' \left(1 + \frac{eE}{r} - \frac{3}{2} eE' \right) - Q_1' \left(1 - \frac{eE}{r} + \frac{3}{2} eE' \right) - \right. \\
&\quad \left. \frac{3eE}{2r^2} (P_3 + Q_3) + \frac{3}{2} eE' (P_3' + Q_3') \right\} \\
\hat{c}_1 &= e\varepsilon^2 \frac{(rET)'}{rR_0} \\
\hat{c}_2 &= e\varepsilon^2 E' \frac{r(\Delta' - T')}{2R_0}
\end{aligned} \tag{5.20}$$

The only non-vanishing contributions of the $\mathcal{O}(\varepsilon^3)$ shaping corrections in eq.(5.2) are the w and the $3w$ harmonics. They appear in J_1 , J_2 , J_3 and J_6 and cancel out when the Mercier and the resistive interchange criteria are evaluated.

The Mercier parameter $-D_I$ in (5.3,5.4) involves J_5' , and therefore, Δ'' , E'' and T'' . These quantities are obtained from the Grad-Shafranov equation, which, in (r, ω, Φ) coordinates, reads

$$\frac{f}{\bar{J}} \left[\frac{\partial}{\partial r} \left(\frac{f g_{\omega\omega}}{\bar{J}} \right) - \frac{\partial}{\partial \omega} \left(\frac{f g_{r\omega}}{\bar{J}} \right) \right] + \frac{p'}{R_0^2 B_0^2} + \frac{\hat{g}\hat{g}'}{R^2} = 0 \tag{5.21}$$

expanded in ε and e , with $' = \varepsilon^{-1} d/dr$. The ω independent piece gives the cylindrical pressure balance equation

$$\hat{g}' + \frac{p'}{B_0^2} + \frac{f}{r} (rf)' = 0 \tag{5.22}$$

that allows us to eliminate \hat{g}' . Equations for the Shafranov shift and the elliptic and the triangular deformations of the flux surfaces are obtained from the $\cos\omega$ component

at $\mathcal{O}(\varepsilon)$, the $\cos 2\omega$ component at $\mathcal{O}(e)$ and the $\cos 3\omega$ component at $\mathcal{O}(\varepsilon)$ respectively:

$$\begin{aligned}
\Delta'' &= -\left(\frac{2f'}{f} + \frac{1}{r}\right)\Delta' + \frac{1}{R_0} - \frac{2rp'}{R_0 B_0^2 f^2} + \\
&e \left[E \left(\frac{3p'}{R_0 B_0^2 f^2} - \frac{3\Delta'}{r^2} + \frac{12T}{r^3} + \frac{5T'}{r^2} + \frac{2Tf'}{r^2 f} \right) + \right. \\
&E' \left(\frac{3rp'}{R_0 B_0^2 f^2} + \frac{3\Delta' f'}{f} + \frac{10T}{r^2} + \frac{2T'}{r} - \frac{3T' f'}{f} - \frac{1}{R_0} \right) \left. \right] \\
E'' &= -\left(\frac{2f'}{f} + \frac{1}{r}\right)E' + \frac{3}{r^2}E \\
T'' &= -\left(\frac{2f'}{f} + \frac{1}{r}\right)T' + \frac{8}{r^2}T + \\
&e \left[E \left(\frac{p'}{R_0 B_0^2 f^2} + \frac{3\Delta'}{r^2} \right) - E' \left(\frac{3rp'}{R_0 B_0^2 f^2} + \frac{4\Delta'}{r} + \frac{3\Delta' f'}{f} - \frac{1}{R_0} \right) \right]
\end{aligned} \tag{5.23}$$

Replacing Δ'' , E'' and T'' into J'_5 leads to the Mercier and the resistive interchange criteria, to second order in ε and first order in e :

$$\begin{aligned}
-D_I &= \frac{1}{4} + \frac{2p'}{rB_0^2} \frac{q^2}{(q')^2} \left[1 - q^2 + \frac{3q^2}{4} \left(\frac{E}{r} + E' \right) + \frac{3q^2}{2} \Lambda \left(\frac{E}{r} - E' \right) - \right. \\
&\left. \frac{R_0 q^2}{r} \left(\frac{2ET}{r^2} + \frac{6E'T}{r} + \frac{7ET'}{2r} - \frac{3}{2} E'T' \right) \right] > 0 \\
-D_R &= \frac{2p'}{rB_0^2} \frac{q^2}{(q')^2} \left\{ \left[1 - q^2 + \frac{3q^2}{4} \left(\frac{E}{r} + E' \right) + \frac{3q^2}{2} \Lambda \left(\frac{E}{r} - E' \right) - \right. \right. \\
&\left. \frac{R_0 q^2}{r} \left(\frac{2ET}{r^2} + \frac{6E'T}{r} + \frac{7ET'}{2r} - \frac{3}{2} E'T' \right) \right] + \\
&rqq' \left[-\Lambda + \left(\frac{3\Lambda}{2} + \frac{1}{4} \right) E' + \right. \\
&\left. \frac{R_0}{r} \left(\frac{ET}{r^2} + \frac{E'T}{r} + \frac{ET'}{r} - \frac{3}{2} E'T' \right) \right] \left. \right\}.
\end{aligned} \tag{5.24}$$

In eq.(5.24), $\Lambda = R_0 \Delta' / r \approx \beta_p(r) + \ell_i(r)/2$, where ℓ_i is the internal inductance. Eq.(5.24) generalizes the formula for circular flux surfaces of Shafranov and Yurchenko [61] and Glasser, Greene and Johnson [12], and is consistent with previous expressions retaining shaping effects near the magnetic axis [59]. Figure 5.1 shows that (5.24) is in reasonable agreement with the full Mercier criterion for two equilibria with (a) large aspect ratio $A = 10$, $\kappa = 1.3$ and (b) small aspect ratio $A = 2.7$, $\kappa = 1.7$. Figure 5.1

also shows the standard Shafranov-Yurchenko expression, which ignores the effect of ellipticity and fails to predict interchange instability at $q = 1$.

An approximation of (5.24) that is often useful for the internal kink mode is obtained by considering almost flat current profiles with q' small and E/r and T/r^2 constant. Together with $q = 1$, this gives

$$\begin{aligned} -D_I &\approx \frac{1}{4} + \frac{rp'}{\hat{s}^2 B_0^2} \frac{3E}{r} \left(1 - \frac{8T}{r} \frac{R_0}{r}\right) \\ -D_R &\approx \frac{rp'}{\hat{s}^2 B_0^2} \left[\frac{3E}{r} \left(1 - \frac{8T}{r} \frac{R_0}{r}\right) - 2\hat{s}\Lambda \right]. \end{aligned} \tag{5.25}$$

Eq.(5.25) shows that for sufficiently ellipticity, ideal interchange instability can occur for modest pressure and not-so-low shear. As an example, we assume that the pressure profile is parabolic, giving $\beta_p = -(p'/(rB_0^2))(R_0^2 q^2/2)$, and that triangularity is negligible. The Mercier criterion (5.25) then reduces to $\beta_p < \hat{s}^2/(24e\epsilon^2)$. Even though the expansion to first order in ellipticity is not very accurate for JET geometry, we consider a JET-like case with $\epsilon_{q=1} = 0.16$ and $e_{q=1} = 0.2$ for which (5.25) gives $\beta_p < 8\hat{s}^2$. This criterion is violated for rather modest pressures when the shear is less than about 0.1. For low shear, say $\hat{s} \leq 0.03$, even a minute pressure gradient will violate the Mercier criterion at $q = 1$ in an elongated tokamak.

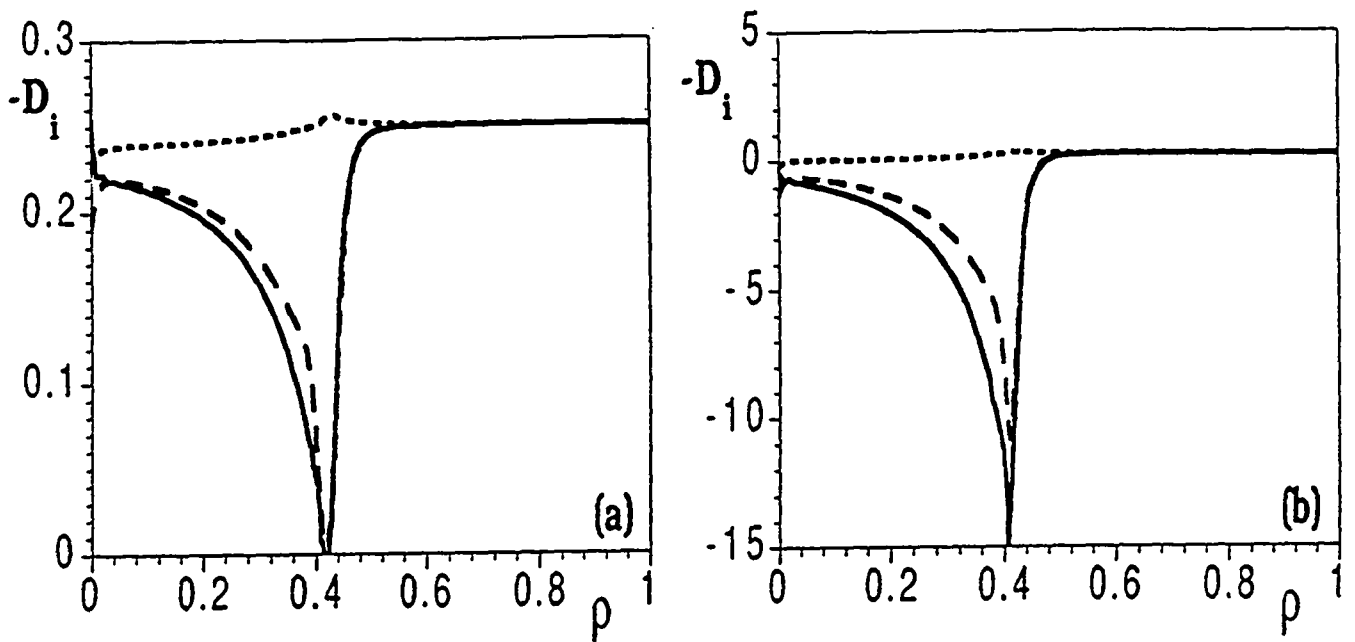


Figure 5.1: The Mercier criterion for an equilibrium with elliptic cross-section and low shear around the $q = 1$ surface. The solid line gives the full criterion (5.3), the curve with long dashes the large aspect ratio expansion with ellipticity (5.24), and the curve with short dashes gives the Shafranov-Yurchenko approximation.

(a) aspect ratio $A = 10$, elongation $\kappa = 1.3$.

(b) aspect ratio $A = 2.7$, elongation $\kappa = 1.7$.

Chapter 6

Resistive toroidal stability of internal kink modes in circular and shaped tokamaks

The dynamics of resistive MHD instabilities is concentrated on thin layers around the resonant surfaces. It is therefore possible to neglect effects of resistivity everywhere in the plasma except in thin layers around the resonant surfaces. The complete solution is then obtained by matching asymptotically the solutions in the resistive layer to the solutions in the ideal regions on either side of it. A dispersion relation of the form

$$\Delta'(\gamma) = \frac{B_+ - B_-}{A_l} \quad (6.1)$$

arises from the matching condition. A_l is the coefficient of the large solution, and B_- , B_+ are the coefficients of the small solution to the left and the right of the resistive layer.

In pressure-less plasma with a circular boundary and in the limit of infinite aspect ratio, the ideal kink mode is marginally stable and the resistive mode is strongly unstable (= the resistive kink mode). The dispersion relation was obtained by Coppi et al. [14]. Toroidicity is stabilizing, and at finite aspect ratio, the resistive kink with $\Delta' = \infty$ turns into a tearing mode with Δ' finite, if $\beta_p < \beta_{p,\text{marginal}}$ for the ideal mode [15]. The growth rate of the resistive tearing mode is of order $\tau_A^{-2/5} \tau_r^{-3/5}$, whereas the resistive kink mode scales as $\tau_A^{-2/3} \tau_r^{-1/3}$, i.e. intermediate between resistive tearing and ideal mode, whose growth rate is of order τ_A^{-1} . Here, $\tau_r = \mu_0 a^2 / \eta$ denotes the

resistive time connected with the minor radius and $\tau_A = R_0/v_A$ is the toroidal Alfvén time. Numerical studies for plasmas with circular cross sections have shown that even the resistive tearing mode can be stabilized, $\Delta' < 0$, if the shear at the $q = 1$ is reduced [5,41].

A main factor for the stability of the internal kink is the pressure. The global effects of pressure are described primarily by the poloidal beta at the $q = 1$ surface, β_p . The results in Chapter 4 show that for the ideal kink mode, the stability limits in β_p are sensitive to the current profile and the shape of the plasma cross section. Moreover, arbitrary low values of $\beta_{p,\text{crit}}$ can result with elliptic cross sections if the shear is reduced at the $q = 1$ surface.

The stability of resistive modes is generally strongly affected by central pressure gradients. First, the global effect of pressure gradients is to modify Δ' (i.e. transform the outer solutions, and therefore the coefficients A_l, B_\pm in eq.(6.1)). Secondly, pressure gradients locally at the $q = 1$ surface easily lead to violation of the resistive interchange criterion for equilibria with low shear and a sufficiently elongated cross section. Eq.(5.25),

$$-D_R \approx \frac{rp'}{\hat{s}^2 B_0^2} \left[\frac{3E}{r} \left(1 - \frac{8T R_0}{r} \right) - 2\hat{s}\Lambda \right] \quad (6.2)$$

shows that if the shear is small (and higher-order corrections are negligible), a slight ellipticity, $e \equiv E/r > 2\hat{s}\Lambda/3$, leads to violation of the resistive interchange criterion. The importance of the resistive interchange criterion on resistive stability can be seen from the dispersion relation of Glasser, Greene and Johnson [12], which reads in its simplified cylindrical form

$$\Delta'(Q) = \frac{2\pi \Gamma(3/4)}{L_R \Gamma(1/4)} Q^{5/4} \left(1 - \frac{\pi D_R}{4Q^{3/2}} \right). \quad (6.3)$$

($|D_R|$ is assumed small.) In eq.(6.3), $L_R = aS^{-1/3}$ is the resistive layer width of the interchange ordering, $Q = \gamma\tau_A S^{1/3}$ is the normalized growth rate, and the resistivity is indicated by the Lundquist number $S = \tau_r/\tau_A$.

According to the dispersion relation (6.3), the stability of the resistive modes at high S becomes almost entirely determined by the resistive interchange parameter. If the criterion is violated, $-D_R < 0$, there is always an unstable mode (for arbitrary Δ' and S), and for large S , its growth rate scales as $S^{-1/3} D_R^{2/3}$. On the other hand, if resistive interchanges are stable, $-D_R > 0$, tearing modes remain stable for Δ' less than some positive threshold Δ'_{crit} , which scales as $S^{1/3} (-D_R)^{5/6}$. We emphasize that, at high S , Δ'_{crit} becomes large, and the stability of resistive modes is completely dominated by the resistive interchange criterion.

In Chapter 6, effects of aspect ratio, shaping of the cross section, current profiles, pressure and wall separation on the resistive internal kink mode are investigated numerically, using the the equilibrium code CHEASE and the toroidal resistive stability code MARS. In the following study, the resistivity η is taken constant in space.

6.1 Dependence on aspect ratio, shaping, and wall separation without pressure

First, effects of aspect ratio, shear at the $q = 1$ surface and wall separation for different cross sections are studied for pressure-less equilibria. The plasma-vacuum interface of the equilibrium is prescribed by eq.(2.25). For the zero-pressure study, three different cross sections are chosen: circular (elongation $\kappa = 1$, triangularity $\delta = 0$ and $\zeta = 0$), elliptic ($\kappa = 1.7$, $\delta = 0$ and $\zeta = 0$), and JET [53] shape ($\kappa = 1.7$, $\delta = 0.3$ and $\zeta = 0$).

The current profile is specified by the surface averaged toroidal current density I^* . Two *flattened* current profiles as in Figure 4.6 are studied. Here, the plateau in I^* is located at $\rho = \rho_p \approx 0.44$. In Section 6.1, the $q = 1$ radius is fixed at $\rho \approx 0.40$, i.e., in the low-shear region inside the “knee” of the current profile at ρ_p . Two different values of the central shear have been chosen, so that the shear \hat{s} at $q = 1$ is about 0.04 and 0.07, and $q_0 \approx 0.935$ and 0.88, respectively. The shear varies only very slightly with respect to aspect ratio and the shape inside a certain radius, say $\rho < 0.6$.

6.1.1 Fixed boundary results for zero pressure

Holmes et al. [41] have shown that the resistive internal kink is stabilized by small aspect ratio and weak shear at the $q = 1$ surface. This is confirmed in Figure 6.1, which shows the fixed boundary growth rates of the resistive kink mode versus the

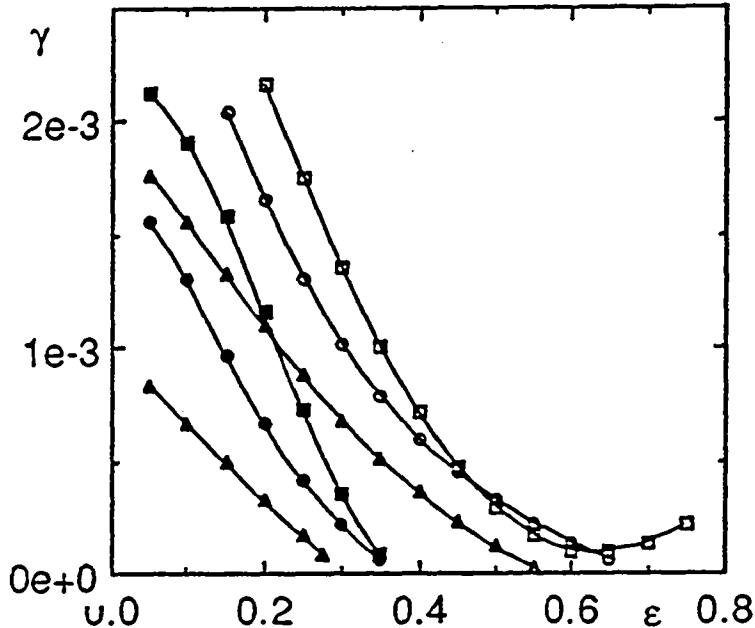


Figure 6.1: Fixed boundary resistive growth rates γ at $S = 10^6$ versus inverse aspect ratio ϵ , for zero pressure equilibria with different shapes: circle, ellipse (squares), and JET shape (triangles). The flattened current profile has been used with different central shear (closed symbols: low shear, open symbols: high shear).

inverse aspect ratio $\epsilon = a/R_0$ at a Lundquist number of $S = 10^6$ for the flattened current profile. The various curves refer to the three cross sections (circle, ellipse and JET shape) and the two different values of central shear. The resistive internal kink is stabilized for aspect ratios below a threshold that varies inversely with the shear.

Figure 6.1 shows that shaping is also important for internal kink stability, in particular, at large aspect ratio. For example, the elliptic case ($\kappa = 1.7$, $\delta = 0$) shows strong instability as the aspect ratio increases. The destabilization by ellipticity has been analyzed for ideal modes at large aspect ratio [39,57]. It is connected to contributions proportional to $(\kappa - 1)^2$ in the normalized potential energy $\delta\mathcal{W}_p/a^2$. The destabilizing

elliptic term competes with the $\mathcal{O}(\varepsilon^2)$ stabilizing toroidal contribution [11]. At fixed shape, the elliptic shaping terms dominate over the toroidal term when the aspect ratio increases, and an elliptical equilibrium with $q_0 < 1$ is ideally unstable at large aspect ratio. As seen from Figure 6.1, the resistive internal mode is significantly destabilized by an ellipticity of $\kappa = 1.7$, for aspect ratios of interest. However, a triangularity of $\delta = 0.3$, in combination with the same ellipticity (JET shape), improves stability over the circle. This is connected to stabilizing terms of order δ^2 and $\varepsilon(\kappa - 1)\delta$ in $\delta\mathcal{W}_p/a^2$, which become significant at large aspect ratio.

At low aspect ratio, the stabilizing toroidal effects tend to dominate over the shaping effects. Figure 6.1 shows that, for the low shear profile, the three shapes are stabilized at roughly the same aspect ratio, $A = R_0/a \approx 3$. For the higher central shear, the circular and the JET-shaped equilibria are stable for A less than about 1.5 and 1.8, respectively. The equilibria with higher central shear and an elliptic cross section are never completely stable, and the resistive growth rates increases again for $\varepsilon > 0.6$.

To summarize, the results of Figure 6.1 for the fixed boundary internal kink at zero pressure: toroidicity and weak shear at the $q = 1$ surface are stabilizing and ellipticity is destabilizing, but a combination of ellipticity and sufficient triangularity is more stable than a circular equilibrium.

6.1.2 Free boundary results for zero pressure

Next, the effects of free boundary are considered. Figure 6.2(a) shows the growth rate of the $n = 1$ mode at $S = 10^6$ for a circular zero beta equilibrium (the case of weak central shear in Figure 6.1). One curve gives the result for a fixed boundary and the two other apply to free boundary modes with a conducting wall placed at a minor radius of $b = 1.2a$.

At large aspect ratio, the two free boundary modes correspond in an unambiguous way to their cylindrical counterparts: one is the internal “ $m = 1$ ” and the other the external “ $m = 2$ ” mode. For the equilibria considered here, the external mode is

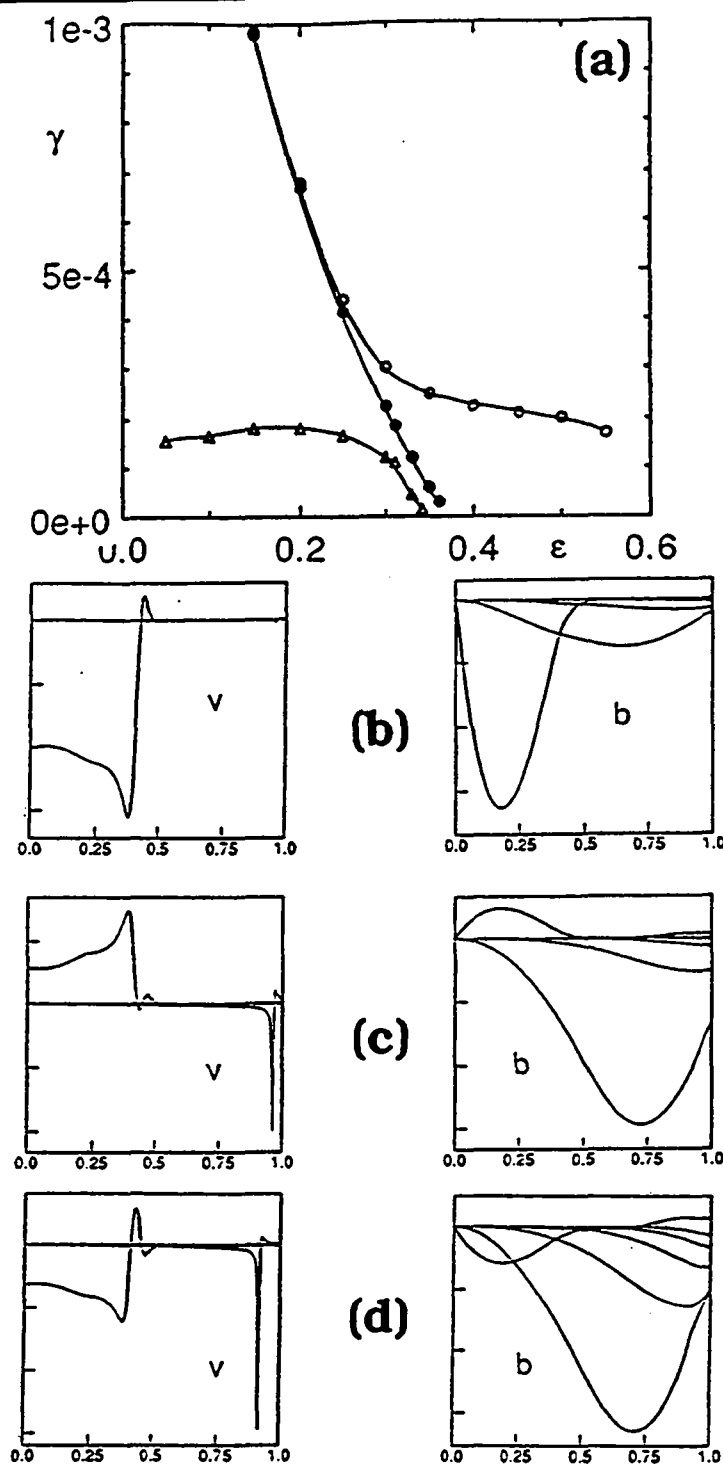


Figure 6.2: Resistive instabilities of a circular equilibrium with a flattened current profile, low central shear, and zero pressure.

(a) Growth rates γ at $S = 10^6$ versus inverse aspect ratio ϵ . The closed circles refer to the fixed boundary modes, while the open symbols show the results with a free boundary and a conducting wall at a radius $b = 1.2a$.

(b)-(d) Fourier components of the radial perturbed velocity $v = v \cdot \nabla \Psi^{1/2}$ and the magnetic flux $b = JB \cdot \nabla \Psi^{1/2}$ in straight field line coordinates [$J = C(\Psi)R^2$] for the free boundary mode.

(b) The “ $m = 1$ ” mode for $A = 5$. (c) The “ $m = 2$ ” mode for $A = 5$.

(d) The single unstable mode for $A = 2.5$.

The $m = 1$ and $m = 2$ components of the magnetic flux reinforce one another on the outboard side for the fast growing branch [(b) and (d)] and on the inside for the slower branch (c).

stable with the wall on the plasma, but it becomes unstable for wall radii $b > 1.1a$. Figure 6.2(a) shows that, as the aspect ratio decreases, the “ $m = 1$ ” mode becomes increasingly stable, whereas the free boundary “ $m = 2$ ” mode is only weakly affected by toroidicity. At a certain aspect ratio ($A \approx 3$ for this case), the two branches cross over and the identification of internal or “ $m = 1$ ” and external or “ $m = 2$ ” breaks down. For aspect ratios below the crossover, the branch connected to the large aspect ratio internal mode acquires a dominant $m = 2$ magnetic component and transforms into an “external” mode with a growth rate almost independent of A , and the large aspect ratio external branch is stabilized. (Note that the “ $m = 2$ ” mode is independent of aspect ratio only for low pressure. For higher pressure, the toroidal effects on the “ $m = 2$ ” mode are stabilizing because of favorable curvature at the $q = 2$ surface.) Figure 6.2(b)-(d) show the radial displacement and the perturbed magnetic flux for the two different modes at aspect ratio $A = 5$ and the single unstable mode at $A = 2.5$. The mixture of the $m = 1$ and $m = 2$ displacements localized around the $q = 1$ and $q = 2$ surface is evident, and the relative sign of the $m = 1$ and the $m = 2$ components is different for the two branches. For the more unstable branch, the $m = 1$ and $m = 2$ magnetic perturbations reinforce one another on the outboard side.

The cases shown in Figure 6.2 indicate that the current profile must be stable to the $m = 2/n = 1$ tearing mode in the straight tokamak approximation, in order to be completely stable at finite aspect ratio and zero pressure. One way to stabilize the $m = 2$ tearing mode is to decrease q_0 to values substantially below unity. However, for such profiles, the shear must be reduced locally at the $q = 1$ surface in order for the $m = 1$ resistive kink to remain stable. Thus, at zero pressure, free boundary stability can be achieved at finite aspect ratio by a TEXTOR profile as in Figure 4.9 with q_0 well below unity and shoulders in the current profile, which reduce the shear at $q = 1$. The free boundary growth rate for this equilibrium is shown as a function of the aspect ratio in Figure 6.3. The *external* mode is now stable at all aspect ratios and the *internal* mode is stabilized for aspect ratios below approximately 10. Thus, the TEXTOR profile

with zero pressure is completely resistively stable for aspect ratios typical of tokamaks. The shear at $q = 1$ for this equilibrium is $\hat{s} \approx 0.035$, which is similar to the flattened profile of low central shear in Figure 6.1, but the internal mode is stabilized at much larger aspect ratio for the TEXTOR profile.

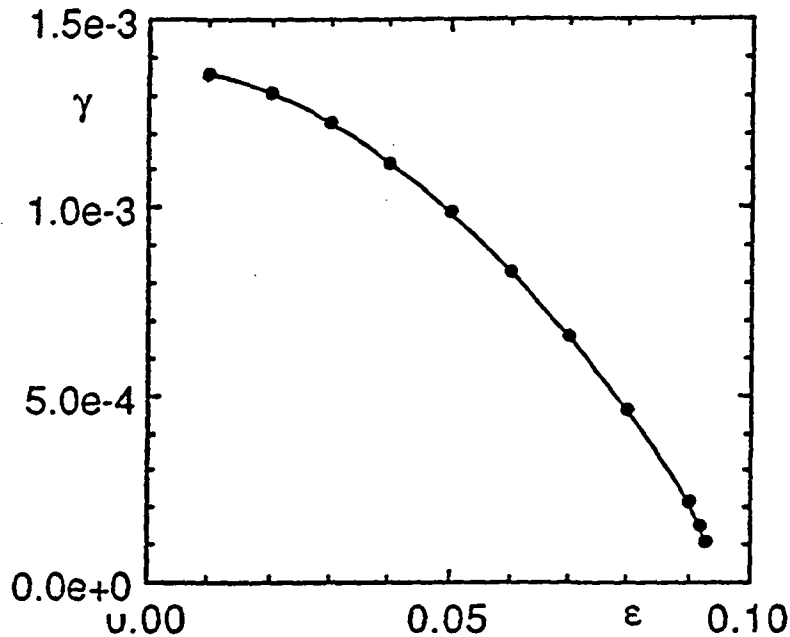


Figure 6.3: Free-boundary resistive growth rates γ at $S = 10^6$ versus inverse aspect ratio ϵ , for a circular equilibrium with TEXTOR current profile and zero pressure. A conducting wall is assumed at $b = 1.2a$. Note the absence of an “ $m = 2$ ” branch and the complete stability at low aspect ratio.

The examples in Figures 6.2-6.3 show that the stability of the resistive internal kink at zero pressure is sensitive to the current profile, aspect ratio, and wall position. Coupling to the external “ $m = 2$ ” mode becomes important at low aspect ratio. Stability to both the internal and external free boundary modes at zero pressure appears to require nonmonotonic current profiles of the TEXTOR type. In the following, we shall mainly consider the purely internal modes by imposing a fixed boundary.

6.2 Pressure effects

To illustrate the significance of the layer effects for the internal kink mode, we show in Figure 6.4-6.6 the resistive growth rate versus inverse aspect ratio for three different cross sections: circle: $\kappa = 1$, $\delta = 0$ and $\zeta = 0$ (Figure 6.4), weakly oblate: $\kappa = 0.9$, $\delta = 0$ and $\zeta = 0$ (Figure 6.5), and JET shape: $\kappa = 1.7$, $\delta = 0.3$ and $\zeta = 0$ (Figure 6.6). In all cases, $\beta_p = 0.05$ and $S = 10^7$, and we have used the flattened current profile with low central shear and $q_0 \approx 0.935$. The pressure profile is the same as the one used for the ideal cases, Figure 4.2, and the $q = 1$ surface is in the low-shear region at $\rho \approx 0.40$ as in Section 6.1.

Figure 6.4(a) shows the resistive growth rate versus ϵ for equilibria with a circular boundary, $\beta_p = 0.05$, and two different wall positions $b = a$ and $b = 1.2a$. By comparison with Figure 6.1, the major effect of finite pressure is that the *fixed boundary* mode remains unstable also at low aspect ratio. This mode is now dominated by the $m = 1$ component. The mode is only weakly dependent on the wall position, and is driven unstable by interchange effects. Figure 6.4(b) shows that the resistive interchange criterion becomes increasingly violated at low aspect ratio. The principal reason for this appears to be the small natural ellipticity of the *internal* flux surfaces at finite aspect ratio. The ellipticity $e_{q=1}$ of the $q = 1$ surface is shown in Figure 6.4(b). With a circular boundary, the ellipticity of the internal surfaces is, to leading order, proportional to ϵ^2 ($e_{q=1} \approx 5.98 \cdot 10^{-2} (a/R_0)^2$ for the equilibria in Figure 6.4). For $A < 3$, the destabilizing ellipticity correction in the resistive interchange criterion dominates over the stabilizing shear term. Thus, even though the plasma boundary is circular, the $\mathcal{O}(\epsilon^2)$ modifications of the shape of the internal surfaces change the stability of the internal kink significantly at relevant aspect ratios. This current profile is particularly sensitive to “small” effects because of the low shear on $q = 1$, but similar behavior is observed for the equilibrium with higher shear in Section 6.1.1. (For the sequence of equilibria in Figure 6.4, where the current profile is held fixed, the shear depends weakly on the

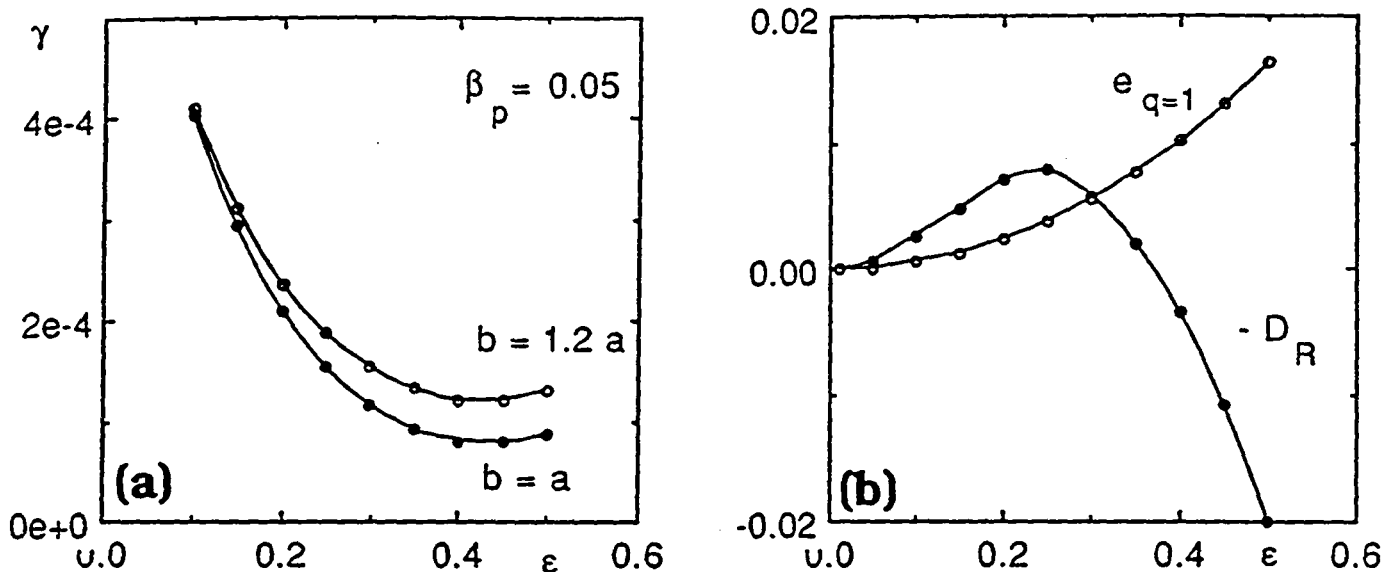


Figure 6.4: Stability results for a circular equilibrium with a flattened current profile, low central shear, and $\beta_p = 0.05$.

(a) Resistive growth rate γ for $S = 10^7$ versus inverse aspect ratio ϵ . The fixed boundary results are shown as closed circles and the open circles refer to the conducting wall at $b = 1.2a$.

(b) The resistive interchange parameter $-D_R$ (closed circles) and ellipticity e (open circles) at the $q = 1$ surface.

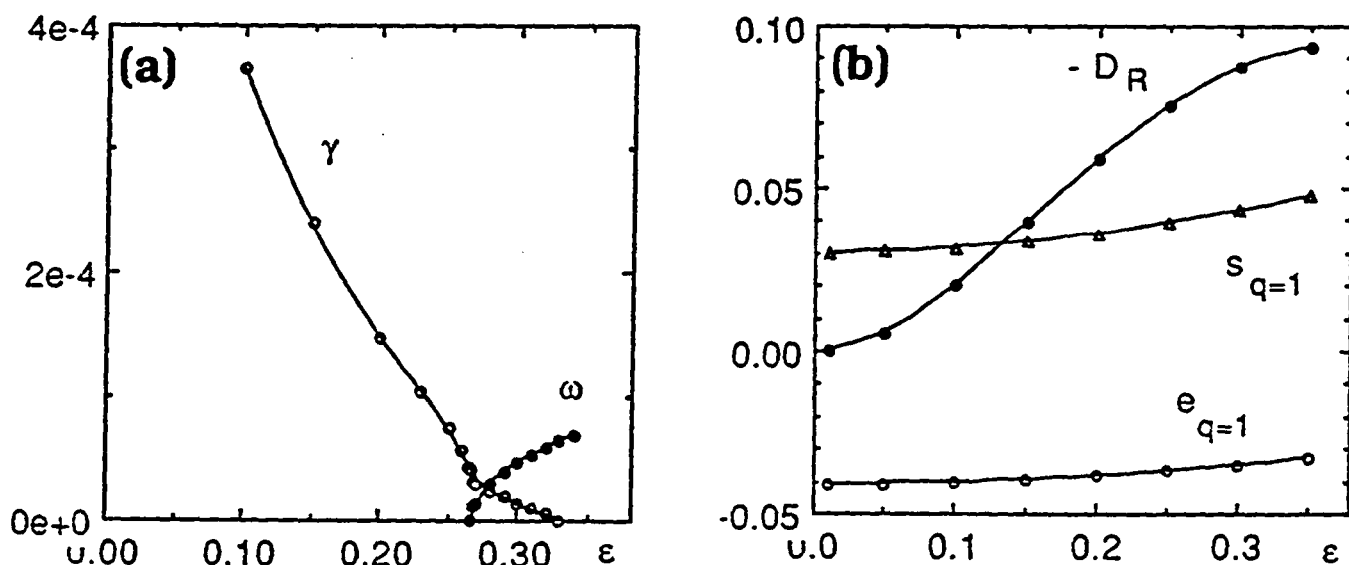


Figure 6.5: Stability results for a weakly oblate equilibrium with a flattened current profile, low central shear, and $\beta_p = 0.05$.

(a) Free boundary resistive growth rate γ for $S = 10^7$ versus inverse aspect ratio ϵ with a conducting wall at $b = 1.2a$. The open circles show the growth rate and the closed circles show the real part of the frequency.

(b) The resistive interchange parameter $-D_R$ (closed circles), ellipticity e (open circles) and shear \hat{s} (open triangles) at the $q = 1$ surface.

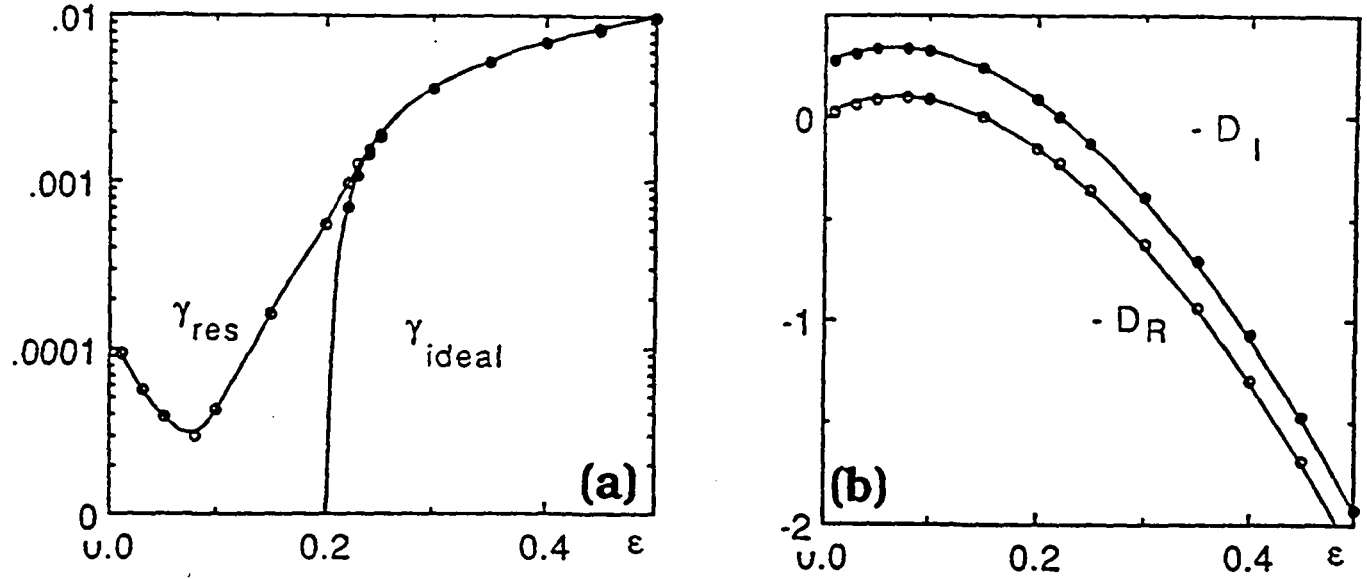


Figure 6.6: Stability results for a JET-shaped equilibrium with a flattened current profile, low central shear, and $\beta_p = 0.05$.

(a) Fixed boundary growth rate versus inverse aspect ratio ϵ . The open circles show the resistive mode for γ for $S = 10^7$ and the closed circles refer to the ideal case.

(b) The resistive and ideal interchange parameter $-D_R$ (open circles), and $-D_I$ (closed circles) versus inverse aspect ratio.

aspect ratio, but this not significant. It should be remarked that the large aspect ratio expansion that led to eq.(5.24) is not strictly valid when the ellipticity is of order ϵ^2 , but eq.(5.24) nevertheless seems to give a good approximation.)

Figure 6.5(a) shows the growth rate for weakly oblate equilibria with $\kappa = 0.9$ and $\beta_p = 0.05$. With decreasing aspect ratio, the growth rate first decreases, then becomes complex, and finally the mode is completely stabilized, as predicted by the theory of Glasser et al. [12]. The resistive interchange criterion is satisfied, because the $q = 1$ surface remains oblate also for small aspect ratios [$e_{q=1} \approx (-4.09 + 6.6a^2/R_0^2) \times 10^{-2}$]. For these oblate equilibria, the internal kink mode is completely stable at low aspect ratio and moderate pressure. Even though both the deviation from circular boundary ($\kappa = 0.9$) and the S number (10^7) are modest, the resistive internal kink mode behaves quite differently than in the case of a circular boundary. With more pronounced shaping and larger S , the influence of curvature of course becomes stronger.

Figure 6.6(a) shows the growth rate for the JET-shaped equilibrium ($\kappa = 1.7, \delta = 0.3$). These results differ clearly from those of the two previous cases. With JET shape and $\beta_p = 0.05$, the growth rate *increases* with ϵ for $\epsilon \geq 0.08$. The internal kink is now *ideally* unstable for $\epsilon > 0.21$ and its growth rate is high ($> 5.10^{-3}\omega_A$) at low aspect ratio. The reason for the ideal instability at low β_p can be seen in Figure 6.6(b): the ideal interchange criterion is violated for $\epsilon > 0.22$. Ideal instability sets in almost exactly when the Mercier criterion is violated and the growth rate soon reaches large values. For $0.14 < \epsilon < 0.22$, only the resistive interchange criterion is violated, and the equilibrium is resistively unstable with much smaller growth rates.

It may be noted, as a curiosity, that at large aspect ratio, $\epsilon < 0.14$, the resistive interchange criterion indicates stability for these JET-shaped equilibria and the growth rate at moderate pressure is reduced *below* the zero beta value. This is connected to the stabilizing influence of triangularity in combination with ellipticity; see eq.(5.25). For fixed shape (E, T independent of ϵ) the stabilizing terms proportional to $E \times T$ become dominant at large aspect ratio. Of course, in the limit of $\epsilon \rightarrow 0$ with β_p fixed, the pressure effects become negligible ($-D_I \rightarrow 1/4$ and $-D_R \rightarrow 0$), and the resistive kink mode of the straight tokamak reappears.

6.3 Current profile effects

6.3.1 Circular shape

In this Section, we study the influence of the current profile in combination with finite pressure and shaping, and discuss how a sawtooth crash might be triggered by changes in the current profile. We first consider circular cross section and two types of current profiles: the flattened (I) (see Figure 4.6) and the TEXTOR (II) profile (see Figure 4.9). The current profiles are prescribed except for a multiplicative factor that is adjusted to specify the $q = 1$ radius or the q value at a specified radius, $q_p = q(\rho_p)$, using the equilibrium transformations described in Section 2.5.

For the flattened profile (I), the shear is low in a central region and has a local

minimum at $\rho = \rho_p = 0.44$, where $dI^*/d\rho = 0$. Outside this radius, the shear increases rapidly. The minimum shear $\hat{s}(\rho_p)$ is about 0.03 and the central safety factor is given by $q_0 \approx 0.935q_p$. For $q_p > 1$, the $q = 1$ surface is in the central region of low shear, but when q_p decreases below unity, it moves into the outer region of rapidly increasing shear. Minimum shear at $q = 1$ occurs for $q_p = 1$. A sequence of self-similar equilibria with decreasing q_0 may correspond approximately to the time evolution during the ramp phase of a sawtooth, if the preceding crash leads to complete reconnection and almost flat central q , followed by peaking of the current due to trapped particle effects [62]. The pressure profile is the same as in Section 4.2. The central beta is related to β_p at $q = 1$ by $\beta_0 \approx 0.096\beta_p$ and the volume averaged beta is $\langle \beta \rangle \equiv 2\mu_0 \langle p \rangle / \langle B^2 \rangle \approx 0.039\beta_p$.

Figures 6.7 and 6.8 show the growth rates of the internal kink mode for the flattened current profile as functions of q_p at different pressure and resistivities. The aspect ratio is 4 and a conducting wall is assumed at a radius of $b = 1.2a$. Complete resistive, free-boundary stability is never achieved for the flattened current profile. However, for $\beta_p \leq 0.05$, the resistive growth rate is small when the $q = 1$ surface is in the region of small shear, and the mode is predominantly external with a large $m = 2$ magnetic perturbation. Such weak instabilities may well be stabilized by effects not included in linear resistive MHD. By comparing Figure 6.7 for $S = 6 \cdot 10^6$ and Figure 6.8 for $S = 6 \cdot 10^8$, one can identify regions of resistive and ideal instability. The instabilities for $\beta_p \geq 0.15$ and $q_p < 1$ (when the $q = 1$ surface is in the outer region of high shear) are ideal. The normalized growth rates are several times 10^{-3} and are almost independent of resistivity. The growth rate peaks when the shear at $q = 1$ is small, as expected for ideal modes [11,63]. By contrast, for $\beta_p \leq 0.05$, the instabilities are resistive. The growth rates follow the tearing scaling with respect to resistivity and have a minimum when the shear is small at $q = 1$. Figure 6.8 shows that the resistive growth rates are very small at high S . These growth rates do not even come close to those observed experimentally in sawtooth precursors where, typically, $\gamma/\omega_A > 10^{-3}$.

An interesting feature can be seen in the cases with $\beta_p \geq 0.15$. The pressure-driven

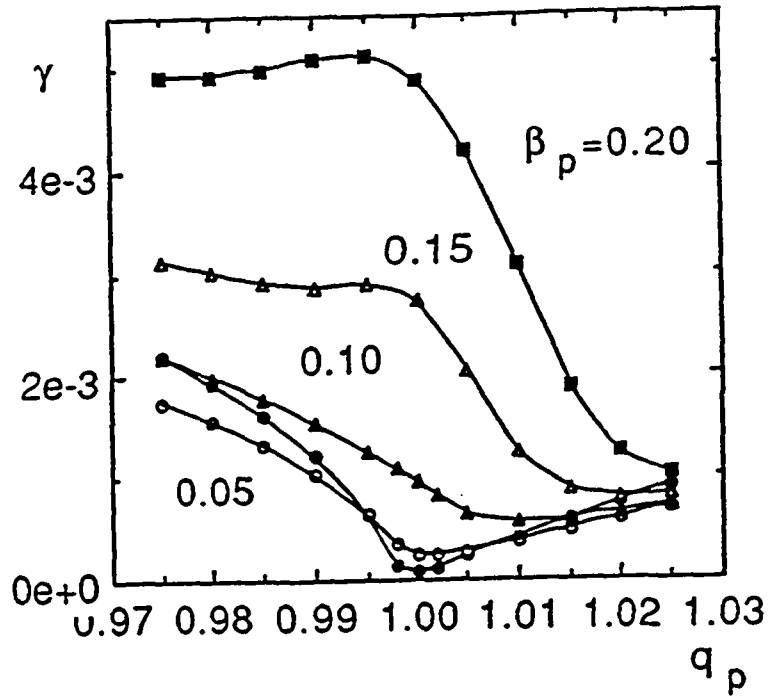


Figure 6.7: Free-boundary growth rates for $S = 6.10^6$ versus the safety factor q_p at the radius of minimum shear ($\rho \approx 0.44$) for a circular equilibrium with a flattened current profile, low central shear, and different β_p . The aspect ratio is 4 and the conducting wall is at a radius $b = 1.2a$.

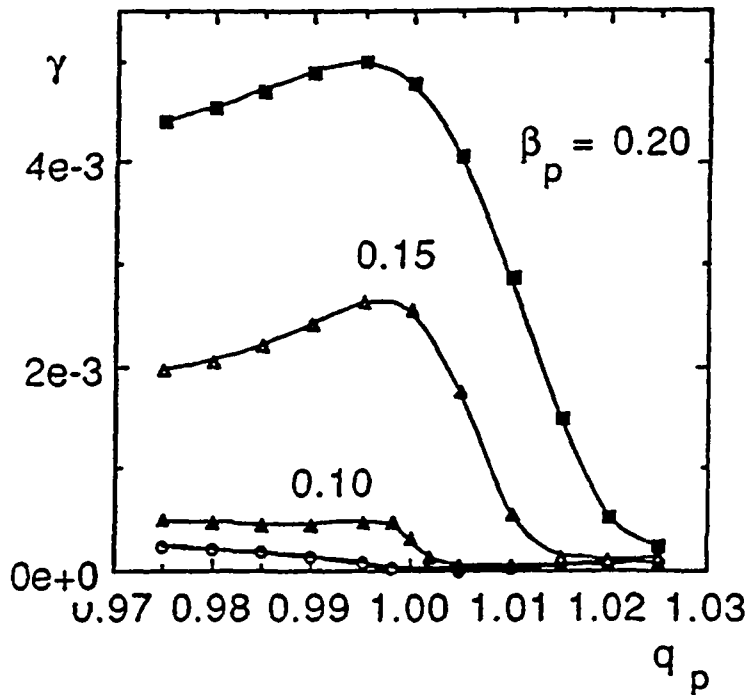


Figure 6.8: Free-boundary growth rates versus q_p . All parameters are identical to Figure 6.7, except $S = 6.10^8$.

instabilities are sensitive to the value of q_p , or to the location of the $q = 1$ surface with respect to the knee of the current profile. The finite-beta growth rates have maxima when the $q = 1$ surface is at the radius of minimum shear and remain high when the $q = 1$ surface reaches the outer, high-shear region. Thus, a “pressure-driven” instability may be triggered by changes in the current profile rather than by an increase in the pressure itself.

For comparison with other geometries, we note that the resistive interchange criterion generally indicates stability for circular cross section with $A = 4$, but $-D_R$ takes small positive values (due to finite shear rather than favorable curvature). The growth rates are generally slightly larger for $\beta_p = 0$ than for $\beta_p = 0.05$ because of the increased inertia associated with the motion along the field lines in the finite beta case.

The details of the results in Figure 6.7 and 6.8 depend on the current profile. For instance, if the central shear is reduced, the ideal pressure-driven instabilities are enhanced, while the growth rates of the resistive instabilities for low pressure are reduced.

Next, we consider the TEXTOR current profile. The shoulders in I^* have been adjusted so that the shear has a minimum of about 0.034 at $\rho = \rho_p \approx 0.44$. The central q is $q_0 \approx 0.634q_p$, and the aspect ratio is 4. Figures 6.9 and 6.10 show the growth rates for different S and central pressures. The behavior is similar to that for the centrally flat profiles, but the TEXTOR profile supports about twice the pressure before becoming ideally unstable. At high pressure, $\beta_p \geq 0.2$, the growth rates are very sensitive to the position of the $q = 1$ surface. For the TEXTOR profile, there is indeed an interval q_p , where the equilibrium is *entirely* stable. However, this interval is small, and certainly less than the shift in q during the sawtooth cycle.

As discussed in Section 6.1, low aspect ratio is stabilizing for the internal kink mode. An example is given in Figure 6.11 which shows the growth rate γ as a function of q_p for a sequence of equilibria with aspect ratio $A = 2.5$ and a TEXTOR current profile. Figure 6.11 refers to $S = 6.10^8$ and differs from Figure 6.10 only with respect to the aspect ratio. We note that the region of complete stability is larger at the smaller

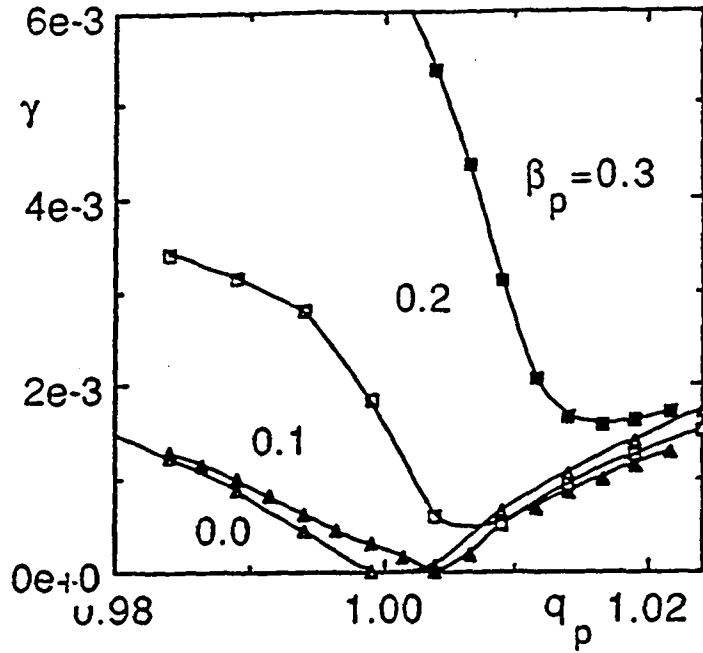


Figure 6.9: Free-boundary growth rates for $S = 6.10^6$ versus the safety factor q_p at the radius of minimum shear ($\rho \approx 0.44$) for a circular equilibrium with TEXTOR current profile and different values of β_p . The aspect ratio is 4 and the conducting wall is at a radius $b = 1.2a$.

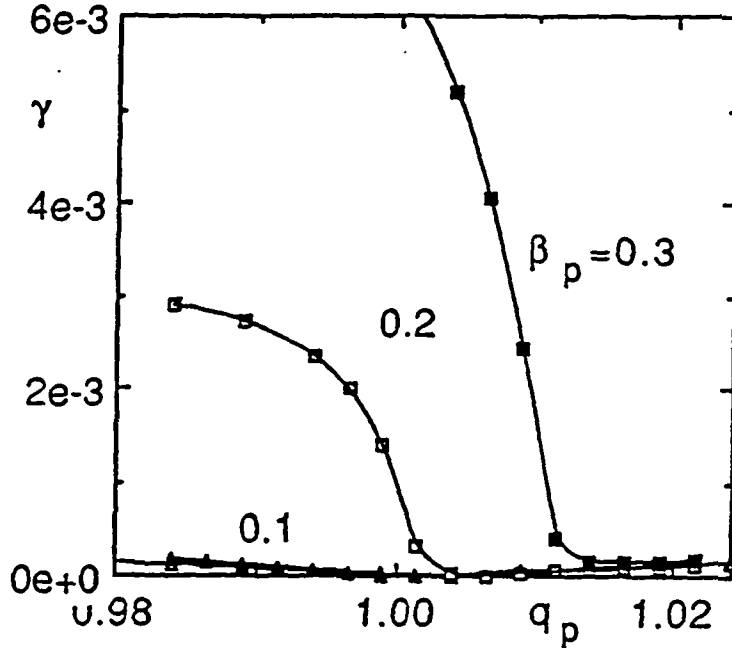


Figure 6.10: Free-boundary growth rates versus q_p . All parameters are identical to Figure 6.9, except $S = 6.10^8$.

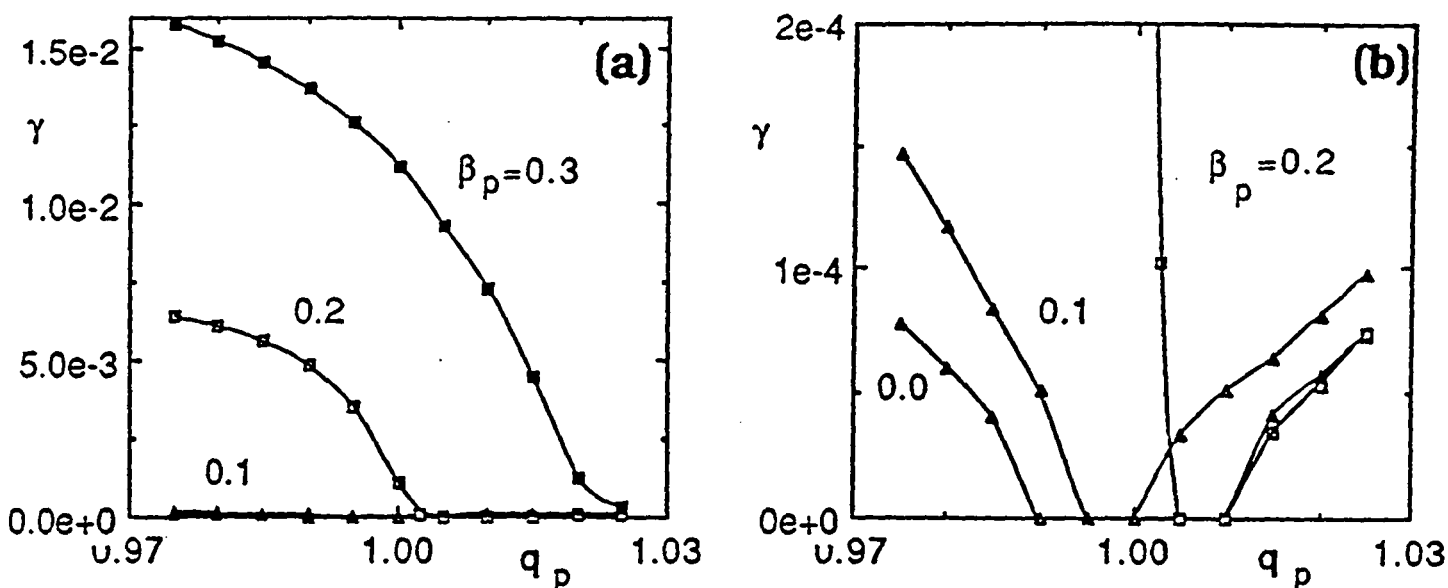


Figure 6.11: Free-boundary growth rates versus the safety factor q_p at the radius of minimum shear ($\rho \approx 0.44$) for a circular equilibrium with TEXTOR current profile. All parameters are identical to Figure 6.10, except that the aspect ratio $A = 2.5$. (a) shows the full range of γ and (b) is a blowup to show the stable region.

aspect ratio, and that there is even a small interval in q_p , giving complete resistive stability for $\beta_p = 0.20$.

6.3.2 JET shape

As noted in Section 6.1, the ellipticity of the $q = 1$ surface in a JET-shaped cross section can cause ideal instability at moderate pressure if the shear at $q = 1$ is small. In order not to be dominated by interchange effects, we consider current profiles with higher shear in this paragraph. To show the dependence on the shear, we choose two values of the minimum shear for each of the two types of profiles: *flattened*, denoted (I-H) and (I-L) for high and low shear, respectively, and TEXTOR, denoted (II-H) and (II-L). The shear at $q = 1$ is shown in Figure 6.12 for the four profiles versus $q_p = q(\rho = \rho_p \approx 0.41)$. The fixed boundary growth rates at $S = 6.10^8$ are shown for different pressures in Figures 6.13-6.15. Figure 6.13 shows that at zero pressure, the growth rates are similar for the four different current profiles. The growth rate at zero pressure are generally lower than for the circular case with $A = 4$. However, the JET cross section is more sensitive to pressure, and a clear increase in growth rates resulting from $\beta_p = 0.05$ is evident in Figure 6.14. None of the current profiles is resistively stable for this pressure in JET geometry. However, the large shear profiles have small growth rates for $\beta_p = 0.05$, in particular, the TEXTOR current profile. The pressure-driven instability for the low-shear TEXTOR profile is highly sensitive to the q value.

For higher pressure, $\beta_p = 0.10$ (Figure 6.15), the two centrally flat profiles both give rather large growth rates for all values of q_p , whereas the TEXTOR profile gives normalized growth rates as small as a few times 10^{-4} when $q_p > 1$, i.e. when the $q = 1$ surface is inside the shoulder.

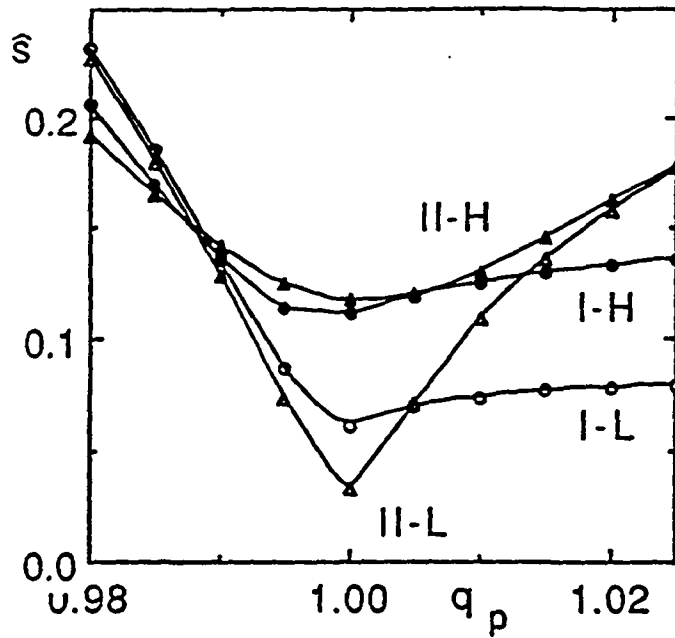


Figure 6.12: Shear at the $q = 1$ surface versus the safety factor q_p at the radius of minimum shear ($\rho \approx 0.41$) for JET-shaped equilibria with $A = 2.7$ and different current profiles. Circles indicate the flattened, and triangles the TEXTOR current profile. Open symbols represent low, and closed symbols high central shear.

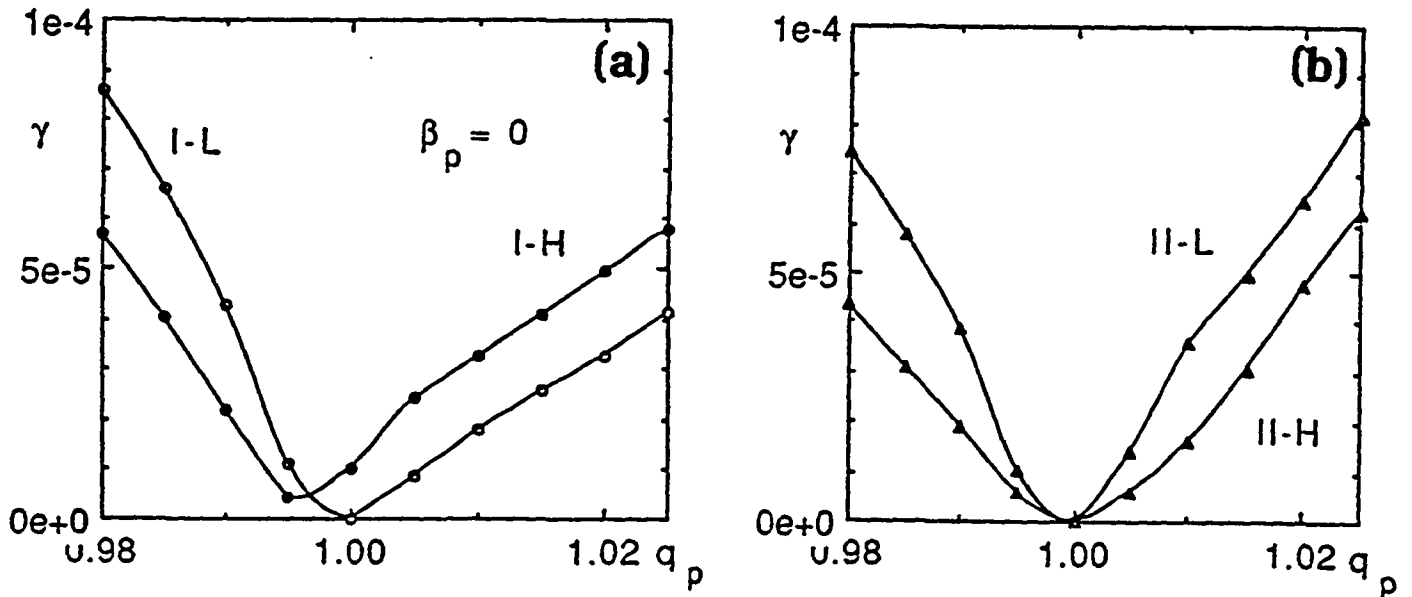


Figure 6.13: Fixed boundary growth rates for $S = 6.10^8$ versus the safety factor q_p at the radius of minimum shear ($\rho \approx 0.41$) for JET-shaped equilibria with different current profiles and zero pressure. (a) shows the results for the flattened current profiles and (b) the TEXTOR profile.

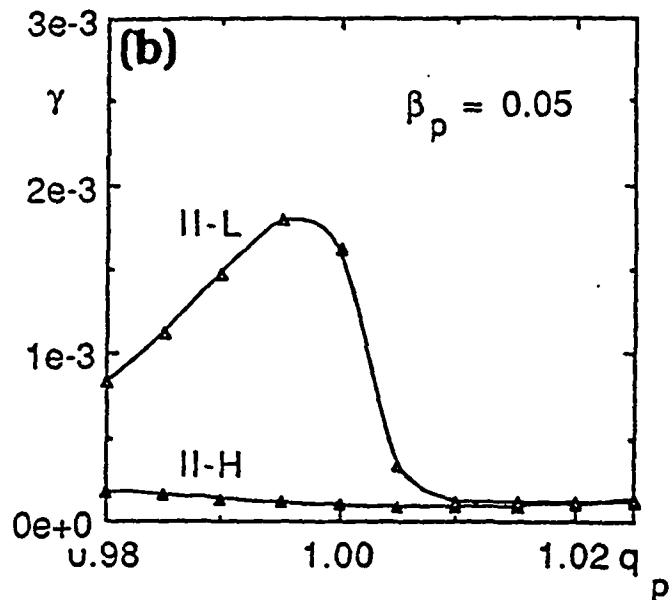
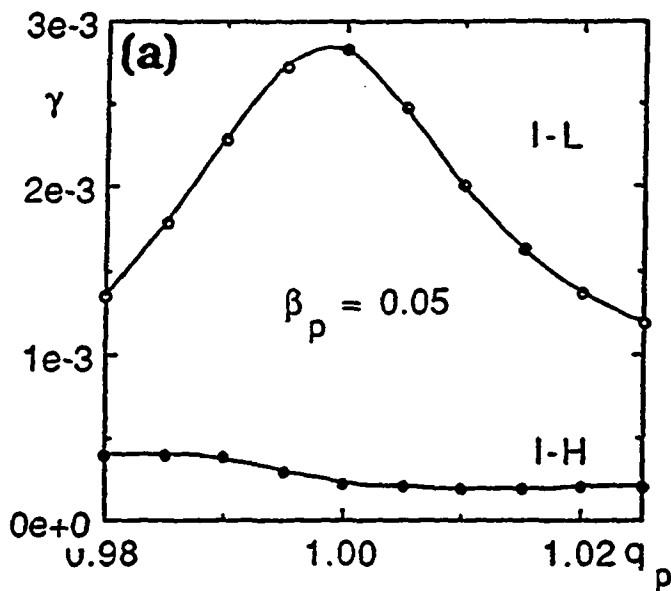


Figure 6.14: Identical to Figure 6.13, except $\beta_p = 0.05$. (a) shows the results for the flattened current profiles and (b) the TEXTOR profile.

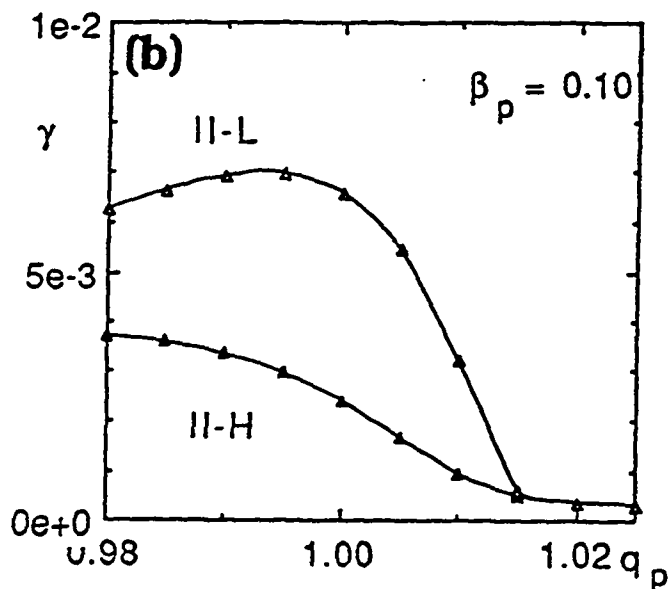
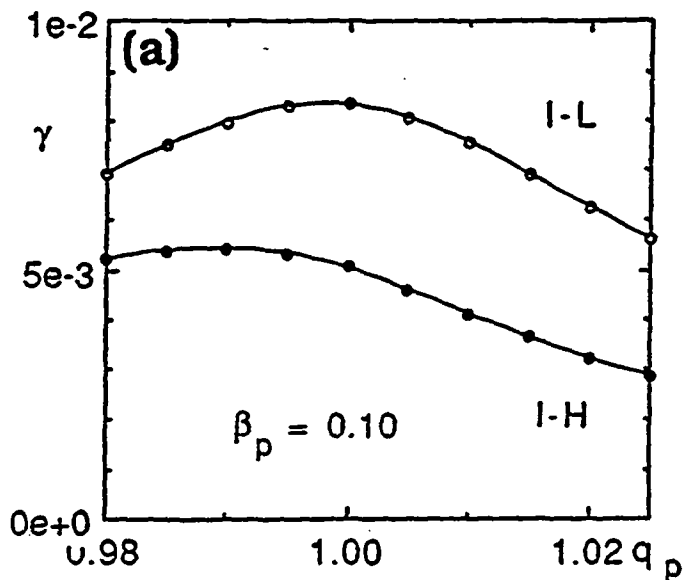


Figure 6.15: Identical to Figure 6.13, except $\beta_p = 0.10$. (a) shows the results for the flattened current profiles and (b) the TEXTOR profile.

6.3.3 Oblate cross section

To illustrate the importance of the average curvature, we again consider the slightly academic example of an oblate cross section (elongation $\kappa = 0.9$, triangularity $\delta = 0$, and aspect ratio $A = 4$). The current profile is of the TEXTOR type with a minimum shear of 0.042. The growth rate for $\beta_p = 0.05$ and $S = 6.10^7$ is shown in Figure 6.16. When the $q = 1$ surface is located near the radius of minimum shear, the growth rate becomes complex, and in a certain interval, $0.995 < q_p < 1.005$, the mode is stabilized, evidently as a result of favorable curvature at $q = 1$. The resistive interchange parameter at $q = 1$, $-D_R$, indicates stability and reaches a maximum of about 0.07.

For higher pressure, $\beta_p = 0.10$, and the oblate cross section, the destabilizing global effects of pressure dominate over the stabilizing layer effects, and the resistive internal kink is no longer stable for any $q_0 < 1$.

6.4 Summary of results on resistive stability

The results on the stability of resistive internal kink modes show that although low shear is stabilizing at zero pressure, it tends to be destabilizing even for very modest central pressure gradients because of interchange instability. This effect is strong for elliptic shaping (including JET shape) which makes the averaged curvature on $q = 1$ unfavorable. For JET shape, we have found no case with $\beta_p \geq 0.05$ that is resistively stable, and complete resistive stability with free boundary was found only for current profiles of the TEXTOR type with shoulders (or at low shear and very low pressure). Stabilization for the TEXTOR profile requires a very careful tuning of parameters, e.g., specification of q with a precision of half a percent.

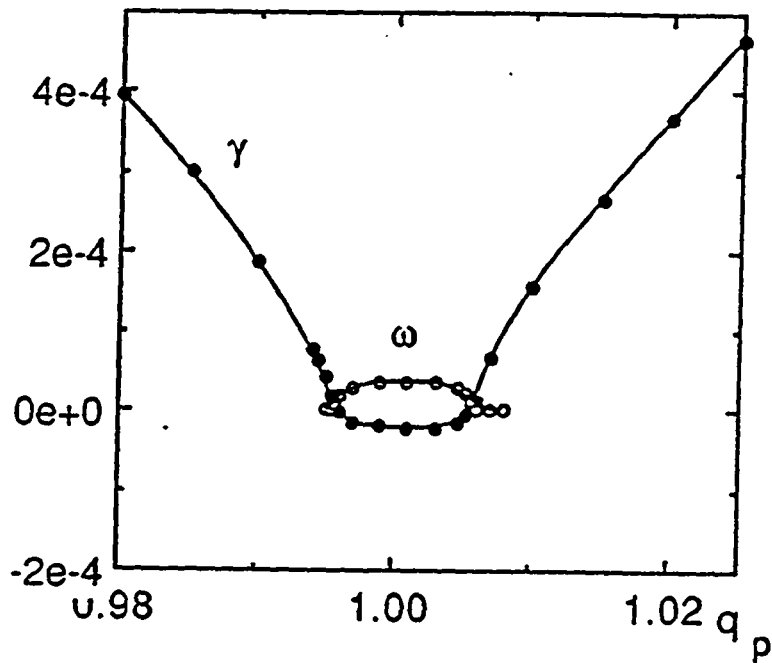


Figure 6.16: Free-boundary growth rates for $S = 6.10^7$ versus the safety factor q_p at the radius of minimum shear ($\rho \approx 0.44$) for a weakly oblate equilibrium with TEXTOR current profile and $\beta_p = 0.05$. The aspect ratio is 4, and the conducting wall is at a radius $b = 1.2a$. Closed circles show the growth rate and open circles show the real frequency.

Chapter 7

Summary

7.1 Cubic Hermite element equilibrium code

The Hermite bicubic elements have proved their efficiency for the resolution of the Grad-Shafranov equation. The convergence rates of the equilibrium solution agree with the theoretical predictions, despite the special treatment on the axis of the modified polar mesh used for the discretization. A comparison with the linear “hybrid element” equilibrium code CLIO shows that the computation of the position of the magnetic axis for a nonlinear JET equilibrium is as precise with CHEASE on a 20×20 discretization mesh as with CLIO on a 300×300 mesh.

To study the effect of the equilibrium calculation and the mapping to flux coordinates on the accuracy of the stability calculations, we have shown convergence tests with the stability codes ERATO using two-dimensional linear “hybrid elements”, and MARS, where Fourier decomposition is used in the poloidal direction. For both codes, the error due to the equilibrium solver on the stability results converges in $\mathcal{O}(h^3)$, to be compared with the $\mathcal{O}(h)$ error if second order accurate finite differences are used for the discretization of the equilibrium. Therefore, CHEASE provides equilibria for these stability codes which are accurate enough for computing routinely instability growth rates below $10^{-2}\omega_A$, which is typical for internal kink modes in tokamaks.

CHEASE has been equipped with a number of commonly-used profile specifications, and is interfaced with the stability codes ERATO and NOVA-W (ideal MHD),

MARS and PEST-3.4 (resistive MHD) and LION (Alfvén and ion cyclotron range of frequencies).

7.2 MHD stability of internal kink modes in tokamaks

For circular cross sections, the ideal full-MHD stability of the internal kink mode at typical aspect ratios is quite well described by the large aspect ratio theory. The large aspect ratio calculation of Bussac et al. [11] has been modified with respect to the boundary conditions so that it applies for tokamak equilibria with $q_a > 2$. With this modification, the large aspect ratio expansion typically predicts β_p -limits in the range of 0.1 to 0.2, in good agreement with our numerical full-MHD results. Most current profiles give β_p -limits that decrease monotonically with increasing $q = 1$ radius. Both large aspect ratio theory and numerical computations show instability at low values of q_0 . The stability of the internal kink is dependent on the current profile, e.g., the Shafranov profile is less stable than profiles that are rounded in the central region, while current profiles with shoulders just outside the $q = 1$ surface are more stable.

With regard to shaping, ellipticity was found to reduce significantly the β_p limit. For JET geometry, typical values of the marginal β_p are between 0.03 and 0.1. The reduction of the pressure limit by elongation is accentuated in cases of weak shear in the $q \leq 1$ region, correlated with violation of the Mercier criterion. A large aspect ratio expansion of the Mercier criterion including the lowest order effects of ellipticity and triangularity is given by eq.(5.24) and confirms the strong destabilizing effect of elongation on the internal kink mode.

The resistive internal kink is sensitive to a large number of effects, and the following is an attempt to delineate the most important of these.

For zero pressure, the resistive MHD stability of the internal kink is influenced primarily by the aspect ratio and the current profile. The low aspect ratio is stabilizing. Stability is improved by low shear at the $q = 1$ surface, but also by low q_0 . Equilibria

with monotonic current profile are stable to fixed boundary modes when the aspect ratio is below a threshold value that varies inversely with the shear. Free-boundary stability appears to require non-monotonic current profiles. Current profiles of the TEXTOR type [5] with shoulders near the $q = 1$ surface are much more stable than monotonic profiles, and can remain resistively stable with a free boundary at rather large aspect ratios.

Central pressure gradients are generally strongly destabilizing for the resistive internal kink mode. Part of the reason for this is global (i.e. Δ') effects on the eigenfunction. However, interchange effects at the $q = 1$ resonant surface are important, in particular, when the shear is low, and this makes the stability at finite pressure highly sensitive to shaping. For many shapes of interest, notably, the JET shape, the curvature at $q = 1$ is unfavorable because of ellipticity, and the resistive interchange criterion is generally violated for low shear. For JET-shaped cross sections, we do not find any profile that is resistively stable with $q_0 < 1$ and $\beta_p \geq 0.05$.

A clear conclusion of our stability study of the resistive internal kink mode is that *complete* MHD stability is difficult to achieve for $q_0 < 1$ and finite pressure.



Appendix A

Bicubic Hermite finite element discretization

This Appendix presents the discretization used in CHEASE for the resolution of the Grad-Shafranov equation (2.3). The Grad-Shafranov equation defined over the plasma cross section Ω with Dirichlet boundary condition $\Psi \equiv 0$ is the Euler equation for the following extremum principle:

$$\text{minimize } I(\varsigma) = \int_{\Omega} \int \frac{1}{2} \frac{1}{R} (\nabla \varsigma)^2 dS + \int_{\Omega} \varsigma j_{\Phi} dS \quad (\text{A.1})$$

where ς is an arbitrary weighting function from the same function space as Ψ , i.e.

$$H_E^1 = \left\{ \varsigma \text{ so that } \int_{\Omega} (\varsigma^2 + |\nabla \varsigma|^2) R dS < \infty, \varsigma \equiv 0 \text{ on } \delta\Omega \right\} \quad (\text{A.2})$$

If $\Psi \in H_E^1$ satisfies the extremum principle (A.1), a variation about that function leads to

$$\int_{\Omega} \int \frac{1}{R} \nabla \Psi \cdot \nabla (\delta \Psi) dS + \int_{\Omega} (\delta \Psi) j_{\Phi} dS = 0 \quad (\text{A.3})$$

for all allowed $\delta \Psi \in H_E^1$. This equation is equivalent to eq.(2.6), with $\varsigma = \delta \Psi$.

In CHEASE, the plasma cross section Ω is subdivided into $N_{\sigma} \times N_{\theta}$ rectangular mesh cells for the discretization, where σ and θ are defined in eq.(2.5). The σ and the θ mesh can be spaced arbitrarily.

Instead of minimizing eq.(A.1) over the whole set H_E^1 , we minimize it only over a subset S_E^1 of H_E^1 , containing the piecewise bicubic Hermite functions on the (σ, θ) mesh.

The Ritz approximation of the solution Ψ of the Grad-Shafranov equation (2.3) is then given by

$$\Psi \in S_E^1 \text{ so that } I(\Psi) \leq I(\zeta), \forall \zeta \in S_E^1 \quad (\text{A.4})$$

On the rectangular (σ, θ) mesh, the Hermite bicubic basis functions are products of the one dimensional basis functions

$$\begin{aligned} N_i(x) &= \frac{(x - x_{i+1})^2(x_{i+1} - 3x_i + 2x)}{(x_{i+1} - x_i)^3} \\ M_i(x) &= \frac{(x - x_{i+1})^2(x - x_i)}{(x_{i+1} - x_i)^2} \\ N_{i+1}(x) &= \frac{(x - x_i)^2(3x_{i+1} - x_i - 2x)}{(x_{i+1} - x_i)^3} \\ M_{i+1}(x) &= \frac{(x - x_i)^2(x - x_{i+1})}{(x_{i+1} - x_i)^2} \end{aligned} \quad (\text{A.5})$$

with $x_1 < \dots < x_i < \dots < x_N$ for $x = \sigma$ or θ and $N = N_\sigma$ or N_θ respectively. Figure

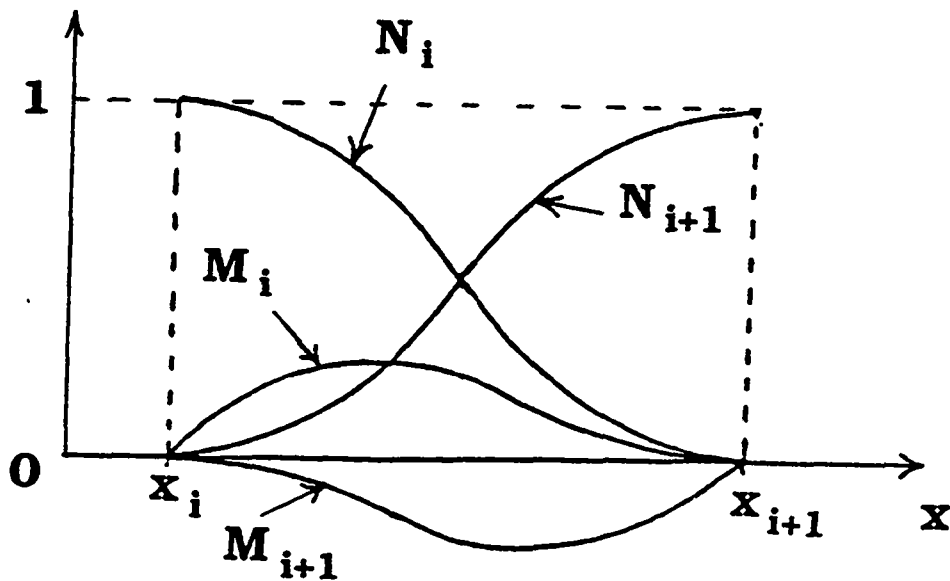


Figure A.1: One-dimensional cubic Hermite basis functions in the interval $[x_i; x_{i+1}]$.

A.1 shows the four cubic Hermite basis functions (A.5) in the interval $x_i \leq x \leq x_{i+1}$.

Thus, the projection of Ψ on S_E^1 reads

$$\begin{aligned} \Psi = \sum_{i=k}^{k+1} \sum_{j=l}^{l+1} & \Psi^{ij} N_i(\sigma) N_j(\theta) + \Psi_{\sigma}^{ij} M_i(\sigma) N_j(\theta) \\ & + \Psi_{\theta}^{ij} N_i(\sigma) M_j(\theta) + \Psi_{\sigma\theta}^{ij} M_i(\sigma) M_j(\theta) \end{aligned} \quad (\text{A.6})$$

in the mesh cell $[\sigma_k; \sigma_{k+1}] \times [\theta_l; \theta_{l+1}]$. Here, the notation $\Psi_x \equiv \partial\Psi/\partial x$ has been used. Substituting eq.(A.6) into the variational form (2.6) and integrating with a Gaussian quadrature method leads to a positive definite symmetric system of linear equations of the form

$$\mathbf{A} \cdot \mathbf{x} = \mathbf{b} \quad (\text{A.7})$$

which is resolved by decomposing \mathbf{A} into

$$\mathbf{A} = \mathbf{L} \mathbf{D} \mathbf{L}^t \quad (\text{A.8})$$

where \mathbf{D} is diagonal and \mathbf{L} is lower triangular. The number of integration points for the Gaussian quadrature is a free input parameter in CHEASE. Usually, we use 4 integration points in both the σ and the θ directions. The matrix \mathbf{A} depends only on geometric quantities, and therefore, the decomposition (A.8) of \mathbf{A} is performed only once for a given $(\sigma; \theta)$ mesh, and every Picard iteration in eq.(2.7) requires only a backsubstitution in eq.(A.7).



Appendix B

Derivation of expressions involved in the flux coordinate transformation

The purpose of this Appendix is to show the relations between the equilibrium coordinates and the generalized poloidal angle χ . These relations are used in CHEASE for the integration of χ and the non-orthogonality $\beta_{\Psi\chi}$.

B.1 Expression of χ in terms of θ on a constant poloidal flux surface

The line element dl on a constant poloidal flux surface is related to the variation $d\chi$ of χ by

$$d\chi = \nabla\chi \cdot d\mathbf{l} = \nabla\chi \cdot \frac{\nabla\Psi \times \nabla\Phi}{|\nabla\Psi||\nabla\Phi|} dl = \frac{R}{J|\nabla\Psi|} dl \quad (\text{B.1})$$

where $J = [(\nabla\Psi \times \nabla\chi) \cdot \nabla\Phi]^{-1}$. Furthermore, dl is defined by

$$\begin{aligned} dl^2 &\equiv g_{\sigma\sigma} d\sigma^2 + g_{\theta\theta} d\theta^2 + 2g_{\sigma\theta} d\sigma d\theta \\ &= \left[\left(\frac{\partial R}{\partial \sigma} \right)^2 + \left(\frac{\partial Z}{\partial \sigma} \right)^2 \right] d\sigma^2 + \left[\left(\frac{\partial R}{\partial \theta} \right)^2 + \left(\frac{\partial Z}{\partial \theta} \right)^2 \right] d\theta^2 + \\ &\quad 2 \left[\frac{\partial R}{\partial \sigma} \frac{\partial R}{\partial \theta} + \frac{\partial Z}{\partial \sigma} \frac{\partial Z}{\partial \theta} \right] d\sigma d\theta \end{aligned} \quad (\text{B.2})$$

where R and Z are given by eq.(2.5). Therefore,

$$dl^2 = \rho_s^2(\theta) d\sigma^2 + \sigma^2 \left[\rho_s^2(\theta) + \left(\frac{d\rho_s}{d\theta} \right)^2 \right] d\theta^2 + 2\sigma \rho_s(\theta) \frac{d\rho_s}{d\theta} d\sigma d\theta. \quad (\text{B.3})$$

Along a constant poloidal flux surface,

$$d\Psi = 0 = \frac{\partial\Psi}{\partial\sigma}d\sigma + \frac{\partial\Psi}{\partial\theta}d\theta. \quad (\text{B.4})$$

Multiplying eq.(B.3) by $(\partial\Psi/\partial\sigma)^2$ and expressing $d\sigma$ in terms of $d\theta$ using eq.(B.4) gives

$$dl = \frac{\sigma\rho_s^2(\theta)|\nabla\Psi|}{\frac{\partial\Psi}{\partial\sigma}}d\theta. \quad (\text{B.5})$$

Substituting eq.(B.5) into eq.(B.1) gives

$$d\chi = \frac{R\sigma\rho_s^2(\theta)}{J\frac{\partial\Psi}{\partial\sigma}}d\theta. \quad (\text{B.6})$$

and integrating with respect to θ leads to the expression of χ in eq.(3.14).

B.2 Relation between the non-orthogonality and the current density

The toroidal current density is defined by

$$j_\Phi = e_\Phi \cdot \nabla \times B \quad (\text{B.7})$$

Substituting the magnetic field (2.1) into eq.(B.7) gives

$$\begin{aligned} j_\Phi &= e_\Phi \cdot \nabla \times (\nabla\Phi \times \nabla\Psi) \\ &= e_\Phi \cdot \nabla \times \left(\frac{|\nabla\Psi|}{R} \frac{\nabla\chi_\perp}{|\nabla\chi_\perp|} \right) \\ &= e_\Phi \cdot \nabla \left(\frac{|\nabla\Psi|}{R|\nabla\chi_\perp|} \right) \times \nabla\chi_\perp \\ &= \frac{\partial}{\partial\Psi} \left(\frac{|\nabla\Psi|}{R|\nabla\chi_\perp|} \right)_n e_\Phi \cdot \nabla\Psi \times \nabla\chi_\perp \\ &= \frac{R}{J_\perp} \frac{\partial}{\partial\Psi} \left(\frac{|\nabla\Psi|^2 J_\perp}{R^2} \right)_n \end{aligned} \quad (\text{B.8})$$

where the subscript n denotes the normal derivative, (Ψ, χ_\perp, Φ) is an orthogonal flux coordinate system, and $J_\perp = [(\nabla\Psi \times \nabla\chi_\perp) \cdot \nabla\Phi]^{-1}$. Therefore,

$$\frac{R^2}{J_\perp} \left(\frac{\partial}{\partial\Psi} \frac{J_\perp}{R^2} \right)_n = \frac{Rj_\Phi}{|\nabla\Psi|^2} - 2 \left(\frac{\partial \ln |\nabla\Psi|}{\partial\Psi} \right)_n \quad (\text{B.9})$$

Moreover,

$$\beta_{\Psi\chi} = \frac{\nabla\Psi \cdot \nabla\chi}{|\nabla\Psi|^2} = \left(\frac{\partial\chi}{\partial\Psi} \right)_n \quad (\text{B.10})$$

and

$$\left(\frac{\partial\chi}{\partial\chi_\perp} \right)_\Psi = \frac{J_\perp}{J} \quad (\text{B.11})$$

Therefore, using eq.(B.9),

$$\begin{aligned} \left(\frac{\partial\beta_{\Psi\chi}}{\partial\chi} \right)_\Psi &= \frac{J}{J_\perp} \left(\frac{\partial}{\partial\Psi} \frac{J_\perp}{J} \right)_n \\ &= -\frac{1}{J} \left(\frac{\partial J}{\partial\Psi} \right)_n + \frac{Rj_\Phi}{|\nabla\Psi|^2} + 2 \left(\frac{\partial \ln R}{\partial\Psi} \right)_n - 2 \left(\frac{\partial \ln |\nabla\Psi|}{\partial\Psi} \right)_n \end{aligned} \quad (\text{B.12})$$

Substituting J by eq.(3.13) and integrating with respect to θ using eq.(B.6) leads to the expression of $\beta_{\Psi\chi}$ in eq.(3.14).



Appendix C

Equilibrium quantities for the codes linked to CHEASE

This Appendix documents the equilibrium quantities required by the stability codes MARS and ERATO, the Alfvén and ion cyclotron range of frequencies code LION, NOVA-W [64] and PEST 3.4 [65]. These codes use an “integer mesh”, with rather arbitrarily-defined χ_k so that $0 = \chi_1 < \dots < \chi_{N_x+1} = 2\pi$, and a “half integer mesh” $\chi_{k+1/2} = (\chi_k + \chi_{k+1})/2$ for $k = 1, \dots, N_x$. Similar integer and half meshes are used in the s -direction.

C.1 ERATO and LION

For ERATO and LION, all quantities of the equilibrium involved in the stability calculation must be computed at the centers of the stability mesh cells, because the discretization is done with the so-called “hybrid finite elements”. In Table C.1, all quantities with $j > 6$ are computed on the $(s_{l+1/2}; \chi_{k+1/2})$ mesh, except at the plasma edge. The primes in Table C.1 denote the derivative with respect to Ψ .

C.2 MARS

MARS uses linear finite elements with a tunable integration scheme in the radial direction [48] and Fourier decomposition in the toroidal direction. All equilibrium and vacuum quantities necessary for MARS are directly Fourier transformed in the map-

j	$EQ(j; k; l)$
1	s_l
2	χ_k
3	s_{l+1} for $l \neq N_s + 1$ and s_{l+1} is free for $l = N_s + 1$
4	χ_{k+1}
5	$s_{l+1/2} = (s_l + s_{l+1})/2$ for $l \neq N_s + 1$ and $s_{l+1/2} = 1$ for $l = N_s + 1$
6	$\chi_{k+1/2} = (\chi_k + \chi_{k+1})/2$
7	mass density ρ
8	plasma pressure $\frac{\gamma p}{q_0 \Psi_{min} }$
9	toroidal magnetic flux G
10	free
11	q/q_0
12	poloidal magnetic field $\frac{\Psi R^2}{q_0 \nabla \Psi ^2}$
13	non-orthogonality $\beta_{s,\chi} = 2s \Psi_{min} \beta_{\Psi\chi}$
14	R^2
15	$\left[\frac{\partial \ln(R^2)}{\partial s} \right]_x$
16	$\left[\frac{\partial \ln(R^2)}{\partial \chi} \right]_s$
17	$-2s \Psi_{min} \left(\frac{R j_\Phi}{ \nabla \Psi ^2} - \left[\frac{\partial \ln(R^2/J)}{\partial \Psi} \right]_x \right)$
18	$\frac{2\Psi}{q_0} \left(\frac{j_\Phi^2}{ \nabla \Psi ^2} - \frac{j_\Phi}{R} \left[\frac{\partial \ln \nabla \Psi }{\partial \Psi} \right]_n - p' \left[\frac{\partial \ln R}{\partial \Psi} \right]_n \right)$
19	R^2/J
20	$\left[\frac{\partial \ln(R^2/J)}{\partial \chi} \right]_\Psi$
21	$\frac{\partial}{\partial s} \left[\int_0^x \frac{JG}{R^2} d\chi' \right]$
22	non-orthogonality $\beta_{s,\chi}^{s.f.} = 2s \Psi_{min} \beta_{\Psi\chi}^{s.f.}$ with straight field lines
23	$\left[\frac{\partial \nabla \Psi ^2}{\partial \chi} \right]_\Psi$

Table C.1: Equilibrium quantities for ERATO and LION

j	$EQL(j)$
1	$\frac{g_{ss}}{J_s} = J_s \left(\beta_{sx} \frac{ \nabla s }{R} \right)^2 + \frac{1}{J_s \nabla s ^2}$
2	$\frac{g_{xx}}{J_s} = J_s \left(\frac{ \nabla s }{R} \right)^2$
3	$\frac{g_{\phi\phi}}{J_s} = \frac{R^2}{J_s}$
4	$\frac{g_{sx}}{J_s} = -J_s \beta_{sx} \left(\frac{ \nabla s }{R} \right)^2$
5	$J_s g_{ss}$
6	$J_s g_{xx}$
7	$J_s g_{\phi\phi}$
8	$J_s g_{sx}$
9	J_s
10	$J_s j^x = -2s \Psi_{min} G'$
11	$J_s j^\phi = -J_s (p' + GG'/R^2)$
12	$J_s B^x = 2s \Psi_{min} $
13	$J_s B^\phi = J_s G/R^2$
14	p
15	$\frac{dp}{ds} = 2s \Psi_{min} p'$

Table C.2: Equilibrium quantities for MARS

j	$EQLV(j)$
1	$\frac{g_{ss}}{J_v} = \frac{1}{J_v} \left((R_v - R_{vc})^2 + (Z_v - Z_{vc})^2 \right)$
2	$\frac{g_{\chi\chi}}{J_v} = \frac{s^2}{J_v} \left(\left(\frac{\partial R_v}{\partial \chi} \right)^2 + \left(\frac{\partial Z_v}{\partial \chi} \right)^2 \right)$
3	$\frac{g_{\Phi\Phi}}{J_v} = \frac{1}{J_v} (R_{vc} + s(R_v - R_{vc}))^2$
4	$\frac{g_{s\chi}}{J_v} = \frac{s}{J_v} \left((R_v - R_{vc}) \frac{\partial R_v}{\partial \chi} + (Z_v - Z_{vc}) \frac{\partial Z_v}{\partial \chi} \right)$

Table C.3: Vacuum quantities for MARS

ping of CHEASE. For this operation, the integration method described in Section 3.3 is applied to

$$f(m; n = 0) = \frac{1}{2\pi} \oint_{\Psi=\text{const}} f e^{im\chi} d\chi \quad (\text{C.1})$$

where f represents any EQL in Table C.2 or any $EQLV$ in Table C.3. MARS requires these quantities both on the half and the integer s -mesh. All quantities in Table C.2 are expressed as function of the Jacobian

$$J_s = [(\nabla s \times \nabla \chi) \cdot \nabla \Phi]^{-1} = 2s |\Psi_{min}| J \quad (\text{C.2})$$

and

$$\beta_{s\chi} = \frac{\nabla s \cdot \nabla \chi}{|\nabla s|^2} = 2s |\Psi_{min}| \beta_{\Psi\chi} \quad (\text{C.3})$$

where J is given by eq.(3.13) and $\beta_{\Psi\chi}$ by eq.(3.12). The primes in Table C.2 denote the derivative with respect to Ψ . The vacuum mesh $(s; \chi; \Phi)$ for MARS is defined so that

$$\begin{aligned} R &= R_{vc} + s(R_v - R_{vc}) \\ Z &= Z_{vc} + s(Z_v - Z_{vc}) \end{aligned} \quad (\text{C.4})$$

where $(R_v; Z_v)$ are the Cartesian coordinates of the $(s; \chi)$ nodes on the plasma surface and $(R_{vc}; Z_{vc})$ is the center of the vacuum mesh. Therefore, the Jacobian of the

transformation from the $(s; \chi; \Phi)$ space to Cartesian coordinates in the vacuum is given by

$$J_v = sR \left((R_v - R_{vc}) \frac{\partial Z_v}{\partial \chi} - (Z_v - Z_{vc}) \frac{\partial R_v}{\partial \chi} \right) \quad (\text{C.5})$$

C.3 NOVA-W and PEST 3.4

1	p	$s_{l+1/2}$
2	$\frac{dp}{d\Psi}$	s_l
3	q	s_l
4	$\frac{dq}{d\Psi}$	s_l
5	G	s_l
6	$\frac{dG}{d\Psi}$	s_l
7	$\frac{G}{q}$	s_l
8	$\frac{d}{d\Psi} \left[\frac{G}{q} \right]$	s_l
9	Ψ	s_l
10	Ψ_m	$s_{l+1/2}$
11	R	(s_l, χ_k)
12	Z	(s_l, χ_k)
13	J_m	$(s_l, \chi_{k+1/2})$
14	J	(s_l, χ_k)

Table C.4: Equilibrium quantities for NOVA-W and PEST3.4

The equilibrium quantities for NOVA-W and PEST 3.4 are rescaled according to the following rules

$$\begin{aligned}
 p'_{\text{new}} &= p'_{\text{old}}/\lambda^2 \\
 G'_{\text{new}} &= G'_{\text{old}}/\lambda^2 \\
 q'_{\text{new}} &= q'_{\text{old}}/\lambda^2 \\
 (G/q)_{\text{new}} &= \lambda(G/q)_{\text{old}} \\
 \Psi_{\text{new}} &= \Psi_{\text{old}}\lambda^2 \\
 R_{\text{new}} &= \lambda R_{\text{old}} \\
 Z_{\text{new}} &= \lambda Z_{\text{old}} \\
 J_{\text{new}} &= \lambda J_{\text{old}}
 \end{aligned}
 \tag{C.6}$$

where $\lambda = R_{\text{major}}/R_0$ and R_{major} is the major axis of the torus in meters. Table C.4 shows all the equilibrium quantities required by NOVA-W and PEST 3.4. The s and χ integer and half-integer meshes are similar to the discretization meshes used by ERATO.

Appendix D

Bicubic spline interpolation of the cubic Hermite equilibrium solution

The purpose of this Appendix is to show how the solution for Ψ given in Hermite bicubic basis functions can be smoothed by interpolation using bicubic splines. The smoothing algorithm applied in CHEASE uses a bicubic spline interpolation of Ψ from the values on the (σ, θ) nodes, ignoring the derivatives Ψ_σ , Ψ_θ and $\Psi_{\sigma\theta}$ of the bicubic Hermite solution. The new values of Ψ_σ , Ψ_θ and $\Psi_{\sigma\theta}$ are computed on the nodes such that the Hermite bicubics have continuous second derivatives. Here, we discuss how Ψ_σ , Ψ_θ and $\Psi_{\sigma\theta}$ are computed for the smoothed solution.

The cubic spline interpolation for a tabulated function $f_i = f(x_i)$, $i = 1, \dots, N$ in the interval $[x_j, x_{j+1}]$ is given by [66,67]:

$$f(x) = A_1 f_j + A_2 f_{j+1} + A_3 f_j'' + A_4 f_{j+1}'' \quad (\text{D.1})$$

where

$$\begin{aligned} A_1 &= \frac{x_{j+1} - x}{x_{j+1} - x_j} \\ A_2 &= \frac{x - x_j}{x_{j+1} - x_j} \\ A_3 &= \frac{1}{6} A_1 (A_1^2 - 1) (x_{j+1} - x_j)^2 \\ A_4 &= \frac{1}{6} A_2 (A_2^2 - 1) (x_{j+1} - x_j)^2 \end{aligned} \quad (\text{D.2})$$

The second derivatives $f_i'' = f''(x_i)$, $i = 1, \dots, N$ required for the evaluation of (D.1) are

computed by imposing that the first derivative

$$\frac{df}{dx} = \frac{f_{j+1} - f_j}{x_{j+1} - x_j} - \frac{3A_1^2 - 1}{6} f_j'' + \frac{3A_2^2 - 1}{6} f_{j+1}'' \quad (\text{D.3})$$

is continuous at $x = x_i, i = 1, \dots, N$. This condition is satisfied for $i = 2, \dots, N - 1$ if

$$\frac{x_i - x_{i-1}}{6} f_{i-1}'' + \frac{x_{i+1} - x_{i-1}}{3} f_i'' + \frac{x_{i+1} - x_i}{6} f_{i+1}'' = \frac{f_{i+1} - f_i}{x_{i+1} - x_i} - \frac{f_i - f_{i-1}}{x_i - x_{i-1}} \quad (\text{D.4})$$

and the values for f_1' and f_N' are given as boundary conditions.

For a tabulated function defined on a rectangular grid (x, y) , the bicubic spline interpolation is a product of one-dimensional splines taken in the x and in the y directions. Therefore, the bicubic Hermite finite element solution Ψ on a rectangular (σ, θ) mesh, with periodic boundary conditions in θ (i.e. $\Psi(\sigma, \theta + 2\pi) = \Psi(\sigma, \theta)$) will have smooth first and second derivatives if :

1. Equation (D.4) is solved for all $\theta_k, k = 1, \dots, N_\theta$ with :

- $x_i = \sigma_i, i = 1, \dots, N_\sigma$.
- $f_i = \Psi(\sigma_i, \theta_k), i = 1, \dots, N_\sigma$.
- Boundary conditions : $f_1' = \frac{\partial \Psi}{\partial \sigma}(\sigma_1, \theta_k)$ and $f_{N_\sigma}' = \frac{\partial \Psi}{\partial \sigma}(\sigma_{N_\sigma}, \theta_k)$, given by the bicubic Hermite solution.

2. $\frac{\partial \Psi}{\partial \sigma}$ is reevaluated on all (σ, θ) nodes with eq.(D.3).

3. Equation (D.4) is solved for all $\sigma_k, k = 1, \dots, N_\sigma$ with :

- $x_i = \theta_i, i = 1, \dots, N_\theta$.
- $f_i = \Psi(\sigma_k, \theta_i), i = 1, \dots, N_\theta$.
- Periodic boundary conditions, $f_1' = \frac{\partial \Psi}{\partial \theta}(\sigma_k, \theta_1) = \frac{\partial \Psi}{\partial \theta}(\sigma_k, \theta_{N_\theta+1}) = f_{N_\theta+1}'$.

and with :

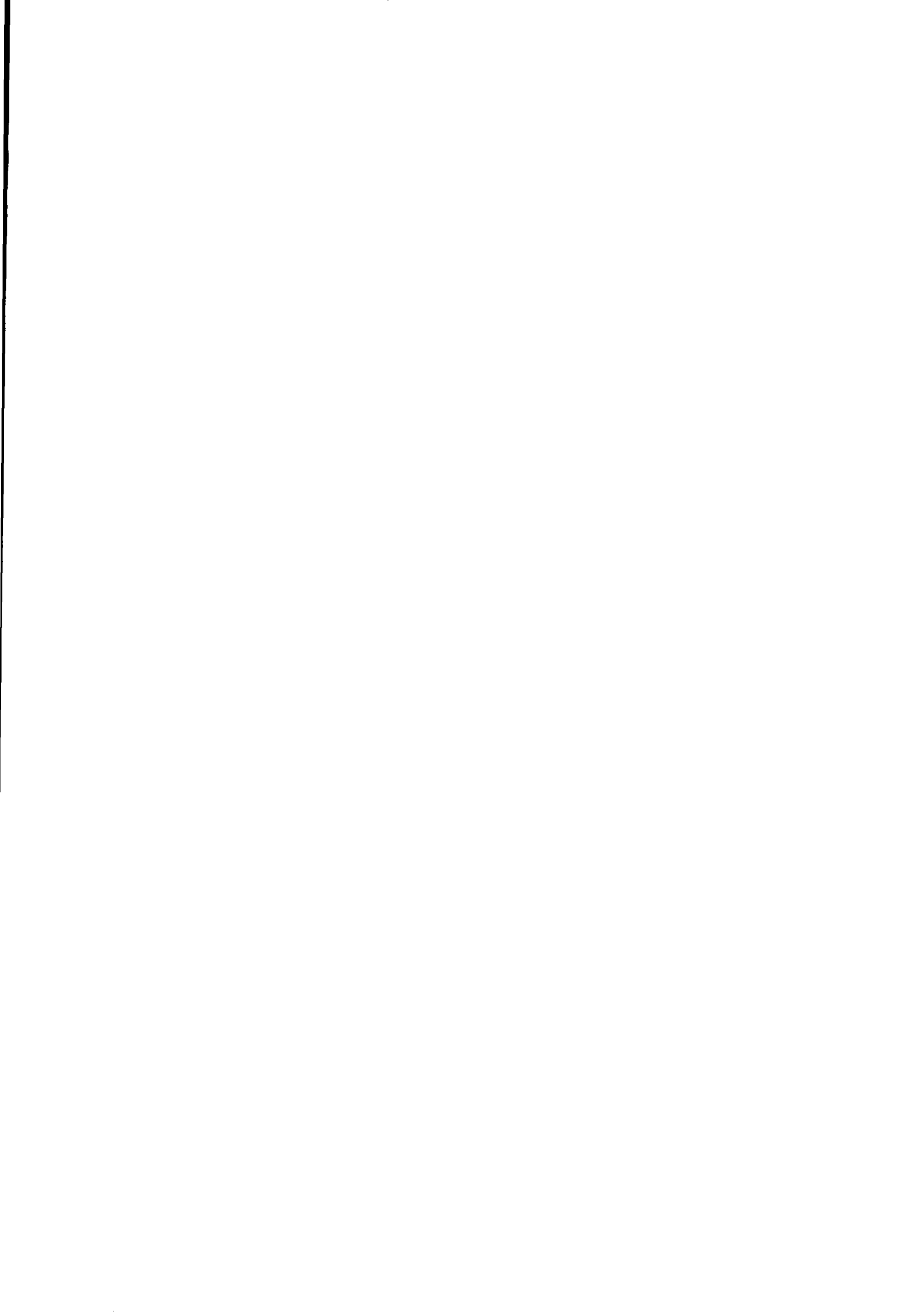
- $x_i = \theta_i, i = 1, \dots, N_\theta$.

- $f_i = \frac{\partial \Psi}{\partial \sigma}(\sigma_k, \theta_i), i = 1, \dots, N_\theta.$

- Periodic boundary conditions, $f'_1 = \frac{\partial^2 \Psi}{\partial \sigma \partial \theta}(\sigma_k, \theta_1) = \frac{\partial^2 \Psi}{\partial \sigma \partial \theta}(\sigma_k, \theta_{N_\theta+1}) = f'_{N_\theta+1}.$

For periodic boundary conditions, the system (D.4) becomes cyclic.

4. $\frac{\partial \Psi}{\partial \theta}$ and $\frac{\partial^2 \Psi}{\partial \sigma \partial \theta}$ are recomputed on all (σ, θ) nodes with eq.(D.3).



Appendix E

Derivation of the ballooning stability and the Mercier criterion

This Appendix presents a derivation of the ballooning and Mercier criteria. The calculation closely follows that of Freidberg [10], Chapter 10. The Appendix serves to give the Mercier criterion in terms of the variables used in CHEASE.

E.1 Ideal ballooning stability criterion

It is convenient to start from a variational form of (3.2-3.8) where pressure and current driven terms appear separately in the plasma potential energy. Originally, this formulation of the energy principle was suggested by Furth et al. [68], and a detailed derivation can be found in Freidberg [10], Chapter 8. It reads

$$\delta\mathcal{W} = \delta\mathcal{W}_p + \delta\mathcal{W}_S + \delta\mathcal{W}_v \geq 0 \quad (\text{E.1})$$

for all allowable plasma displacements ξ . \mathcal{W}_p , \mathcal{W}_S and \mathcal{W}_v are the fluid, the plasma surface and the vacuum contributions respectively, with

$$\begin{aligned} \mathcal{W}_p &= \frac{1}{2} \int_{\text{plasma}} \left\{ |\mathbf{Q}_\perp|^2 + B^2 \left[\nabla \cdot \xi_\perp + 2\xi_\perp \cdot \kappa \right]^2 + \Gamma p (\nabla \cdot \xi)^2 - \right. \\ &\quad \left. 2(\xi_\perp \cdot \nabla p)(\kappa \cdot \xi_\perp^*) - J_\parallel (\xi_\perp^* \times \mathbf{b}) \cdot \mathbf{Q}_\perp \right\} d\tau \\ \mathcal{W}_S &= \frac{1}{2} \int_{\text{surface}} |\mathbf{n} \cdot \xi_\perp|^2 \mathbf{n} \cdot \left[\nabla \left(p + \frac{B^2}{2} \right) \right] dS \\ \mathcal{W}_v &= \frac{1}{2} \int_{\text{vacuum}} B_{v1}^2 d\tau. \end{aligned} \quad (\text{E.2})$$

Here, $Q = \nabla \times (\xi \times B)$ is the perturbed magnetic field, $\mathbf{b} = B/B$ is the unit vector in the direction of B and $\kappa = (\mathbf{b} \cdot \nabla)\mathbf{b}$ is the magnetic field line curvature. The indices \perp and \parallel denote the projection of a quantity in the directions parallel and perpendicular to \mathbf{b} , and $[[x]]$ denotes the jump in x from vacuum to plasma.

Ballooning instabilities are pressure driven modes characterized by a highly localized $k_{\perp} \rightarrow \infty$ (or with a toroidal mode number $n \rightarrow \infty$). The assumption $k_{\perp} \rightarrow \infty$, or $k_{\perp}a \gg 1$, where a is the minor radius of the plasma, implies that the scale length of the ballooning instabilities is much smaller than that of the equilibrium ($\sim a \sim 1$).

The natural technique for problems with disparate length scales is the WKB analysis. An eikonal representation is used for functions of interest, here ξ_{\perp} :

$$\xi_{\perp}(\mathbf{r}) = \eta_{\perp}(\mathbf{r})e^{iS(\mathbf{r})} \quad (\text{E.3})$$

We assume that the eikonal, $S(\mathbf{r})$, represents only the rapid perpendicular mode structure, and the envelope, $\eta_{\perp}(\mathbf{r})$, determines the slow parallel dependence. Therefore, if the quantity η_{\perp} is assumed to vary slowly on the equilibrium length scale, i.e. $|a\nabla\eta_{\perp}|/|\eta_{\perp}| \sim 1$,

$$\begin{aligned} B(\mathbf{r}) \cdot \nabla S(\mathbf{r}) &= 0 \\ \mathbf{k}_{\perp} &= \nabla S(\mathbf{r}). \end{aligned} \quad (\text{E.4})$$

Substituting eq.(E.3) into \mathcal{W}_p in eq.(E.2) leads to

$$\begin{aligned} \mathcal{W}_p &= \frac{1}{2} \int_{\text{plasma}} \left\{ |\nabla \times (\eta_{\perp} \times B)_{\perp}|^2 + B^2 \left[i\mathbf{k}_{\perp} \cdot \eta_{\perp} + \nabla \cdot \eta_{\perp} + 2\kappa \cdot \eta_{\perp} \right]^2 - \right. \\ &\quad \left. 2(\eta_{\perp} \cdot \nabla p)(\eta_{\perp}^* \cdot \kappa) - J_{\parallel}(\eta_{\perp}^* \times \mathbf{b}) \cdot \nabla \times (\eta_{\perp} \times B)_{\perp} \right\} d\tau \end{aligned} \quad (\text{E.5})$$

Examining eq.(E.5) shows that \mathbf{k}_{\perp} appears explicitly only in the second term of the integrand (= magnetic compression term).

Now, we consider the limit $k_{\perp} \rightarrow \infty$. If η_{\perp} is expanded so that

$$\eta_{\perp} = \eta_{\perp 0} + \eta_{\perp 1} + \dots \quad (\text{E.6})$$

with $|\boldsymbol{\eta}_{\perp 1}|/|\boldsymbol{\eta}_{\perp 0}| \sim 1/k_{\perp}a$, \mathcal{W}_p can be systematically minimized at the different orders in $1/k_{\perp}a$. At order zero, \mathcal{W}_p reduces to

$$\mathcal{W}_{F0} = \frac{1}{2} \int B^2(\mathbf{k}_{\perp} \cdot \boldsymbol{\eta}_{\perp 0})^2 d\tau \quad (\text{E.7})$$

\mathcal{W}_{F0} is minimized for any perturbation which satisfies $\mathbf{k}_{\perp} \cdot \boldsymbol{\eta}_{\perp 0} = 0$, i.e.

$$\boldsymbol{\eta}_{\perp 0} = y\mathbf{b} \times \mathbf{k}_{\perp}. \quad (\text{E.8})$$

where y is a scalar quantity, varying on the slow equilibrium scale. The next non-vanishing contribution of \mathcal{W}_p occurs at second order:

$$\begin{aligned} \mathcal{W}_{F2} = \frac{1}{2} \int \left\{ |\nabla \times (\boldsymbol{\eta}_{\perp 0} \times \mathbf{B})_{\perp}|^2 + B^2 \left[i\mathbf{k}_{\perp} \cdot \boldsymbol{\eta}_{\perp 1} + \nabla \cdot \boldsymbol{\eta}_{\perp 0} + 2\boldsymbol{\kappa} \cdot \boldsymbol{\eta}_{\perp 0} \right]^2 - \right. \\ \left. 2(\boldsymbol{\eta}_{\perp 0} \cdot \nabla p)(\boldsymbol{\eta}_{\perp 0}^* \cdot \boldsymbol{\kappa}) - J_{\parallel}(\boldsymbol{\eta}_{\perp 0}^* \times \mathbf{b}) \cdot \nabla \times (\boldsymbol{\eta}_{\perp 0} \times \mathbf{B})_{\perp} \right\} d\tau \end{aligned} \quad (\text{E.9})$$

The quantity $\nabla \times (\boldsymbol{\eta}_{\perp 0} \times \mathbf{B})_{\perp}$ modified with eq.(E.8):

$$\begin{aligned} \nabla \times (\boldsymbol{\eta}_{\perp 0} \times \mathbf{B})_{\perp} &= \nabla \times (yB\mathbf{k}_{\perp})_{\perp} \\ &= (\mathbf{b} \cdot \nabla X)\mathbf{b} \times \mathbf{k}_{\perp} \end{aligned} \quad (\text{E.10})$$

where $X \equiv yB$. Thus, substituting (E.8) and (E.10) into the last term of eq.(E.9) gives

$$\begin{aligned} J_{\parallel}(\boldsymbol{\eta}_{\perp 0}^* \times \mathbf{b}) \cdot \nabla \times (\boldsymbol{\eta}_{\perp 0} \times \mathbf{B})_{\perp} &= \\ J_{\parallel}y^*(\mathbf{b} \cdot \nabla X)[(\mathbf{b} \times \mathbf{k}_{\perp}) \times \mathbf{b}] \cdot (\mathbf{b} \times \mathbf{k}_{\perp}) &= 0 \end{aligned} \quad (\text{E.11})$$

and \mathcal{W}_{F2} reduces to

$$\begin{aligned} \mathcal{W}_{F2} = \frac{1}{2} \int \left\{ k_{\perp}^2 |\mathbf{b} \cdot \nabla X|^2 + B^2 \left[i\mathbf{k}_{\perp} \cdot \boldsymbol{\eta}_{\perp 1} + \nabla \cdot \boldsymbol{\eta}_{\perp 0} + 2\boldsymbol{\kappa} \cdot \boldsymbol{\eta}_{\perp 0} \right]^2 - \right. \\ \left. \frac{2}{B^2} (\mathbf{b} \times \mathbf{k}_{\perp} \cdot \nabla p)(\mathbf{b} \times \mathbf{k}_{\perp} \cdot \boldsymbol{\kappa}) |X|^2 \right\} d\tau. \end{aligned} \quad (\text{E.12})$$

$\boldsymbol{\eta}_{\perp 1}$ appears only in the non-negative second term of eq.(E.12), and therefore, \mathcal{W}_{F2} is minimized by choosing

$$i\mathbf{k}_{\perp} \cdot \boldsymbol{\eta}_{\perp 1} = -\nabla \cdot \boldsymbol{\eta}_{\perp 0} - 2\boldsymbol{\kappa} \cdot \boldsymbol{\eta}_{\perp 0} \quad (\text{E.13})$$

The only contributions to \mathcal{W}_{F2} which remain to be minimized are therefore

$$\mathcal{W}_{F2} = \frac{1}{2} \int d\tau \left\{ k_{\perp}^2 |\mathbf{b} \cdot \nabla X|^2 - \frac{2}{B^2} (\mathbf{b} \times \mathbf{k}_{\perp} \cdot \nabla p) (\mathbf{b} \times \mathbf{k}_{\perp} \cdot \boldsymbol{\kappa}) |X|^2 \right\}. \quad (\text{E.14})$$

The last step in the derivation of the ballooning stability criterion is the determination of the eikonal function S . This requires the introduction of a coordinate system, here the axisymmetric flux coordinates (Ψ, χ, Φ) . In axisymmetric geometry, the displacement $\boldsymbol{\xi}$ can be Fourier decomposed with respect to Φ :

$$\boldsymbol{\xi}(\Psi, \chi, \Phi) = \boldsymbol{\xi}(\Psi, \chi) e^{-in\Phi} \quad (\text{E.15})$$

where n is the toroidal mode number. Therefore, $\boldsymbol{\eta}_{\perp} = \boldsymbol{\eta}_{\perp}(\Psi, \chi)$, $X = X(\Psi, \chi)$ and using eq.(2.1),

$$\mathbf{b} \cdot \nabla X = \frac{1}{JB} \frac{\partial X}{\partial \chi} \quad (\text{E.16})$$

Substituting the eikonal form (E.3) into eq.(E.15) gives

$$S(\Psi, \chi, \Phi) = \tilde{S}(\Psi, \chi) - n\Phi. \quad (\text{E.17})$$

The eikonal S must satisfy $\mathbf{B}(\mathbf{r}) \cdot \nabla S(\mathbf{r}) = 0$, i.e.

$$\frac{G}{R^2} \frac{\partial S}{\partial \Phi} + \frac{1}{J} \frac{\partial S}{\partial \chi} = 0. \quad (\text{E.18})$$

Integrating eq.(E.18) with respect to χ , using eq.(E.17), one obtains

$$S = n \left(-\Phi + \int_{\chi_0}^{\chi} \frac{JG}{R^2} d\chi' \right) \quad (\text{E.19})$$

where χ_0 is an arbitrary integration constant.

S given in eq.(E.19) guarantees $\mathbf{B}(\mathbf{r}) \cdot \nabla S(\mathbf{r}) = 0$, but is not physically acceptable, because it is aperiodic in χ . Connor et al. [69], and Dewar and Glasser [70] gave an elegant solution to this problem by constructing a solution $\hat{\boldsymbol{\xi}}_{\perp}$ of eq.(E.2) which is periodic in χ from a series of non-periodic functions, called quasimodes:

$$\hat{\boldsymbol{\xi}}_{\perp}(\Psi, \chi) = \sum_m e^{-im\chi} \int_{-\infty}^{+\infty} e^{im\chi'} \boldsymbol{\xi}_Q(\Psi, \chi') d\chi' \quad (\text{E.20})$$

Any quasimode $\xi_Q(\Psi, \chi)$, which is a solution of the variational form (E.2) in the domain $-\infty < \chi < +\infty$, will generate a periodic solution of eq.(E.2) if it satisfies the boundary conditions $\xi_Q(\Psi, \chi \rightarrow \pm\infty) = 0$. Therefore, $\xi_Q(\Psi, \chi)$ does not need to be periodic in χ , and can be expressed in the eikonal form (E.3). The ballooning mode energy is then transformed into

$$\mathcal{W}_{F2} = \frac{1}{2} \int_{-\infty, \Psi=\text{const}}^{+\infty} J d\chi \left\{ k_{\perp}^2 \left(\frac{1}{JB} \frac{\partial X}{\partial \chi} \right)^2 - \frac{2}{B^2} (\mathbf{b} \times \mathbf{k}_{\perp} \cdot \nabla p) (\mathbf{b} \times \mathbf{k}_{\perp} \cdot \boldsymbol{\kappa}) |X|^2 \right\} \quad (\text{E.21})$$

where X is now the amplitude of the quasimode $\xi_Q(\Psi, \chi)$.

The coefficient of $|X|^2$ in eq.(E.21) can be expressed in terms of the equilibrium quantities. For this purpose, it is convenient to introduce the following set of locally orthogonal unit vectors:

$$\begin{aligned} \mathbf{n} &= \frac{\nabla \Psi}{|\nabla \Psi|} \\ \mathbf{t} &= \frac{1}{B} \left(\frac{G}{R} \frac{\nabla \Phi \times \nabla \Psi}{|\nabla \Phi \times \nabla \Psi|} - |\nabla \Phi \times \nabla \Psi| \mathbf{e}_{\phi} \right) \\ \mathbf{b} &= \frac{1}{B} \left(\nabla \Phi \times \nabla \Psi + \frac{G}{R} \mathbf{e}_{\phi} \right) \end{aligned} \quad (\text{E.22})$$

Every vector $\mathbf{w} = w_n \mathbf{n} + w_t \mathbf{t}$ defined in the plane perpendicular to \mathbf{b} satisfies

$$\begin{aligned} (\mathbf{b} \times \mathbf{k}_{\perp}) \cdot \mathbf{w} &= (k_n w_t - k_t w_n) \mathbf{b} \cdot (\mathbf{n} \times \mathbf{t}) \\ &= k_n w_t - k_t w_n \end{aligned} \quad (\text{E.23})$$

where $\mathbf{k}_{\perp} = k_n \mathbf{n} + k_t \mathbf{t}$. The magnetic field line curvature

$$\begin{aligned} \boldsymbol{\kappa} &= \mathbf{b} \cdot \nabla \mathbf{b} \\ &= -\mathbf{b} \times \left(\frac{1}{B} \nabla \times \mathbf{B} - \mathbf{B} \times \nabla \left(\frac{1}{B} \right) \right) \\ &= \frac{1}{B^2} \left(\nabla p + \frac{1}{2} \nabla_{\perp} B^2 \right) \end{aligned} \quad (\text{E.24})$$

is perpendicular to \mathbf{b} . Thus,

$$\boldsymbol{\kappa} = \kappa_n \mathbf{n} + \kappa_t \mathbf{t} \quad (\text{E.25})$$

and using eq.(E.4) and eq.(E.24),

$$\begin{aligned}
k_n = n \cdot \nabla S &= |\nabla \Psi| \left[\frac{\partial S}{\partial \Psi} \right]_n \\
&= n |\nabla \Psi| \int_{x_0}^x \frac{\partial}{\partial \Psi} \left[\frac{JG}{R^2} \right]_n d\chi' \\
&\equiv n |\nabla \Psi| g \\
k_t = t \cdot \nabla S &= (t \cdot \nabla S) \frac{\partial S}{\partial \chi} + (t \cdot e_\phi) \frac{1}{R} \frac{\partial S}{\partial \Phi} \\
&= \frac{1}{B} \left(\frac{G}{J |\nabla \Psi|} \frac{\partial S}{\partial \chi} - \frac{|\nabla \Psi|}{R^2} \frac{\partial S}{\partial \Phi} \right) \\
&= \frac{nB}{|\nabla \Psi|} \\
\kappa_n = n \cdot \kappa &= \frac{\nabla \Psi}{|\nabla \Psi|} \cdot \frac{\partial}{\partial \Psi} \left(p + \frac{B^2}{2} \right) \frac{\nabla \Psi}{B^2} \equiv \left[\frac{\partial \tilde{P}}{\partial \Psi} \right]_n \frac{|\nabla \Psi|}{B^2} \\
\kappa_t = t \cdot \kappa &= \frac{G}{2J |\nabla \Psi| B^3} \left[\frac{\partial B^2}{\partial \chi} \right]_\Psi \equiv \frac{G}{J |\nabla \Psi| B^3} \left[\frac{\partial \tilde{P}}{\partial \chi} \right]_\Psi
\end{aligned} \tag{E.26}$$

Substituting eq.(E.23) and eq.(E.26) into eq.(E.21) leads to the ballooning potential energy

$$\delta \mathcal{W}_p(n \rightarrow \infty) = \frac{1}{2} \int_{-\infty}^{+\infty} \left\{ c_1 \left| \frac{\partial \xi}{\partial \chi} \right|^2 + c_2 |\xi|^2 \right\} J d\chi \tag{E.27}$$

where

$$\begin{aligned}
\nu &= \frac{JG}{R^2} \\
B^2 &= \frac{1}{R^2} [G^2 + |\nabla \Psi|^2] \\
c_1 &= \frac{1}{J^2 |\nabla \Psi|^2} \left(1 + \frac{|\nabla \Psi|^4}{B^2} g^2 \right) \\
c_2 &= -\frac{2p'}{B^2} \left[\left(\frac{\partial \tilde{P}}{\partial \Psi} \right)_n - \frac{gG}{B^2} \frac{1}{J} \left(\frac{\partial \tilde{P}}{\partial \chi} \right)_\Psi \right] \\
g &= \nu \beta_{\Psi\chi} + \int_{x_0}^x \left(\frac{\partial \nu}{\partial \Psi} \right)_\chi d\chi' \\
\tilde{P} &= p + \frac{B^2}{2}
\end{aligned} \tag{E.28}$$

E.2 Mercier stability criterion

The derivation of the Mercier stability criterion [13], toroidal equivalent of the Suydam stability criterion for a cylinder [71], follows the work of Connor et al. [69]. The

minimizing Euler-Lagrange equation of the ballooning potential energy (3.17) is

$$\frac{\partial}{\partial \chi} \left(J c_1 \frac{\partial X}{\partial \chi} \right) - J c_2 X = 0 \quad (\text{E.29})$$

where c_1 and c_2 are defined in eq.(E.28). Newcomb's stability analysis [72] shows that a sufficient condition for instability is the oscillatory behavior of the solution of the energy principle. Therefore, if the solution of eq.(E.29) is oscillatory as $\chi \rightarrow \pm\infty$, the mode is unstable. Conversely, the ballooning stability limit can be investigated if the solution of eq.(E.29) is non-oscillatory and vanishes sufficiently fast as $\chi \rightarrow \pm\infty$.

As $\chi \rightarrow \infty$, the quantity g appearing in the coefficients c_1 and c_2 becomes arbitrarily large ($g \sim 2\pi q'(\Psi)(\chi - \chi_0)$). Therefore, the asymptotic expansion for X as $\chi \rightarrow \infty$ can be written as

$$X = g^\alpha \left\{ X_0 + \frac{X_1}{g} + \frac{X_2}{g^2} + \dots \right\} \quad (\text{E.30})$$

where $X_j = X_j(\Psi, \chi)$ are assumed to be periodic functions of χ with the same period as the equilibrium. α is the complex indicial coefficient which determines the oscillatory nature of the solution.

The coefficient c_2 in eq.(3.18) can be rewritten

$$c_2 = -\frac{2p'}{B^2} \left[\left(\frac{\partial \tilde{P}}{\partial \Psi} \right)_n - \frac{gG}{B^2} \frac{1}{J} \left(\frac{\partial \tilde{P}}{\partial \chi} \right)_\Psi \right] = -\frac{2p'}{B^2} \left(\frac{\partial \tilde{P}}{\partial \Psi} \right)_n - \frac{g}{J} \frac{\partial}{\partial \chi} \left(\frac{p'G}{B^2} \right)_\Psi \quad (\text{E.31})$$

Substituting this and the expansion (E.30) into the Euler-Lagrange equation (E.29) and equating the terms of equal power in g gives

- Order $g^{\alpha+2}$:

$$\frac{\partial}{\partial \chi} \left(\frac{|\nabla \Psi|^2}{JB^2} \frac{\partial X_0}{\partial \chi} \right) = 0 \quad (\text{E.32})$$

This equation is only satisfied if X_0 is constant, and without loss of generality, X_0 can be set to 1.

- Order $g^{\alpha+1}$:

$$\frac{\partial}{\partial \chi} \left\{ \frac{|\nabla \Psi|^2}{JB^2} \left(\frac{\partial X_1}{\partial \chi} + \alpha \frac{\partial g}{\partial \chi} \right) \right\} + \frac{\partial}{\partial \chi} \left(\frac{Gp'}{B^2} \right) = 0 \quad (\text{E.33})$$

• Order g^α :

$$\begin{aligned} & \frac{\partial}{\partial \chi} \left\{ \frac{|\nabla \Psi|^2}{JB^2} \left(\frac{\partial X_2}{\partial \chi} + (\alpha - 1) \frac{\partial g}{\partial \chi} X_1 \right) \right\} + \\ & (\alpha + 1) \frac{|\nabla \Psi|^2}{JB^2} \frac{\partial g}{\partial \chi} \left(\frac{\partial X_1}{\partial \chi} + \alpha \frac{\partial g}{\partial \chi} \right) + 2 \frac{Jp'}{|\nabla \Psi|} \kappa_n + \frac{\partial}{\partial \chi} \left(\frac{Gp'}{B^2} \right) X_1 = 0 \end{aligned} \quad (\text{E.34})$$

At order $g^{\alpha+1}$ and g^α , X_0 has been replaced by 1. The solution at order $g^{\alpha+1}$ can be integrated with respect to χ :

$$\frac{|\nabla \Psi|^2}{JB^2} \left(\frac{\partial X_1}{\partial \chi} + \alpha \frac{\partial g}{\partial \chi} \right) + \frac{Gp'}{B^2} = \tilde{C} \quad (\text{E.35})$$

\tilde{C} is an integration constant obtained from the periodicity condition $X_1(\chi = 0) = X_1(\chi = 2\pi)$, i.e.

$$\tilde{C} = \left\langle \frac{p'G}{B^2} \right\rangle + \alpha q' \left\langle \frac{|\nabla \Psi|^2}{JB^2} \right\rangle \quad (\text{E.36})$$

where the average is defined by

$$\langle u \rangle = \frac{\oint_{\Psi=\text{const}} \frac{uB^2}{|\nabla \Psi|^2} J d\chi}{\oint_{\Psi=\text{const}} \frac{B^2}{|\nabla \Psi|^2} J d\chi} \quad (\text{E.37})$$

and

$$q' = \frac{1}{2\pi} \oint_{\Psi=\text{const}} \frac{\partial}{\partial \Psi} \left[\frac{JG}{R^2} \right]_n d\chi \quad (\text{E.38})$$

Integrating the equation at order g^α over one period in χ and requiring that X_2 is periodic function in χ gives

$$\begin{aligned} & \oint_{\Psi=\text{const}} \left[(\alpha + 1) \frac{|\nabla \Psi|^2}{B^2} \frac{\partial g}{\partial \chi} \left(\frac{\partial X_1}{\partial \chi} + \alpha \frac{\partial g}{\partial \chi} \right) + \right. \\ & \left. 2 \frac{Jp'}{|\nabla \Psi|} \kappa_n + \frac{\partial}{\partial \chi} \left(\frac{Gp'}{B^2} \right) X_1 \right] d\chi = 0 \end{aligned} \quad (\text{E.39})$$

The last term of this equation is integrated by parts. Thus, substituting $\partial X_1/\partial \chi$ from eq.(E.35) and averaging eq.(E.39) with eq.(E.37) leads to the indicial equation

$$\alpha^2 + \alpha + D_m = 0 \quad (\text{E.40})$$

where

$$D_m = \frac{p'(G^2 J_1 + J_4)}{2\pi(q')^2} \oint \left[\frac{2\kappa_n}{|\nabla\Psi} + \frac{G}{B^2} \left(\frac{Gp'}{|\nabla\Psi|^2} - \frac{1}{J} \frac{\partial g}{\partial\chi} \right) \right] J d\chi + \frac{Gp'J_2}{(q')^2} (q' - Gp'J_2) \quad (\text{E.41})$$

and

$$\left\{ J_1, J_2, J_3, J_4, J_5 \right\} = \frac{1}{2\pi} \oint_{\Psi=\text{const}} \left\{ \frac{1}{R^2|\nabla\Psi|^2}, \frac{1}{|\nabla\Psi|^2}, \frac{R^2}{|\nabla\Psi|^2}, \frac{1}{R^2}, 1 \right\} J d\chi \quad (\text{E.42})$$

This equation is equivalent to Freidberg's result, Chapter 10 [10]. However, certain terms cancel in this form of D_m . Using eq.(E.26) for κ_n , g and \tilde{P} , the integrand in eq.(E.41) is transformed as follows:

$$\begin{aligned} \frac{2\kappa_n}{|\nabla\Psi} + \frac{G}{B^2} \left(\frac{Gp'}{|\nabla\Psi|^2} - \frac{1}{J} \frac{\partial g}{\partial\chi} \right) = \\ \frac{1}{B^2} \left(2 \left[\frac{\partial\tilde{P}}{\partial\Psi} \right]_n - \frac{G}{J} \left(\frac{JG}{R^2} \left[\frac{\partial\beta_{\Psi\chi}}{\partial\chi} \right]_{\Psi} + \frac{\partial}{\partial\Psi} \left[\frac{JG}{R^2} \right]_n \right) + \frac{G^2 p'}{|\nabla\Psi|^2} \right) = \\ \frac{R^2 p'}{|\nabla\Psi|^2} + \frac{1}{B^2} \left(p' + \frac{GG'}{R^2} + \frac{\partial}{\partial\Psi} \left[\frac{|\nabla\Psi|^2}{R^2} \right]_n - \frac{G^2}{JR^2} \left[\frac{\partial J}{\partial\Psi} \right]_n - \frac{G^2}{R^2} \left[\frac{\partial\beta_{\Psi\chi}}{\partial\chi} \right]_{\Psi} \right) \end{aligned} \quad (\text{E.43})$$

The source term of the Grad-Shafranov equation (2.3) can be recognized in eq.(E.43).

Using the relation between j_{Φ} and $\beta_{\Psi\chi}$ in the Appendix B, eq.(B.12), it reads

$$p' + \frac{GG'}{R^2} = -\frac{j_{\Phi}}{R} = -\frac{\partial}{\partial\Psi} \left[\frac{|\nabla\Psi|^2}{R^2} \right]_n - \frac{|\nabla\Psi|^2}{R^2} \left(\left[\frac{\partial\beta_{\Psi\chi}}{\partial\chi} \right]_{\Psi} + \frac{1}{J} \left[\frac{\partial J}{\partial\Psi} \right]_n \right) \quad (\text{E.44})$$

Substituting that into eq.(E.41) leads to

$$\frac{2\kappa_n}{|\nabla\Psi} + \frac{G}{B^2} \left(\frac{Gp'}{|\nabla\Psi|^2} - \frac{1}{J} \frac{\partial g}{\partial\chi} \right) = \frac{R^2 p'}{|\nabla\Psi|^2} - \left[\frac{\partial\beta_{\Psi\chi}}{\partial\chi} \right]_{\Psi} - \frac{1}{J} \left[\frac{\partial J}{\partial\Psi} \right]_n \quad (\text{E.45})$$

and therefore,

$$D_m = \frac{p'}{(q')^2} (G^2 J_1 + J_4) (p' J_3 - J_5) + \frac{Gp'J_2}{(q')^2} (q' - Gp'J_2) \quad (\text{E.46})$$

where the J_i 's are defined in eq.(E.42). The roots of the indicial equation (E.40) are

$$\alpha = -\frac{1}{2} \pm \frac{1}{2} (1 - 4D_m)^{1/2}. \quad (\text{E.47})$$

The transition from oscillatory to non-oscillatory behavior occurs at $D_m = 1/4$. Therefore, the Mercier criterion for interchange stability is given by $-D_I = 1/4 - D_m > 0$, which is equivalent to eq.(3.20).

Appendix F

Definition of symbols appearing in the text

Symbol	Definition
a	Minor radius of torus
$A(\Psi)$	Aspect ratio
\mathbf{A}	Equilibrium problem matrix
A_e, A_i	Logarithmic derivatives of radial displacement
A_l	Coefficient of the large solution outside the resistive layer
b	$q = 2$ or conducting wall radius in large aspect ratio expansion
\mathbf{b}	Equilibrium problem right hand side
\mathbf{B}	Plasma magnetic field
B_p	Poloidal magnetic field
B_0	Toroidal magnetic field
B_v	Vacuum Magnetic field
B_{\pm}	Coefficient of small solutions left and right of the resistive layer
c	Shift constant for $G^2(\Psi)$ in equilibrium transformation
c_1, c_2	Coefficients in ballooning potential energy
$C(\Psi)$	Normalization constant of (Ψ, χ, Φ) Jacobian J at $\Psi = \text{const.}$
$C_0(\Psi), \dots, C_3(\Psi)$	Surface integrals for the definition of I^* and j_p at $\Psi = \text{const.}$
dl	Line element along constant Ψ surface in poloidal plane
dS	Surface element
$-D_I$	Mercier parameter
$-D_R$	Resistive interchange parameter
e	Ellipticity
E	Elliptic deformation in large aspect ratio expansion
\mathbf{E}	Electric field
F	$\mathbf{k} \cdot \mathbf{B}$ operator
g	\sim Normal derivative of eikonal used for WKB in ballooning stability
$G(\Psi)$	Toroidal flux function at $\Psi = \text{const.}$

Symbol	Definition
(g_{ij})	Covariant flux coordinate tensor
(g^{ij})	Contravariant flux coordinate tensor
h	Cell size
H	H of Glasser, Greene and Johnson [12]
I	Total toroidal current
$I^*(\Psi)$	Surface averaged toroidal current density at $\Psi = \text{const.}$
I_N	Normalized toroidal current
$I_\Phi(\Psi)$	Toroidal current inside $\Psi = \text{const.}$
$j_p(\Psi)$	Volume averaged parallel current density at $\Psi = \text{const.}$
j_Φ	Toroidal current density
J	(Ψ, χ, Φ) flux coordinates Jacobian
\tilde{J}	(r, w, Φ) Jacobian in large aspect ratio expansion
J_s	(s, χ, Φ) flux coordinates Jacobian
J_v	(s, χ, Φ) flux coordinates Jacobian in vacuum
J	Current density
J_1, \dots, J_6	Integrals for Mercier and resistive interchange criteria
l_i	Plasma inductance
L_R	Resistive layer width
m	Poloidal mode number
M_i	Cubic Hermite basis function
n	Toroidal mode number
\hat{n}	Unity vector normal to constant Ψ surfaces
N	Inverse of cell size, so that $N = N_\sigma = N_\theta = 1/h$
N_i	Cubic Hermite basis function
N_m	Number of poloidal Fourier components for MARS
N_s	Number of radial intervals for stability discretization
N_θ	Number of angular intervals for equilibrium discretization
N_σ	Number of radial intervals for equilibrium discretization
N_χ	Number of angular intervals for stability discretization
$p(\Psi)$	Pressure
ppf.	Pressure peaking factor
\tilde{P}	$p + B^2/2$
P_n	$\epsilon^3 \cos n\omega$ correction of R in large aspect ratio expansion
$q(\Psi)$	Safety factor at $\Psi = \text{const.}$
q_0	Safety factor on axis
q_a	Safety factor at plasma surface
Q	Perturbed magnetic field
Q_n	$\epsilon^3 \sin n\omega$ correction of Z in large aspect ratio expansion
r	Radial coordinate in large aspect ratio expansion
$r_{q=1}$	Radial location of $q = 1$ in large aspect ratio expansion
r_0	Radial location of step in Shafranov current profile
\mathbf{r}	Position vector

Symbol	Definition
R	Radial coordinate in torus
R_0	Major radius of torus
R_c	Major radius of equilibrium mesh center
R_m	Major radius of magnetic axis
R_{vc}	Major radius of vacuum mesh center in MARS
s	Radial stability coordinate
$\hat{s}(\Psi)$	Shear at $\Psi = \text{const.}$
\hat{s}_{local}	Local shear
S	Lundquist number
S_p	Plasma boundary
S_v	Vacuum boundary
t	Time
T	Triangular deformation for large aspect ratio expansion
v	Velocity field
v_A	Toroidal Alfvén velocity
$V(\Psi)$	Volume of $\Psi = \text{const.}$ flux tube $/2\pi$
V_{tot}	Total plasma volume $/2\pi$
W_B	Poloidal magnetic field energy
W_p	Potential energy of plasma
W_S	Plasma surface term of potential energy
W_v	Potential energy of vacuum
\mathbf{x}	Equilibrium problem solution
Z	Vertical coordinate in torus
Z_c	Vertical position of equilibrium mesh center
Z_m	Vertical position of magnetic axis
Z_{vc}	Vertical position of vacuum mesh center for MARS
α	Exponent of R in (Ψ, χ, Φ) Jacobian J
β	Total beta
β^*	Fusion beta
β_p	Poloidal beta at $q = 1$
$\beta_p(\Psi)$	Poloidal beta at $\Psi = \text{const.}$
$\beta_{p,\text{tot}}$	Total poloidal beta
$\beta_{p,\text{crit}}$	Marginal poloidal beta at $q = 1$
β_x	Experimental total beta
$\beta_{s,\chi}$	Non-orthogonality in (s, χ, Φ) coordinates
$\beta_{\Psi,\chi}$	Non-orthogonality in (Ψ, χ, Φ) coordinates
γ	Normalized growth rate
Γ	Ratio of specific heats
δ	Triangularity

Symbol	Definition
Δ	Shafranov shift
$\Delta'(\gamma)$	Inner dispersion relation in resistive layers of the plasma
ϵ	Numerical accuracy of equilibrium solution
ε	Inverse aspect ratio
$\underline{\underline{\epsilon}}$	Dielectric tensor
ζ	Parameter which narrows or broadens equilibrium boundary tips
η	Resistivity
θ	Poloidal angle for equilibrium discretization mesh
κ	Magnetic field line curvature
\mathcal{K}	Elongation
λ	Scale factor for equilibrium transformation
Λ	$R_0\Delta'/r$
μ	Exponent of $ \nabla\Psi $ in (Ψ, χ, Φ) Jacobian J
ν	JG/R^2
ξ	Displacement field
ξ	Radial displacement
$\rho(\Psi)$	Generalized radius at $\Psi = \text{const.}$
ρ_p	Generalized radius of lowest shear region
$\rho_{q=1}$	Generalized radius at $q = 1$
$\rho_s(\theta)$	Plasma radius in (σ, θ) equilibrium coordinates
ρ	Mass density
σ	Radial coordinate for equilibrium discretization
ς	Weighting function in variational equilibrium formulation
τ_A	Toroidal Alfvén time
τ_R	Resistive time connected with minor radius of torus
Φ	Toroidal angle
χ	Generalized poloidal angle for stability calculations
χ_0	Integration constant for ballooning potential energy
Ψ	Poloidal flux function
Ψ_c, Ψ_R, Ψ_Z	Equilibrium solution at equilibrium mesh center
Ψ_{min}	Poloidal flux on magnetic axis
ω	Poloidal angular coordinate for large aspect ratio expansion
ω_A	Toroidal Alfvén frequency
Ω	Plasma cross section

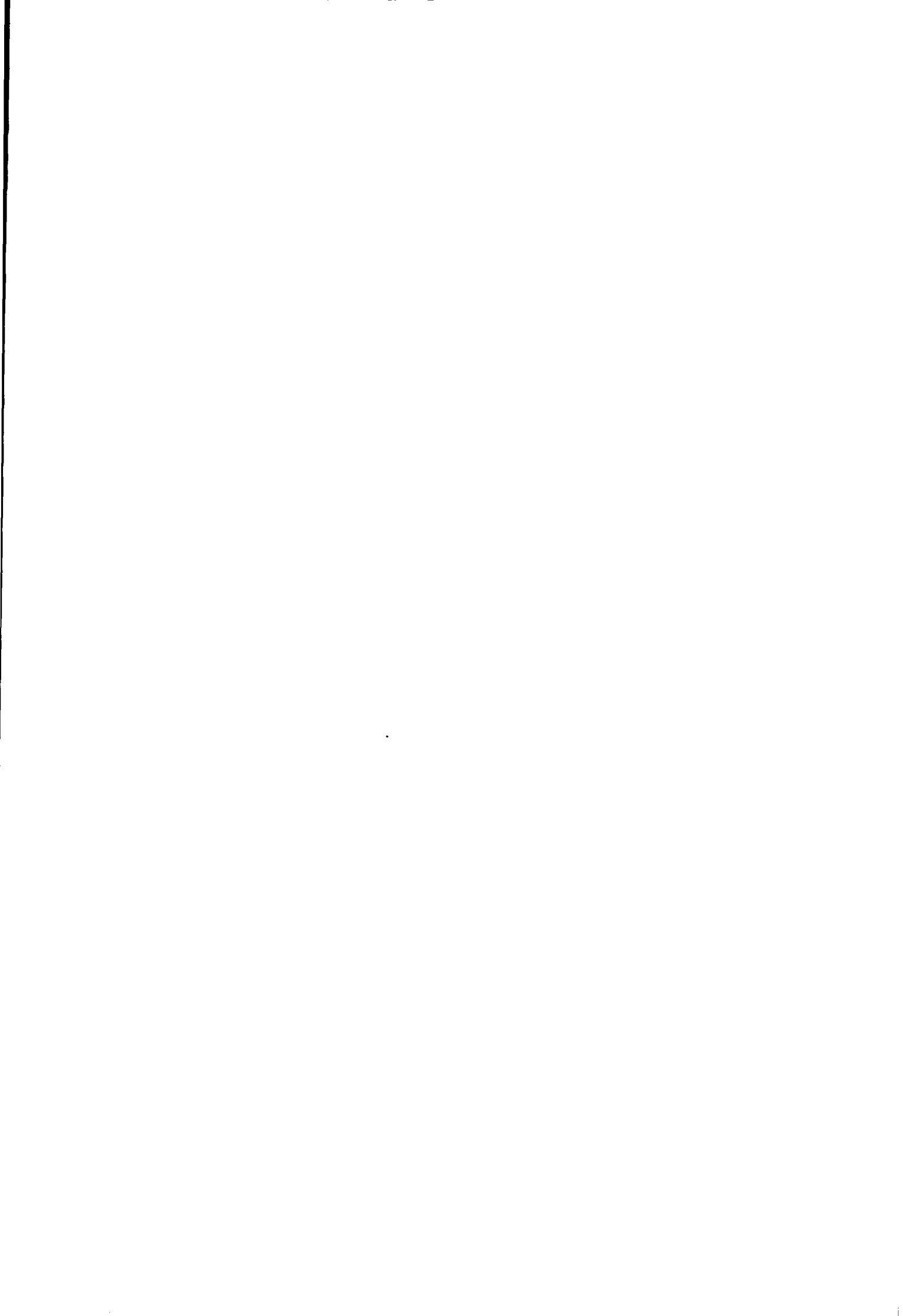
Appendix G

Symbolic names of some important variables computed by CHEASE

Symbol	Definition	Symbolic name	Subroutine
a	(2.24,2.25)	ASPCT	Namelist
$A(\Psi)$		ARATIO	GLOQUA
A	(A.7,A.8)	A	MATRIX, SETUPA
b	(A.7)	B	SETUPB
c	(2.21)	ZCSHFT	NOREPT
c_1, c_2	(3.18)	ZF, ZG	BALOON
$C(\Psi)$	(3.14)	CP	SURFACE
$C'(\Psi)$	(3.14)	CPDP	SURFACE
$C_0(\Psi), \dots, C_3(\Psi)$	(2.15)		CINT
$-D_I(\Psi)$	(3.20)	SMERCI	BALOON
$-D_R(\Psi)$	(3.21)	SMERCR	BALOON
g	(3.18)	ZGBAR	BALOON
$G(\Psi)$	(2.3)	TMF	ISOFUN, PRFUNC
$G'(\Psi)$	(2.3)	TTP	ISOFUN, PRFUNC
H	(3.22)	HMERCR	BALOON
I	(2.4), Table 2.1	RITOT	GLOQUA
$I^*(\Psi)$	(2.13)	CIPR	ISOFUN, PRFUNC
I_N	Table 2.1	RINOR	GLOQUA
$I_\Phi(\Psi)$	Table 2.1	ZJPSI	GLOQUA
$j_p(\Psi)$	(2.14)	CIPR	ISOFUN, PRFUNC
j_Φ	(2.3,2.16,2.17)	PJIPHI	CURRENT
J	(3.13)	ZJAC	SURFACE, ERDATA, JNOVAW, BALOON, VACUUM
J_s	(C.2)	ZJAC	GIJLIN, FOURIER
J_v	(C.5)	ZJAC1	VACUUM

Symbol	Definition	Symbolic name	Subroutine
$J_1(\Psi), \dots, J_6(\Psi)$	(3.19)	ZMC1, ..., ZMC6	BALOOON
l_i	Table 2.1	RINDUC	GLOQUA
M_i	(A.5)	FN2, FN4	BASIS
N_i	(A.5)	FN1, FN3	BASIS
N_m		MSMAX	Namelist
N_s		NPSI	Namelist
N_θ		NT	Namelist
N_σ		NS	Namelist
N_x		NCHI	Namelist
$p(\Psi)$	(2.3)	CPR	PPRIME
$p'(\Psi)$	(2.3)	CPPR	PPRIME
ppf.	Table 2.1	CPPF	GLOQUA
$q(\Psi)$	(2.12)	QPSI	SURFACE
$q'(\Psi)$		CDQ	SURFACE
q_0		Q0	MAPPIN
R_0		1	
R_c	(2.5)	R0	Namelist
R_m		RMAG	MAGAXE
R_{vc}	(C.4)	ROW	Namelist
s_k	(3.10)	CS	MESH
$s_{k+1/2}$	(3.10)	CSM	MESH
$\hat{s}(\Psi)$	Table 2.1	SHEAR	GLOQUA
\hat{s}_{local}	Table 2.1	RSHEAR	ERDATA
$V(\Psi)$	Table 2.1	VSURF	GLOQUA
$2\pi V_{tot}$	Table 2.1	VOLUME	GLOQUA
W_B	(2.22)	WMAGP	ENERGY
x	(A.7)	CPSI	SOLVIT
Z_c	(2.5)	RZ0	Namelist
Z_m		RZMAG	MAGAXE
Z_{vc}	(C.4)	RZ0W	Namelist
α	(3.13)	NER	Namelist
β	Table 2.1	BETA	GLOQUA
β^*	Table 2.1	BETAS	GLOQUA
$\beta_p(\Psi)$	Table 2.1	BETAB	GLOQUA
$\beta_{p,tot}$	Table 2.1	BETAP	GLOQUA
β_x	Table 2.1	BETAX	GLOQUA
$\beta_{s,x}$	(C.3)	BCHIN, BCHIO	SURFACE

Symbol	Definition	Symbolic name	Subroutine
Γ	(1.2)	GAMMA	Namelist
δ	(2.25)	TRIANG	Namelist
ϵ	(2.8)	EPSCON	Namelist
ζ	(2.25)	CETA	Namelist
θ	(2.5)	CT	MESH
κ	Table 2.1	ZCURV	ERDATA
\mathcal{K}	(2.25)	ELLIPT	Namelist
λ	(2.20)	SCALE	NOREPT
μ	(3.13)	NEGP	Namelist
$\rho(\Psi)$	Table 2.1	RSURF	GLOQUA
$\rho_s(\theta)$	(2.5)		BOUND
σ	(2.5)	CSIG	MESH
χ_k	(3.13)	CHI	MESH
$\chi_{k+1/2}$	(3.13)	CHIM	MESH
Ψ	(2.3)	CPSI	SOLVIT
Ψ_c, Ψ_R, Ψ_Z	(2.10)		SOLVIT
Ψ_{Solovev}	(2.24)		TEST
Boundary conditions A	(2.11)		LIMITA
Boundary conditions b	(2.11)		LIMITB
Equilibrium quantities for ERATO & LION	Table C.1	EQ	ERDATA
Equilibrium quantities for MARS	Tables C.2, C.3		MAPPIN
Equilibrium quantities for NOVA-W & PEST3.4	Table C.4		OUTNVW
Bi-spline smoothing of equilibrium	Section 3.5		SMOOTH



Bibliography

- [1] S. von Goeler, W. Stodiek, N. Sauthoff, *Phys. Rev. Lett.* **33**, 1201 (1974).
- [2] B.B. Kadomtsev, *Sov. J. Plasma Phys.* **1**, 389 (1975).
Fiz. Plazmy **1**, 710 (1975).
- [3] M.A. Dubois, D.A. Marty, A. Pochelon, *Nucl. Fusion* **20**, 1155 (1980).
- [4] D.J. Campbell, R.D. Gill, C.W. Gowers, J.A. Wesson, D.V. Bartlett, C.H. Best, S. Coda, A.E. Costley, A.W. Edwards, S.E. Kissel, R.M. Niestadt, H.W. Piekaar, R. Prentice, R.T. Ross, B.J.D. Tubbing, *Nucl. Fusion* **26**, 1085 (1986).
- [5] H. Soltwisch, W. Stodiek, J. Manickam, J. Schlüter, *Plasma Physics and Controlled Nuclear Fusion Research 1986*, Proceedings of the 11th International Conference, Kyoto (IAEA, Vienna, 1987), Vol. 1, p.263.
- [6] J. O'Rourke, J. Blum, J.G. Cordey, A. Edwards, N. Gottardi, B. Keegan, E. Lazzaro, G. Magyar, Y. Stephan, P. Stubberfield, D. Véron, D. Zaslav, *Controlled Fusion and Plasma Heating 1988*, Proceedings of the 15th European Conference, Dubrovnik, (EPS, Geneva, 1988), Vol. 12B Part I, p.155.
- [7] A. Weller, A.D. Cheatham, A.W. Edwards, R.D. Gill, A. Gondhalekar, R.S. Granetz, J. Snipes, J.A. Wesson, *Phys. Rev. Lett.* **59**, 2303 (1987).
- [8] V.D. Shafranov, *Zh. Tekh. Fiz.* **40**, 241 (1970).
Sov. Phys. - Tech. Phys. **15**, 175 (1970).
- [9] J.A. Wesson, *Nucl. Fusion* **18**, 87 (1978).
- [10] J.P. Freidberg, *Ideal Magnetohydrodynamics*, (Plenum Press, New York, 1987).
- [11] M.N. Bussac, R. Pellat, D. Edery, J.L. Soulé, *Phys. Rev. Lett.* **35**, 1638 (1975).
- [12] A.H. Glasser, J.M. Greene, J.L. Johnson, *Phys. Fluids* **18**, 875 (1975).
- [13] C. Mercier, *Nucl. Fusion Suppl.* **1**, 47 (1960).
- [14] B. Coppi, R. Galvao, R. Pellat, M. Rosenbluth, P. Rutherford, *Sov. J. Plasma Phys.* **2**, 533 (1976).
- [15] M.N. Bussac, R. Pellat, D. Edery, J. Soulé, *Plasma Physics and Controlled Nuclear Fusion Research 1976*, Proceedings of the 6th International Conference, Berchtesgaden (IAEA, Vienna, 1977), Vol. 1, p.607.

- [16] D. Berger, L.C. Bernard, R. Gruber, F. Troyon, *Plasma Physics and Controlled Nuclear Fusion Research 1976*, Proceedings of the 6th International Conference, Berchtesgaden (IAEA, Vienna, 1977), Vol. 2, p.411.
- [17] L.S. Solov'ev, *Zh. Tekh. Fiz.* **53**, 626 (1967);
JETP **26**, 400 (1968).
- [18] J.W. Connor, R.J. Hastie, "The effect of shaped plasma cross sections on the ideal internal kink mode in a tokamak", CLM-M-106 (1985), Culham Laboratory, Abingdon, UK.
- [19] T. Takeda, T. Tsunematsu, *Japan Atomic Energy Research Institute Report JAERI-M 8042* (1979)
- [20] J. Blum, J. Le Foll, B. Thooris, *Comput. Phys. Commun.* **24**, 235 (1981).
- [21] S. Semenzato, R. Gruber, H.P. Zehrfeld, *Comput. Phys. Reports* **1**, 389 (1984).
- [22] R. Gruber, R. Iacono, F. Troyon, *J. Comput. Phys.* **73**, 168 (1987).
- [23] J.D. Callen, R.A. Dory, *Phys. Fluids* **15**, 1523 (1972).
- [24] J.L. Johnson, H.E. Dahled, J.M. Greene, R.C. Grimm, Y.Y. Hsieh, S.C. Jardin, J. Manickam, M. Okabayashi, R.G. Storer, A.M. Todd, D.E. Voss, K.E. Weimer, *J. Comput. Phys.* **32**, 212 (1979).
- [25] J. DeLucia, S.C. Jardin, A.M.M. Todd, *J. Comput. Phys.* **37**, 183 (1979).
- [26] A.D. Turnbull, M.A. Secrétan, F. Troyon, S. Semenzato, R. Gruber, *Comput. Phys. Commun.* **66**, 391 (1986).
- [27] K.M. Ling, S.C. Jardin, *J. Comput. Phys.* **38**, 300 (1985).
- [28] L.E. Zakharov, V.D. Shafranov, *Kurchatov Institute Report IAE-3075* (1978).
Oak Ridge National Laboratory Translation ORNL/TR-4667.
- [29] P.N. Vabishchevich, L.M. Degtyar'ev, A.P. Favorskii, *Sov. J. Plasma Phys.* **4**, 554 (1978).
- [30] L.L. Lao, S.P. Hirshman, R.M. Wieland *Phys. Fluids* **24**, 1431 (1981).
- [31] L.L. Lao, *Comput. Phys. Commun.* **31**, 201 (1984).
- [32] H.R. Hicks, R.A. Dory, J.A. Holmes, *Comput. Phys. Reports* **1**, 373 (1984).
- [33] T. Takeda, S. Tokuda, *Comput. Phys. Commun.* **93**, 1 (1991).
- [34] H. Lütjens, A. Bondeson, A. Roy, *Comput. Phys. Commun.* **69**, 287 (1992).
- [35] G. Strang, G. Fix, *An Analysis of the finite element method* (Prentice-Hall, Inc., Englewood Cliffs, N.J., 1973).
- [36] A. Bondeson, G. Vlad, H. Lütjens, *Advances in Simulation and Modelling of Thermonuclear Plasmas 1992*, Proceedings of the IAEA Technical Committee Meeting, Montréal, Canada.
- [37] R. Gruber, F. Troyon, D. Berger, L.C. Bernard, S. Rousset, R. Schreiber, W. Kerner, W. Schneider, K.V. Roberts, *Comput. Phys. Commun.* **21**, 323 (1981).

- [38] L. Villard, K. Appert, R. Gruber, J. Vaclavik, *Comput. Phys. Reports* **4**, 95 (1986).
- [39] A. Bondeson, M.N. Bussac, *Nucl. Fusion* **32**, 513 (1992).
- [40] A.C. Coppi, B. Coppi, *Nucl. Fusion* **32**, 205 (1992).
- [41] J.A. Holmes, B.A. Carreras, L.A. Charlton, *Phys. Fluids* **B1**, 788 (1989).
- [42] J.M. Greene, J.L. Johnson, *Physics Fluids* **5**, 510 (1962).
- [43] V.D. Shafranov, *ZhETF* **33**, (1957);
Sov. Phys. JETP **8**, 494 (1958).
- [44] R. Lüst, A. Schlüter, *Z. Naturforsch.* **129**, 850 (1957).
- [45] H. Grad, H. Rubin, *Proceedings of Second International Conference on the Peaceful Uses of Atomic Energy*, (United Nations, Geneva, 1958), Vol.31, 190.
- [46] K.W. Morton, *Computer Physics Report*, **6**, 1 (1987).
- [47] F. Troyon, R. Gruber, H. Sauremann, S. Semenzato, S. Succi, *Plasma Physics and Controlled Fusion* **26**, 209 (1984).
- [48] G.Y. Fu, A. Bondeson, *Comput. Phys. Commun.* **66**, 167 (1991).
- [49] J.W. Connor, R.J. Hastie, J.B. Taylor, *Phys. Rev. Lett.* **40**, 396 (1978).
- [50] D. Dobrott, D.B. Nelson, J.M. Greene, A.H. Glasser, M.S. Chance, E.A. Frieman, *Phys. Rev. Lett.* **39**, 943 (1977).
- [51] W. Graeb, *Die Grundlehren der mathematischen Wissenschaften, Band XCVII, Lineare Algebra* (Springer Verlag, Berlin Goettingen Heidelberg, 1958), p.157.
- [52] G. Laval, *Phys. Rev. Lett.* **34**, 1316 (1974).
- [53] P.H. Rebut, JET team, *Plasma Physics and Controlled Nuclear Fusion Research 1986*, Proceedings of the 11th International Conference, Kyoto (IAEA, Vienna, 1987), Vol. 1, p.31.
- [54] H. Lütjens, A. Bondeson, G. Vlad, *Nucl. Fusion* **32**, 1625 (1992).
- [55] A. Bondeson, G. Vlad, H. Lütjens, *Phys. Fluids* **B4**, 1889 (1992).
- [56] A.D. Turnbull, F. Troyon, *Nucl. Fusion* **29**, 1887 (1989).
- [57] D. Edery, G. Laval, R. Pellat, J.L. Soulé, *Phys. Fluids* **19**, 260 (1976).
- [58] B.N. Kuvshinov, *Sov. J. Plasma Phys.* **17**, 79 (1991);
Fiz. Plasmy **17**, 139 (1991).
- [59] G. Laval, H. Luc, E.K. Maschke, C. Mercier, R. Pellat, *Plasma Physics and Controlled Nuclear Fusion Research 1970*, Proceedings of the 4th International Conference, Madison (IAEA, Vienna, 1971), Vol. 2, p.507.
- [60] D. Lortz, J. Nührenberg, *Nucl. Fusion* **13**, 821 (1973).
- [61] V.D. Shafranov, E.I. Yurchenko, *Sov. Phys. JETP* **26**, 682 (1968).

- [62] W. Park, D.A. Monticello, *Nucl. Fusion* **30**, 2413 (1990).
- [63] R.J. Hastie, T.C. Hender, B.A. Carreras, L.A. Charlton, J.A. Holmes, *Phys. Fluids* **30**, 1756 (1987).
- [64] D.J. Ward, S.C. Jardin, *Nucl. Fusion* **32**, 973 (1992).
- [65] R.C. Grimm, R.L. Dewar, J. Manickam, *J. Comput. Phys.* **49**, 94 (1983).
- [66] G.E. Forsythe, M.A. Malcolm, C.B. Moler, *Computer Methods for Mathematical Computations* (Englewood Cliffs, N.J., Prentice-Hall), 70 (1977).
- [67] W.H. Press, B.P. Flannery, S.A. Teukolsky, W.T. Vetterling, *Numerical Recipes* (Cambridge University Press, Cambridge), 86 (1989).
- [68] H.P. Furth, J. Killeen, M.N. Rosenbluth, B. Coppi, *Plasma Physics and Controlled Nuclear Fusion Research 1964*, (IAEA, Vienna, 1965), Vol. 1, p.103.
- [69] J.W. Connor, R.J. Hastie, J.B. Taylor, *Proc. R. Soc. London, Ser. A* **365**, 1 (1979).
- [70] R.L. Dewar, A.H. Glasser, *Phys. Fluids* **20**, 1341 (1983).
- [71] B.R. Suydam, *Proceedings of Second International Conference on the Peaceful Uses of Atomic Energy*, (United Nations, Geneva, 1958), Vol.31, 157.
- [72] W.A. Newcomb, *Ann. Phys.* **10**, 232 (1960).

Curriculum vitae

Je suis né à München (Allemagne) le 28 août 1962. J'ai suivi mes études secondaires au collège et lycée international de Ferney-Voltaire (France), où j'ai obtenu mon baccalauréat C (scientifique) en 1981. De 1981 à 1982, j'ai suivi le CMS à l'Ecole Polytechnique Fédérale de Lausanne. En 1982 je me suis inscrit au département de physique de l'EPFL, où j'ai obtenu mon diplôme en 1987. Depuis, je travaille comme assistant au Centre de Recherches en Physique des Plasmas à l'EPFL.

